

# MASSIV: Mass Assembly Survey with SINFONI in VVDS <sup>★</sup> <sup>★★</sup>

## II. Kinematics and close environment classification

B. Epinat<sup>1,2,3\*\*\*</sup>, L. Tasca<sup>3</sup>, P. Amram<sup>3</sup>, T. Contini<sup>1,2</sup>, O. Le Fèvre<sup>3</sup>, J. Queyrel<sup>1,2</sup>, D. Vergani<sup>4</sup>, B. Garilli<sup>5</sup>, M. Kissler-Patig<sup>6</sup>, J. Moutaka<sup>1,2</sup>, L. Pairore<sup>5</sup>, L. Tresse<sup>3</sup>, F. Bournaud<sup>7</sup>, C. López-Sanjuan<sup>3</sup>, and V. Perret<sup>3</sup>

<sup>1</sup> Institut de Recherche en Astrophysique et Planétologie (IRAP), CNRS, 14, avenue Édouard Belin, F-31400 Toulouse, France

<sup>2</sup> IRAP, Université de Toulouse, UPS-OMP, Toulouse, France

<sup>3</sup> Laboratoire d'Astrophysique de Marseille, Université d'Aix-Marseille & CNRS, UMR7326, 38 rue F. Joliot-Curie, F-13388 Marseille Cedex 13, France

<sup>4</sup> INAF-Osservatorio Astronomico di Bologna, via Ranzani 1, I-40127, Bologna, Italy

<sup>5</sup> IASF-INAf, Via Bassini 15, I-20133, Milano, Italy

<sup>6</sup> ESO, Karl-Schwarzschild-Str.2, D-85748 Garching b. München, Germany

<sup>7</sup> Laboratoire AIM Paris-Saclay, CEA/IRFU/SAP, Université Paris Diderot, CNRS, F-91191 Gif-sur-Yvette Cedex, France.

Preprint online version: June 16, 2022

### ABSTRACT

**Context.** Processes driving mass assembly are expected to evolve on different timescales along cosmic time. A transition might happen around  $z \sim 1$  as the cosmic star formation rate starts its decrease.

**Aims.** Identifying the dynamical nature of galaxies on a representative sample is necessary to infer and compare the mass assembly mechanisms across cosmic time.

**Methods.** We present an analysis of the kinematics properties of 50 galaxies with redshifts  $0.9 < z < 1.6$  from the MASSIV sample observed with SINFONI/VLT with a mass range from  $4.5 \times 10^9 M_\odot$  to  $1.7 \times 10^{11} M_\odot$  and a star formation rate from  $6 M_\odot \text{ yr}^{-1}$  to  $300 M_\odot \text{ yr}^{-1}$ . This is the largest sample with 2D-kinematics in this redshift range. We provide a classification based on kinematics as well as on close galaxy environment.

**Results.** We find a significant fraction of galaxies in our sample (29%) experiencing merging or with close companions that may be gravitationally linked. This is thus placing a lower limit on the fraction of interacting galaxies since on-going mergers are probably also present but harder to identify. We find that at least 44% of the galaxies in our sample display ordered rotation whereas at least 35% are non-rotating objects. All rotators except one are compatible with rotation-dominated ( $V_{\text{max}}/\sigma > 1$ ) systems. Non-rotating objects are mainly small objects ( $R_e < 4 \text{ kpc}$ ) and show an anti-correlation between their velocity dispersion and their effective radius. These low mass objects ( $\log M_{\text{star}} < 10.5$ ) may be on-going mergers in a transient state, galaxies with only one unresolved star-forming region, galaxies with an unstable gaseous phase or, less probably, spheroids. Combining our sample with other 3D-spectroscopy samples, we find that the local velocity dispersion of the ionized gas component decreases continuously from  $z \sim 3$  to  $z = 0$ . The proportion of disks also seems to be increasing in star-forming galaxies when the redshift decreases. The number of interacting galaxies seems to be at a maximum at  $z \sim 1.2$ .

**Conclusions.** These results draw a picture in which cold gas accretion may still be efficient at  $z \sim 1.2$  but in which mergers may play a much more significant role at  $z \sim 1.2$  than at higher redshift. From a dynamical point of view, the redshift range  $1 < z < 2$  therefore appears as a transition period in the galaxy mass assembly process. All the data published in this paper are publicly available at the time of the publication following this link: <http://cosmosdb.lambrate.inaf.it/VVDS-SINFONI>.

**Key words.** galaxies: evolution – galaxies: formation – galaxies: kinematics and dynamics – galaxies: high-redshift

<sup>★</sup> Based on observations collected at the European Southern Observatory (ESO) Very Large Telescope, Paranal, Chile, as part of the Programs 179.A-0823, 177.A-0837, 78.A-0177, 75.A-0318, and 70.A-9007.

<sup>★★</sup> Based on observations obtained with MegaPrime/MegaCam, a joint project of CFHT and CEA/DAPNIA, at the Canada-France-Hawaii Telescope (CFHT) which is operated by the National Research Council (NRC) of Canada, the Institut National des Sciences de l'Univers of the Centre National de la Recherche Scientifique (CNRS) of France, and the University of Hawaii. This work is based in part on data products produced at TERAPIX and

the Canadian Astronomy Data Centre as part of the Canada-France-Hawaii Telescope Legacy Survey, a collaborative project of NRC and CNRS.

<sup>\*\*\*</sup> E-mail: benoit.epinat@oamp.fr

## 1. Introduction

During the last decade the first observations of distant galaxies with Integral Field Unit spectrographs (IFU) have lead to the construction of several galaxy samples from  $z \sim 0.5$  to  $z \sim 3$ . These IFU observations have given new insights into the resolved physical properties of galaxy population at various redshifts but a clear view of the transition epoch between young, unstable and clumpy galaxies and evolved and stable galaxies forming the Hubble Sequence is still missing.

In the redshift range  $0.5 < z < 3$ , large quantities of gas are converted into stars, producing a peak in the cosmic star formation at these epochs (see e.g. Hopkins & Beacom 2006; Tresse et al. 2007). Large gas reservoirs are being accreted onto galaxies via various mechanisms: isolated events such as galaxy major and minor mergers (e.g. de Ravel et al. 2009; Conselice et al. 2008; Lin et al. 2008; López-Sanjuan et al. 2011) and cold gas accretion along cosmic filaments, a more continuous process (e.g. Kereš et al. 2005; Dekel & Birnboim 2006; Genel et al. 2008; Dekel et al. 2009). Cosmological numerical simulations have helped to outline the importance that these processes may play in the build-up of the present-day Hubble sequence. Indeed, on the one hand, merging galaxies is a natural mass assembly mechanism expected in the  $\Lambda$ CDM framework where dark matter halos grow from hierarchical assembly. Some authors have shown that a peak of major merger activity might occur around  $1 < z < 2$  (Ryan et al. 2008; Conselice et al. 2008; López-Sanjuan et al. 2009). On the other hand, fresh cold gas accretion along cosmic web filaments may play a significant role at  $z > 2$  but might be less usual at  $z < 1$  (e.g. Dekel et al. 2009; Kereš et al. 2009). This process seems to be efficient for halo masses larger than  $\sim 10^{10} M_{\odot}$  (Bouché et al. 2010).

Recent IFU studies aim at understanding the role of these different processes in the precursors of local ellipticals and spirals. From the IMAGES sample at  $0.4 < z < 0.75$  (Yang et al. 2008; Neichel et al. 2008; Puech et al. 2008; Rodrigues et al. 2008), it has been shown that regular rotating disks where rather similar to local rotators and that merging is playing a significant role in galaxy mass assembly. At higher redshift, the SINS sample at  $z \sim 2.2$  (Genzel et al. 2008; Shapiro et al. 2008; Förster Schreiber et al. 2009; Shapiro et al. 2009; Cresci et al. 2009), the LSD/AMAZE sample at  $z \sim 3.3$  (Gnerucci et al. 2010) and the sample built by Law et al. (2009) at  $2 < z < 3$  are all containing a large fraction of galaxies with high gaseous turbulence. Based on numerical simulations results of unstable gas-rich disks (e.g. Bournaud et al. 2007; Genel et al. 2008; Dekel et al. 2009), these authors claim that continuous cold gas accretion along cosmic web filaments is playing a significant role in mass assembly at these redshifts since they find that half the disks are dispersion-dominated and that even rotation-dominated disks show a high gaseous local velocity dispersion (above  $60 \text{ km s}^{-1}$ ), uncommon for local galaxies (Epinat et al. 2010). Lehnert et al. (2009); Le Tiran et al. (2011) suggested that this high gaseous local velocity dispersion is not directly powered by shocks or Jeans instabilities due to cold gas accretion but might be related to a vigorous star formation at both high and low redshift. This was further supported by Green et al. (2010) that observed a few local analogues to these high redshift galaxies that all have a star formation rate above  $15 M_{\odot}/\text{yr}$ . Gonçalves

et al. (2010) also observed galaxies with high gaseous local velocity dispersion among a sample of  $z \sim 0.2$  Lyman-break analogues that are also forming stars very efficiently. It has been suggested that this intense star-formation could also be triggered by merging (Basu-Zych et al. 2007, 2009a,b; Overzier et al. 2008).

Among these various samples (IMAGES, SINS and LSD/AMAZE), the redshift range  $0.9 < z < 1.8$ , at the peak of the cosmic star formation history, is still poorly explored. The MASSIV survey has been built to study this redshift range which seems to correspond to the period where the modern Hubble Sequence is being built (e.g. Bell et al. 2004; Williams et al. 2009).

The first goal of this paper is to study the dynamical nature of 50 galaxies with  $0.9 < z < 1.6$  from MASSIV and the evolution with redshift of the fraction of galaxies in a given dynamical state. The second objective is to identify the main physical mechanisms responsible for the transition between  $z \sim 2$ , where a large fraction of disks show high intrinsic gaseous velocity dispersions, and  $z \sim 0.5$  where the disks seem to be more “stable”. The general presentation of the MASSIV sample selection and data acquisition strategy is the subject of a companion paper (Contini et al. 2011). An analysis focused on the dynamical properties of rotators is presented in a second companion paper (Vergani et al. submitted) and the analysis of the spatially-resolved metallicity of this first set of 50 MASSIV galaxies is discussed in an third paper (Queyrel et al. 2011).

The paper is organized as follows. In section 2, the MASSIV “first epoch” sample, the observations and the data reduction are presented. In section 3, galaxy morphology and kinematics models are described. The galaxy classification scheme is detailed in section 4 and the discussion of this classification is given in section 5. Appendix A contains detailed informations and comments on each galaxy.

In this paper, we use the cosmological parameters  $\Omega_m = 0.3$ ,  $\Omega_{\Lambda} = 0.7$  and  $H_0 = 70 \text{ km s}^{-1} \text{ Mpc}^{-1}$ .

## 2. Observations and Data reduction

### 2.1. Sample selection

A complete description of the MASSIV sample selection and global properties is presented in Contini et al. (2011). Here we only present a brief summary.

The MASSIV sample contains 84 star-forming galaxies in the redshift range  $0.9 < z < 1.8$ . It has been constructed from the VVDS (VIMOS VLT Deep Survey) spectroscopic survey (Le Fèvre et al. 2005). This survey is I-band magnitude limited and complete up to magnitude  $I_{AB} < 24$  for VVDS-Deep (RA= 02h, Le Fèvre et al. 2005),  $I_{AB} < 24.75$  for VVDS-Ultra-Deep (RA= 02h, Cassata et al. 2010; Le Fèvre et al. in prep) and  $I_{AB} < 22.5$  for VVDS-Wide (RA= 14h and RA= 22h, Garilli et al. 2008). VVDS provides low resolution ( $R \sim 230$ ) spectra that lead to accurate spectroscopic redshifts for 4446 galaxies in the redshift range  $0.9 < z < 2$ .

The selection of the MASSIV sample has been based on star formation activity traced by [O II]  $\lambda 3727$  emission line equivalent width for galaxies with  $z < 1.46$  and from their observed photometric *UBVR*IK spectral energy distribution for galaxies with  $z > 1.46$ . These criteria ensures that the selected targets are star-forming galaxies for which strong emission lines can be studied using SINFONI to trace

the kinematics. The [O II]  $\lambda 3727$  selection criteria has been tested on a pilot sample (Epinat et al. 2009) and has proven to be very efficient. Resulting from this selection function, the MASSIV sample provides a good representation of star-forming galaxies with  $SFR \geq 5 M_{\odot} \text{ yr}^{-1}$  at  $z \sim 1.5$  in the stellar mass regime  $10^9 - 10^{11} M_{\odot}$  (see Contini et al. 2011 for a detailed study).

The MASSIV “first epoch” sample discussed in this paper is a subsample of the MASSIV sample. It contains the 50 galaxies with  $0.9 < z < 1.6$  (the median redshift is 1.24) that have been observed before January 2010. Except two galaxies observed in the VVDS-Ultra-Deep, galaxies studied in this paper are from the VVDS-Deep and VVDS-Wide samples.

## 2.2. Observations

SINFONI (Eisenhauer et al. 2003; Bonnet et al. 2004) has been used to obtain 2D spatially resolved spectroscopy in the NIR of the MASSIV galaxies around the  $H\alpha$  line or around the [O III]  $\lambda\lambda 4959, 5007$  line for four galaxies. Out of an initial sample of 50 galaxies no line was detected for only 4 galaxies. The success rate is much better when the  $H\alpha$  line is targeted (44/46). VVDS220148046 was observed at  $z = 2.244$  whereas it was expected at  $z \sim 1.371$  from the VIMOS spectrum. The redshift determination for this galaxy is based on the observation of [O III]  $\lambda\lambda 4959, 5007$  and  $H\beta$  lines in our SINFONI data. The observations were obtained in service mode from period P79 to period P82 as part of the Large Programme 179.A-0823 (P.I. T. Contini) and during a pilot program presented in Epinat et al. (2009) (ESO runs 75.A-0318 and 78.A-0177). Galaxies were observed in two or three Observing Blocks.

For the galaxies with  $z < 1.1$ ,  $H\alpha$  was observed with the J grism over the spectral range 1.08–1.41  $\mu\text{m}$ , whereas for galaxies with  $z > 1.2$ ,  $H\alpha$  was observed with the H grism over the spectral range 1.43–1.86  $\mu\text{m}$ . [O III]  $\lambda\lambda 4959, 5007$  was observed in the J-band except for VVDS220148046 for which it was observed in the H-band. SINFONI spectral resolution in J and H bands reaches  $\sim 2000$  and  $\sim 2500$  respectively.

For seeing limited observations, in order to maximize the observing efficiency during the nights, we offset alternatively the target from one corner of the field-of-view of the instrument to the opposite one (object nodding). This observing strategy allowed us to avoid sky frame acquisition. For AO observations, we used one sky frame for four object frames in order to maximize the time spent on sources (details in Contini et al. 2011). In addition, we also applied a sub-dithering to avoid the return of the target onto the same position on the chip. To allow for an accurate on-source pointing of our galaxies, we acquired them through a blind offset from a bright nearby star (PSF star used to measure the spatial PSF) to our target. We also observed standard (STD) stars for flux calibration during the same night. Individual exposures were 300s, 600s or 900s with a total on-source integration time that ranges between 1h and 2h.

Most of the data were observed in seeing limited mode using the  $0.125'' \times 0.25''$  pixel scale leading to a  $8'' \times 8''$  field of view with a mean seeing of  $0.68 \pm 0.12''$ , considering only detected galaxies. However, a subset of seven galaxies were observed with the laser guide star (LGS) adaptive optics system using the  $0.05'' \times 0.10''$  pixel scale with

a  $3.2'' \times 3.2''$  field of view. Two of them were not detected (VVDS020126402 and VVDS220071601) and the PSF star was missed for VVDS220386469. The mean spatial resolution for the four other galaxies is  $0.23''$ . The observing details along with the periods when the galaxies were observed are listed in Table 1.

## 2.3. Data reduction

The data reduction has been performed using the ESO-SINFONI pipeline (version 2.0.0, Modigliani et al. 2007) complemented with additional IDL and PYTHON routines in order to perform the data processing homogeneously among the reducers and to improve some reduction steps.

First, the PSF stars and STD stars observations were reduced using standard data reduction.

Then, for each object science frame, the following steps where applied:

1. bad line removal in the raw data;
2. dark current, sky background and night sky line subtraction from the raw data using the contiguous frame (with the target in the opposite corner due to the observing strategy or with only sky in the case of AO data);
3. flat-field correction using an internal lamp;
4. wavelength calibration using arc-lamps;
5. flux calibration using the STD telluric star spectrum with standard techniques to convert counts in flux units. This enables to correct for the atmospheric transmission and instrumental response;
6. cube reconstruction (with and without skylines) in counts;
7. adjustment of the astrometry in order to match our I-band reference images (CFHT12k survey, McCracken et al. 2003) using the acquisition PSF star and the offsets of object observations with respect to this star. This method was not possible on AO data due to missing meta-informations. For some galaxies of the pilot program, no PSF star was observed and in other cases, PSF stars were saturated in the CFHT images which provided a deteriorated astrometry.

In the pipeline, the spaxels are resampled in order to be square ( $0.125''$  or  $0.05''$ ).

All the cubes obtained for each science frame for a given object are then combined using the SINFO\_UTL\_CUBE\_COMBINE recipe to obtain the final cubes using an additional median filtering in order to remove as much as possible the sky line residuals in the final cube.

Mono-dimensional sky spectra are extracted from the sky cubes. They are used to:

- determine the effective spectral resolution: using a Gaussian fit to approximate sky lines, the spectral resolution element is found to be fairly constant over the whole wavelength range, in both J and H bands and the dispersion of the Gaussian was estimated to  $\sigma \sim 2.8 \pm 0.2 \text{ \AA}$ ;
- quantify the noise that was considered as a poissonian noise.

The data from the pilot study (Epinat et al. 2009) have been reduced again using this new procedure.

#### 2.4. Maps extraction

The ionized gas kinematics of MASSIV galaxies is studied through the brightest emission line available in the NIR spectra, the H $\alpha$  line or the [O III]  $\lambda$ 5007 line in a few cases. IDL routines, based on the `mpfit` routine (Markwardt 2009), were used to extract the kinematic maps from the SINFONI data. First, in order to enhance the signal-to-noise ratio (SNR) without degrading the spatial resolution of the data, a sub-resolution two dimensional spatial Gaussian smoothing (FWHM of two pixels) was applied on the data cubes. In addition, the residual cosmic rays were rejected using a  $15\sigma$  clipping on  $3\times 3$  pixels boxes. Then, for each spatial pixel, the spectrum around H $\alpha$  was fit by a single Gaussian profile and a constant continuum (four parameters in total). In order to minimize the effects of noise induced by sky lines but also of sky line residuals on the line parameters determination, the 1D sky spectrum was used as an estimation of the noise to weight the contribution of each spectral element. From these fitting techniques it was possible, for each source, to recover the line flux map, the velocity field and the velocity dispersion map. The instrumental spectral PSF was taken into account to compute the velocity dispersion:  $\sigma^2 = \sigma_{obs}^2 - \sigma_{PSF}^2$ . During the line fitting procedure, the velocity dispersion was allowed to vary in the range  $40 \text{ km s}^{-1}$  (in order to avoid fitting noise) to  $250 \text{ km s}^{-1}$  (in order to avoid fitting a continuum). 2D error maps have also been derived for each quantity from the fitting procedure. These are statistical errors that take into account the error spectrum and that indicate the accuracy of the fit for each parameter. A SNR map was computed. The computation of this map has been refined since the study of the pilot program (Epinat et al. 2009). The presence of sky lines is now taken into account in order to modulate the confidence on the line detection: the inverse of the sky spectrum is used for weighting ( $w$ ). The signal ( $S$ ) is computed as the weighted flux of the line divided by the dispersion of the line ( $\sigma_\lambda$ ) multiplied by  $\sqrt{2\pi}$ . In the following equations, the weight has been normalized ( $\sum w = 1$ ),  $n_z$  is the number of spectral elements,  $\Delta\lambda$  refers to the spectral sampling and is expressed in the same unit as  $\sigma_\lambda$ ,  $m$  is the modeled spectrum,  $c$  is the continuum of the modeled spectrum and  $l$  is the observed line spectrum:

$$S = \frac{n_z \Delta\lambda \sum w(m - c)}{\sigma_\lambda \sqrt{2\pi}}$$

The noise ( $N$ ) is computed as the square root of the weighted variance of the residual spectrum:

$$N = \sqrt{\sum w(l - m)^2}$$

This gives the SNR:

$$\frac{S}{N} = \frac{n_z \Delta\lambda \sum w(m - c)}{\sigma_\lambda \sqrt{2\pi} \sum w(l - m)^2} \quad (1)$$

If the weight is constant then, according to equation 1, the SNR is simply the ratio of the intensity of a Gaussian line over the RMS of the spectrum. This criteria is robust and a SNR threshold of three was used to clean the kinematic maps (see Appendix B). Extra-cleaning was performed manually to remove isolated pixels (less than  $\sim 5$  adjacent pixels) or groups of pixels associated with data artifacts that could have passed the criteria. The existence of any I-band counterpart was checked when there were groups of more than four pixels.

### 3. Modeling

#### 3.1. Morphology modeling

The stellar continuum is barely detected in the SINFONI data. In order to study the morphology of the stellar component, we use the best CFHT I-band images available, i.e. from the CFH12K/CFHT survey (McCracken et al. 2003) for the galaxies in the 14h field and from the CFHT Legacy Survey<sup>1</sup> with the best seeing for the galaxies in the 02h and 22h fields. We ran GALFIT (Peng et al. 2002) on those images using a Sersic profile (Sersic 1968) in order to recover the morphological parameters: the center, the position angle of the major axis ( $PA$ ), the axis ratio ( $b/a$ ), the effective radius ( $R_e$ ), the Sersic index ( $n$ ) and the total magnitude. GALFIT convolves the model to the spatial PSF in order to converge into a set of beam smearing corrected parameters.

In order to obtain robust estimates of the parameters and of their associated error bars, it is mandatory to control the PSF as well as possible. Indeed, for objects with sizes comparable to the resolution, the use of an overestimated PSF leads to low axis-ratios with small error bars since no strong elongation may be reproduced: this would lead to a systematic underestimate of structures in the galaxies. We are indeed in most cases in this situation where the size of the objects is of the same order as the spatial resolution for seeing-limited ground-based imaging surveys. Thus, in each CFHT field, we have randomly selected stars in order to characterize and to follow the variation of the PSF. The detection of stars is based on colour and morphological criteria for the 02h and 22h fields and on morphological criteria only for the 14h field. From these stars, the width, the axis ratio and the orientation of the PSF are found to vary much across the 14h and 22h fields. The most affected field is the 14h one where the seeing smoothly varies from  $0.6''$  to  $1.0''$ . Thus, in each field, we have selected specific PSFs located at  $45''$  from each galaxy on average. The study of the PSF distribution over the various fields enabled us to determine the uncertainty on the PSF FWHM to be  $\sim 0.1$  pixel ( $\sim 20 \text{ mas}$ ). It is estimated as the deviation from large scale variations.

GALFIT produces residual maps that were used to check the convergence of the fits. It was sometimes necessary to fit secondary objects to have a correct fit (cf. Appendix A). The parameters of the fits are summarized in Table 2.

We have tried in a second step to fit the morphology while fixing the position angle of the major axis to the value determined from the kinematics modeling (cf. Section 3.2) as this was done in the pilot study (Epinat et al. 2009). However, this leads to a bias toward high axis ratios because GALFIT cannot match the elongation when the position angle is fixed and finds that round morphologies match better the data. Thus, we adopt in the following the morphologies as derived in an unconstrained way from the CFHT images.

#### 3.2. Kinematics modeling

Among the various dynamical states of galaxies, the easiest to probe is the rotating disk one. We have thus tested the likelihood of this hypothesis for the galaxies in our sample and have recovered the fundamental dynamical parameters

<sup>1</sup> <http://www.cfht.hawaii.edu/Science/CFHLS/>

within this hypothesis. The velocity field is thus fitted with a model that assumes that the ionized gas is located in an infinitely thin rotating disk as done in Epinat et al. (2009). The rotation curve is described by a linear slope in the inner parts and a plateau in the outer parts. The velocity along the line of sight is computed taking into account geometrical position effects. The model parameters are:

- $x_c, y_c$ : the center coordinates;
- $z$ : the redshift corresponding to the systemic velocity;
- $i$ : the inclination of the gaseous disk;
- $PA_k$ : the position angle of the major axis;
- $V_t$ : the plateau rotation velocity;
- $r_t$ : the turnover radius at which the plateau is reached.

The method used to adjust the models is described in details in Epinat et al. (2010). It is based on a  $\chi^2$  minimization and takes the velocity error map into account in order to minimize the contribution of the regions with low SNR. The spatial PSF is taken into account in these models and is described with a two dimension Gaussian. Its FWHM is computed on the PSF stars associated to each observation. To compute the model velocity field, a higher resolution velocity field is constructed (with at least 8 pixels in the PSF FWHM) from the analytical model and a high resolution line flux map has also to be built. Indeed, in a final low spatial resolution element, the contribution of the line of sight velocity at higher resolution is weighted by the true line flux distribution. We use a linear interpolation of the observed flux map in order to avoid making any assumption on the real flux distribution. This is one of the major uncertainty of our models since the real line flux distribution could be more clumpy than observed.

Our model allows to compute the circular velocity within the disk hypothesis. This assumption is not realistic for all the objects in the MASSIV sample in which we also expect mergers (on-going or late stage), spheroids or structures with chaotic motions. However, this hypothesis allows to compute a map containing only the beam smearing effect on velocity dispersion, due to the blurring of large scale motions. Thus, by subtracting quadratically the map deduced from the model to the observed velocity dispersion map, a velocity dispersion map corrected from beam smearing effect is obtained (noted “ $\sigma$  residuals” in Appendix B). This correction is also valid at first order for non-rotating objects, even if it can overestimate the correction in the inner parts. Details of the method are given in Appendix A of Epinat et al. (2010). The maps of the models are shown in Appendix B and the resulting parameters are given in Table 3. For non isolated galaxies (see Section 4), we fit separately the various components when they were extended enough (VVDS220397579). In the Table, companions have the suffix “s”.

The model rotation curve only reproduces the velocity field and is not based on a gravitational potential model (as done for instance in Förster Schreiber et al. 2006; Cresci et al. 2009; Gnerucci et al. 2010) since the shape of the gravitational potential is unknown and can probably not be described by a stellar component only. Note that a gaseous thin disk in rotation is not incompatible with a spheroidal stellar distribution as it has been observed in local ellipticals (e.g. Sarzi et al. 2006) or as suggested from numerical simulations (e.g. Bournaud et al. 2007; Xu et al. 2010).

As described in the following sections, some parameters are difficult to constrain from the kinematics. In order to

reduce the number of free parameters, we constrained the center and the inclination from the morphology to model the kinematics, making the assumption that the stars and the ionized gas follow a common distribution. Thus only four parameters remain free and can be reasonably constrained from our observed velocity fields. Using these constraints, Epinat et al. (2010) have shown from 137 galaxies of the GHASP sample (the largest 2D kinematics sample of nearby late-type galaxies described in Epinat et al. 2008b,a) projected at  $z \sim 1.7$ , that this method enables to recover statistically the other model parameters.

### 3.2.1. Center

Due to the low spatial resolution of our data, the kinematic center of a given galaxy is hardly constrained from the kinematics (Epinat et al. 2010). Thus the centers are taken from the I-band morphology since we expect that in the inner parts of a galaxy at these redshifts, the stars dominate the gravitational potential.

Thanks to the method we have used, the astrometry in the SINFONI data cubes matches the I-band astrometry. However, a post correction is applied in order to match the outer isophotes of the galaxy in the CFHT images and in the H $\alpha$  maps. The median offset of this post correction is 0.18”, which is in agreement with the accuracy of the SINFONI pointing system estimated to be 0.1-0.2” (see SINFONI manual, using a guiding star instead of offsetting from a bright star). This is also the final accuracy of our astrometry. This offset has been computed for 38 galaxies. The other galaxies were excluded (i) when no PSF star was observed or (ii) when they were observed with AO because the observing sequence did not allow to compute an astrometry correction. We find a good agreement between the centers derived from the I-band images and the peak in the H $\alpha$  maps.

### 3.2.2. Inclination

Disk inclination is a critical parameter to estimate because it is directly linked to the rotational velocity ( $V_\theta$ ) of the disks. Indeed, we measure the velocities projected along the line of sight:  $V_{los} = V_\theta \times \sin i$ . Thus, the observed velocity has to be corrected for the inclination and this correction is larger for galaxies with low inclination. Due to this degeneracy between inclination and rotation velocity in rotating disk models, the inclination is not well constrained from the kinematics alone. This degeneracy can theoretically be solved for high resolution observations but not for observations with strong beam smearing (Epinat et al. 2010): this would lead to erroneous rotational velocity. Thus the inclination is constrained from the morphology axis ratio. In addition, since the uncertainty on the inclination (its sine) directly impacts the uncertainty on the rotation velocity, we pay a special attention in deriving realistic error bars on the inclination. The thickness of the disk, which is considered as null in our models, could impact the determination of the inclination, mainly for edge-on galaxies. However, for these objects, the deprojection has a negligible impact on the determination of  $V_{max}$  (less than 3% considering a thickness leading to  $b/a \sim 0.2$ ).

In order to take into account both the uncertainty on the model and the uncertainty on the PSF used to re-

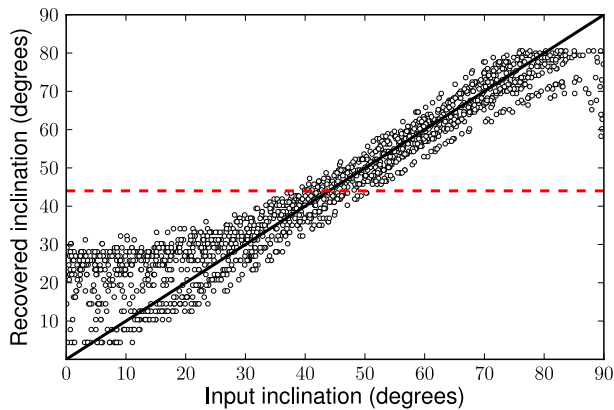


**Fig. 1.** Example of the method used to estimate the uncertainty on the inclination for galaxy VVDS020164388. The x-axis corresponds to the input inclination of the modeled galaxies, the y-axis corresponds to the inclination recovered by GALFIT for each modeled galaxies and the red dashed line corresponds to the inclination of the real galaxy. The uncertainty is measured along this line as the range that contains 68% of the points ( $1\sigma$ ).

cover galaxy parameters in GALFIT, we have used a Monte Carlo method. For each galaxy we simulated 2000 synthetic sources having the same structural parameters (magnitude, Sersic index, effective radius, position angle), but a random value of  $b/a$ . The PSF to simulate these sources was also randomly chosen among different stars in the fields. Poisson noise was added and the simulated sources were placed in a nearby piece of sky from the original image (three pieces for each galaxy). The simulated sources are then modeled with GALFIT using the PSF used for the real galaxy. The final uncertainty is estimated from the range of input inclinations that lead to the inclination that was measured with GALFIT on the real galaxy (see Figure 1). For the smallest galaxies, the inclination is not constrained enough. We thus decided to use an inclination of  $60^\circ$ , the median value for randomly distributed disks, and an uncertainty of  $24^\circ$  that makes a probability of 0.68 ( $1\sigma$ ).

We also checked that there was no bias by studying the inclination distribution for the MASSIV sample. Theoretically, for uniformly randomly oriented thin disks (i.e. with a null thickness) the probability to observe a disk with an inclination between  $\theta_1$  and  $\theta_2$  is equal to  $|\cos\theta_1 - \cos\theta_2|$ , leading to distribution as displayed in black in Figure 2 with a median value of  $60^\circ$ . In Figure 2, we observe that the distribution of MASSIV galaxies having constrained inclinations (filled blue histogram) misses face-on objects ( $i = 0^\circ$ ) and edge-on objects ( $i = 90^\circ$ ) and has an excess of objects with intermediate inclinations compared to the theoretical distribution. The most plausible explanation for the lack of edge-on morphologies is that disks are thick. It could be also that extinction is larger in these galaxies, inducing a non detection of the [O II]  $\lambda 3727$  line in the VVDS spectra. From Figure 1, it is clear that GALFIT cannot recover extreme inclinations. However, the lack of face-on objects could also be attributed to the small numbers expected or to a computing bias. It could also be that galaxies do not have regular morphologies and that, due to surface brightness dimming, one can only observe the clumpy irregular emission. Indeed, I-band morphology

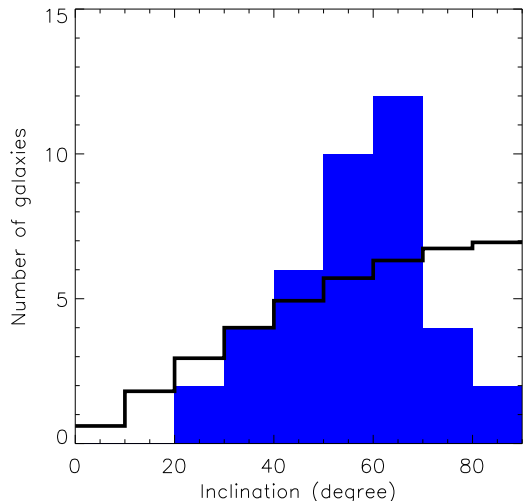


**Fig. 2.** Distribution of the inclinations for the 40 galaxies of the MASSIV sample (having a constrained inclination) using a Sersic profile with GALFIT and assuming they are thin disks (filled blue histogram) compared with the theoretical distribution in the case of a randomly oriented thin disk (black histogram).

could be in some cases contaminated by gaseous emission lines like [O II]  $\lambda 3727$  since the MegaCam/MegaPrime  $i'$  band filter covers the  $0.70$  to  $0.84 \mu\text{m}$  spectral range which corresponds to [O II]  $\lambda 3727$  redshifted between  $0.87$  and  $1.26$ . Unfortunately, CFHT I-band imaging resolution does not allow us to conclude about the clumpy emission. The peak around  $60^\circ$  could also be attributed to (i) the thickness of disks and (ii) the observation of galaxies that are not disks (mergers for example). The median of the distribution for our sample ( $59^\circ$ ) is compatible with the median expected for a distribution of disk with random inclination.

### 3.2.3. Constraints on the other model parameters

Since inner velocity gradients reaching a plateau ( $V_t$ ) within less than one pixel could not be resolved with our spatial resolution that is larger than four pixels, the turnover radius  $r_t$  was thus constrained to be at least one pixel during the fitting process. However, when the model converged toward this value, the statistical error gets null. On the other hand, when the plateau is not reached according to the  $\chi^2$  minimization, the error on  $r_t$  gets large and so do the error on  $V_t$  because the models mainly constrain the slope. Thus the errors on these parameters are difficult to interpret and to propagate to compute the error on the inner slope of the velocity gradient. A solution would consist in using a model described by the slope  $\alpha$  and the turnover radius  $r_t$  in order to estimate the error on the slope. This test has been performed but did not give more realistic errors in many cases. Since this solution was not convincing, we used the original model. For these galaxies, no error is indicated for  $r_t$  and  $V_t$  in Table 3. Although  $r_t$  is not well constrained for small galaxies, it was shown in Epinat et al. (2010), using a 137 galaxies projected at  $z \sim 1.7$ , that leaving  $r_t$  as a free parameter statistically gives a good estimation of the

shape of the rotation curve. It is thus necessary to let  $r_t$  as a free parameter, in particular for the largest galaxies.

### 3.2.4. Parameters deduced from the kinematic maps and models

#### Radius of the H $\alpha$ extent $R_{last}$

This radius is computed from the cleaned maps. The center and position angle from the kinematic best fit models were used in order to derive the radius of each pixel.  $R_{last}$  is the radius that both sides of the galaxy reach.

#### Velocity shear $V_{shear}$

$V_{shear}$  has been computed as the total shear observed in the modeled velocity field shown in Appendix B, i.e. with a SNR threshold of 3 and thus taking into account the uncertainty on the observed velocity field. It is a projected velocity along the line of sight and is not inclination corrected and thus makes no assumption on the geometry of the galaxy. The use of the model enables to smooth the velocity field at the outskirts.

#### Maximum rotation velocity $V_{max}$

This has been computed according to the model at the  $R_{last}$  radius. Two sources of uncertainties have been added in quadrature to compute the final uncertainty on  $V_{max}$ .

The first one is the uncertainty on the inclination (cf. Section 3.2.2). To propagate uncertainties from inclination to rotation velocity, we have used a Monte Carlo method assuming a Gaussian distribution for the inclination. The uncertainty on  $V_{max}$  was thus the standard deviation of the resulting distribution on this parameter.

The second source of uncertainty is related to the modeling. Since the uncertainty on  $V_t$  is a statistical one it can be rather small. Instead of using an approach based on these errors, the GHASP sample (Epinat et al. 2008a,b) has been exploited in order to compute model uncertainties related to the size of the galaxies with respect to the seeing. Using the same method than Epinat et al. (2010), 136 GHASP galaxies were projected at  $z = 1.33$  under typical seeing and sampling of SINFONI observations of the MASSIV sample and the SNR of the simulations has been adjusted to match the H $\alpha$  fluxes from the MASSIV sample. Figure 13 of Epinat et al. (2010) was reproduced with these new simulations. This figure displays the relative error on the maximum velocity determination with respect to the beam smearing parameter defined as  $B = D_{25}/2s$  where  $D_{25}$  is the optical diameter and  $s$  is the seeing FWHM. A linear regression was performed in order to estimate the evolution of the accuracy of the fit with galaxy size. The best fit gives:

$$\delta V_{max} = V_{max} \times \frac{27.5 - 5.8B}{100} \quad (2)$$

The percentage of galaxies below this relation is around 60%. Assuming a Gaussian distribution, 1- $\sigma$  correspond to a confidence level of 68%. We thus simply approximate that  $\delta V_{max}$  is the 1- $\sigma$  uncertainty. For the MASSIV sample,  $B$  was estimated from half-light radii ( $R_e$ ) determined by GALFIT on I-band images (see Section 3.1). Indeed, assuming an exponential disk the following relation can be written:  $D_{25}/2 = 1.9R_e$ . The model uncertainty was thus determined following Equation 2. A minimum uncertainty

of 10 km/s was however imposed. This approach is well adapted for rotators since it has been built from a control sample of rotators.

#### Local velocity dispersion $\sigma$

The velocity dispersion is computed as in Epinat et al. (2009): this is the average of the velocity dispersion map corrected for beam smearing effects (see Section 3.2) and spectral PSF. A weight proportional to the inverse of the uncertainty on the velocity dispersion (estimated before correcting for beam smearing and spectral resolution) is attributed to each pixel to compute the average. The uncertainty on this parameter is computed as the weighted standard deviation.

## 4. Kinematics classification

To disentangle between galaxy formation scenarios, it is necessary to know the dynamical state of galaxies for large samples and at various redshifts.

### 4.1. Previous classification schemes of large samples

The first kinematics classification of distant galaxies observed using integral field unit techniques was provided by Flores et al. (2006) in the frame of the IMAGES sample ( $0.4 < z < 0.75$ ) that contains 68 classified galaxies (Neichel et al. 2008). Their classification is a visual one that relies on both HST optical images and FLAMES/GIRAFFE data. The galaxies were split in three classes: (i) rotating disks that have a good match between morphological and kinematic position angles and a velocity dispersion peak in the center, (ii) perturbed rotators, with a good match between morphological and kinematic position angles but a peak in the velocity dispersion offset from the center and (iii) complex kinematics systems with both a disagreement between morphological and kinematic position angles and a peak in the velocity dispersion offset from the center. They found a majority of galaxies with complex kinematics (44%), and a nearly equivalent fraction of rotating disks (29.5%) and of perturbed rotators (26.5%). From these numbers, they concluded that at that epoch merging is still more active than in the local Universe.

The classification of the SINS sample ( $z \sim 2.2$ ) relies on the asymmetries measured on both the velocity and velocity dispersion fields in order to distinguish rotator-like from merger-like galaxies. These asymmetries were derived either from a kinemetry analysis (Shapiro et al. 2008) or from a qualitative assessment (Förster Schreiber et al. 2009). Then, comparing the mean local velocity dispersion and the rotational velocity, these galaxies (both mergers and rotators) were classified either as rotation-dominated ( $V_{max}/\sigma_0 > 1$ ) or dispersion-dominated ( $V_{max}/\sigma_0 < 1$ ). For small or low SNR galaxies, they rather compared the full velocity shear  $v_{obs}$  with the integrated line width  $\sigma_{int}$  and used a threshold of  $v_{obs}/(2\sigma_{int}) \sim 0.4$ . On the one hand, Förster Schreiber et al. (2009) found that one third of the 62 galaxies in the H $\alpha$  SINS sample contains mergers. On the other hand, they also found that one third of this sample contains rotation-dominated systems, another third corresponds to dispersion-dominated systems and the last third are not classified. They interpret the large amount of dispersion-dominated disks as an evidence for cold gas accretion along cosmic web filaments.



For the LSD/AMAZE sample, since galaxies have a rather low SNR, the classification only distinguishes rotator-like from perturbed galaxies. This classification relies on the modeling of the velocity field as an inclined X-Y plane (Gnerucci et al. 2010). The criterion is based on the  $\chi^2$  of the fit by the plane and on a constraint on the reliability of the inclination of the plane.

In the pilot run study of MASSIV (Epinat et al. 2009), based on a visual kinematic classification, nine galaxies with  $1.2 < z < 1.6$  were classified into three groups: (i) three galaxies are mergers showing disturbed kinematics and possibly several components, (ii) two objects are classified as rotation-dominated disks, with clear signs of rotation and with a maximum rotation velocity larger than the mean local velocity dispersion and (iii) four galaxies are dispersion-dominated disks, with clear signs of rotation but with a maximum rotation velocity lower than the mean local velocity dispersion. It was concluded that about one third of galaxies are observed during some merging event, whereas one third are rotation-dominated and the other third are dispersion-dominated.

In this paper, we present a new kinematic classification for the MASSIV sample in order to put constraints on the dynamical state of galaxies at  $z \sim 1.2$ . The classification scheme has been elaborated in several steps. First, eight people of the collaboration have defined independently their own criteria. These criteria were then reconciled and discussed during a common session and led to a unique classification based both on the close environment and on the velocity shear strength. The visual classification helped in defining measurable criteria in order to build an automatic, thus reproducible, classification (this led to minor changes in the final classes). The final classification was also refined in order to describe the dynamical state and support of the galaxies.

#### 4.2. Galaxy small-scale environment

The study of galaxy close environment is crucial to infer a merger rate in the population probed by the MASSIV sample at  $z \sim 1.2$ . Using SINFONI data and CFHT imaging, galaxies could be classified as interacting or isolated. Flags have also been attributed to this classification in order to qualify its reliability. Flag “A”, “B” and “C” respectively mean secure classification ( $> 90\%$  probability), confident ( $\sim 75\%$  probability) classification and poor reliability ( $\sim 50\%$  probability).

The SINFONI field-of-view was explored in order to detect emission lines that could be attributed to companions. The same field was also explored systematically in the I-band images. Due to the nodding strategy, the field-of-view is larger for seeing-limited observations. In that case, the shape of the field results from the superposition of two  $8''$  square fields overlapped over their opposite corners ( $4''$  quadrants). Thus, the field-of-view of the combined data around each target can be as large as  $6''$  (corresponding to  $\sim 50$  kpc at  $z \sim 1.2$ ). In the non-overlapping regions, the exposure time is half the total on-source exposure time but is sufficient to at least detect emission lines of objects. The explored field is not a full  $12'' \times 12''$  square field but only  $78\%$  of this area. For AO observations, the field of view is restricted to  $3''$  (corresponding to  $\sim 25$  kpc) which is not sufficient to study the environment and thus only

the I-band image was explored in order to see if a possible companion was observed in the  $6''$  around the main object.

Galaxies were classified as interacting with a confidence flag “A” when the following conditions were met: (i) the average SNR (see Table 4) has to be larger than three on an area larger than the seeing, (ii) the systemic velocity difference between the two components has to be lower than  $1000 \text{ km s}^{-1}$  and (iii) an optical counterpart has to be observed within the CFHT I-band image. In the case when the companion is extended but slightly smaller than the seeing, we put a flag “B”. When no counterpart is observed in I-band or on the contrary when some galaxies are observed in the neighborhood in I-band but not in the SINFONI datacube, the object is considered as isolated with a flag “B”. A flag “C” is given for AO observations except if absolutely no other galaxy is observed in I-band around the object. This is detailed in Appendix A.

In some cases, morphology is elongated and several H $\alpha$  blobs can be detected along the elongation, sometimes also in I-band images (see comments in Appendix A). It is not straightforward to assess that these blobs are small objects being accreted rather than star forming regions within one unique galaxy. A monotonic velocity field along the direction of the major axis is likely an evidence for rotation. However, if the elongation is the result of the projection of the two components and if the two objects are small (no gradient detectable in each component), this could mimic a monotonic velocity field due to the difference of radial velocity between the components. Some additional features can also support a merger hypothesis: (i) the angular separation is larger than  $3''$  (ie  $\sim 25$  kpc), because such large galaxies are not expected at high redshift nor observed in the local Universe; (ii) the radial velocity gap is larger than  $\sim 600 \text{ km s}^{-1}$ , since such rotational velocity would imply an unrealistic dynamical mass for a unique object. If one of these features is seen, then galaxies are classified as interacting but with a flag “B”. If none of them is observed, galaxies are classified as isolated but a flag “B” is assigned. For the difficult cases, morphology traced by old stars (mainly observable in near infrared bands) can be used: the old star population might not follow the star forming regions in case of unique objects. The SNR of such J or H-band continuum morphologies recovered from SINFONI data is however rather low. It is thus not straightforward to derived definite conclusions.

When components are very close, i.e. about to merge, the situation is more complex. However, perturbed line profiles (e.g. VVDS020294045, cf. Appendix A) in the region in between the two blobs are in favor of a strong discontinuity in the velocity field and thus to a two components hypothesis. These cases receive a flag “B”.

In the case of on-going mergers, one expects to observe peculiar kinematic signatures. Thus, some galaxies were classified as interacting because their velocity fields, velocity dispersion maps and morphologies were presenting perturbations in the same positions suggesting for instance the presence of tidal arms (e.g. VVDS020283083, cf. Appendix A). Since these signatures are more subjective, these galaxies have usually a flag “B” for the isolation criterion.

Other galaxies were classified as isolated. However, when there were some perturbations in the velocity field or a peak in the velocity dispersion map, this could be interpreted as signs for merger remnants, but since it concerns



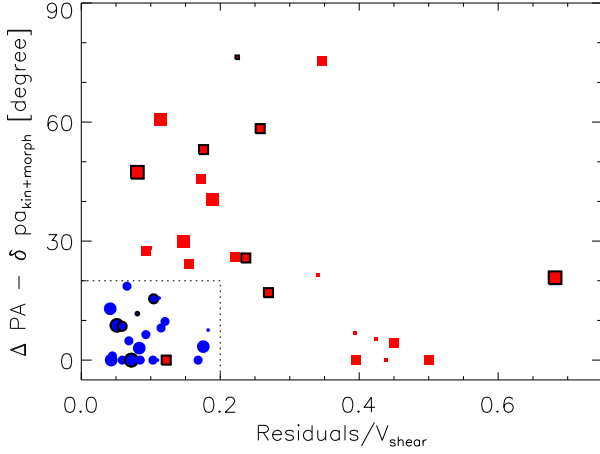


**Fig. 3.** Disagreement between morphological and kinematic position angles (within the errors) as a function of the velocity field residuals normalized by the velocity shear. Blue dots and red squares represent respectively rotating and non-rotating galaxies. Symbols with black contours mark interacting galaxies. Symbol size is related to the SNR of the SINFONI data: small, medium and large symbols refers to galaxies with  $SNR < 5$ ,  $5 < SNR < 10$  and  $SNR > 10$  respectively. One galaxy is not in the expected region (VVDS020294045, cf. Appendix A)

the galaxy outskirts, it is more likely noise and we put a flag “B”.

#### 4.3. Velocity shear strength

To make a kinematic classification, we used a first criterion as simple and objective as possible based on the velocity shear  $V_{shear}$  (see Section 3.2.4). The sample was thus divided into low velocity shear galaxies ( $V_{shear} < 100 \text{ km s}^{-1}$ ) and high velocity shear galaxies ( $V_{shear} > 100 \text{ km s}^{-1}$ ). This gives roughly an idea on the dynamical state of a galaxy without taking into account more complex motions. For VVDS220397579 and VVDS220544394 it was possible to study the velocity shear of the companion as well.

This criterion has the advantage to be easily measured. However, the value of  $V_{shear}$  for a given galaxy may vary with the orientation. It is particularly true for galaxies in ordered rotation ( $V_{shear}$  is lower when observed face-on). However, the distribution of the inclinations, as seen in Figure 2, shows that only eight galaxies according to the theoretical distribution and only three according to the observed distribution may need a correction larger than a factor of two (corresponding to an inclination of  $30^\circ$ ) for the measurement of the velocity shear.

In galaxies having a low velocity shear there might be several classes of objects: (i) very low-mass objects, (ii) face-on rotating galaxies, (iii) on-going mergers in a transient state (iv) spheroids if one expects that the gas in these objects follows the distribution of stars and (v) galaxies with non/slowly-rotating gaseous component.

#### 4.4. Rotating and non-rotating galaxies

For specific analysis (e.g. Tully-Fisher relation, see Vergani et al. submitted), it is essential to be able to define a ro-

bust sample of rotating galaxies. From rotators, we expect to have a rough agreement between their morphological and kinematic position angles. They can be slightly different due to perturbations like bars or strong spiral arms. We also expect for these galaxies that the rotation motions are dominant with respect to perturbations. In order to distinguish rotators from non-rotating galaxies, we have made a diagram in Figure 3 with two quantities that might quantify these two arguments: the disagreement between morphological and kinematic position angles derived from the models presented respectively in sections 3.1 and 3.2 within the uncertainties,  $|PA_m - PA_k| - \sqrt{\delta PA_m^2 + \delta PA_k^2}$ , and the mean weighted velocity field residuals normalized by the velocity shear. Rotators are thus defined as galaxies having a position angle difference lower than  $20^\circ$  and velocity field perturbations lower than 20%. These thresholds have been chosen from the distribution seen in Figure 3 since they enable to isolate a clear cloud of points near the origin (the rotators). We note that these values are also representative of relatively small deviations from rotational motion and position angles. There is one exception in this diagram: VVDS020294045 has been classified visually as non-rotating while it is in the rotators region. Indeed, the velocity shear visible in its velocity field is probably due to a very close companion that thus mimic a rotating disk velocity field. The shape of the line is in favor of a merger. If we could exclude the companion, that is overlapping with the main galaxy, the resulting velocity field would probably be classified as non-rotating (see Appendix A).

We have checked the agreement between this classification and the classification based on kinemetry used in the SINS sample (Shapiro et al. 2008). The agreement is reasonable but we find that galaxies that would be classified as mergers according to their criteria are mainly those that we have classified as non-rotating. Indeed, the classification of Shapiro et al. (2008) relies on the position in a diagram in which galaxies are placed according to their asymmetric velocity and velocity dispersion components. Galaxies show a strong correlation between these two quantities. This correlation is due to the fact that asymmetries are normalized by the global velocity shear. We are able to show that the normalized residuals of the model are well correlated with the normalized asymmetries in the velocity field. This is true for large and small galaxies. Thus, our classification adds the agreement between the position angles in morphology and kinematics as a new criterion. One advantage of this criterion is that it is not restricted to galaxies observed with a good SNR and with large number of resolution elements.

#### 4.5. Dynamical support

The last criterion is related to the dynamical support of galaxies. Indeed, it has been shown that at high redshift ( $z > 2$ ), galaxies are on average more dispersion-dominated than in the intermediate ( $z \sim 0.5$ ) and local Universe. One of our goals is to determine the evolution of the fraction of dispersion-dominated systems with redshift since MASSIV might probe a transitional redshift range.

To quantify the dynamical support, we have made the assumption that galaxies all have some rotation and that this rotation is well described by the rotating disk model. Then, we have made the additional assumption that the local velocity dispersion of the gas is representative of the

random motions in the galaxy. Thus, the dynamical support is estimated by the ratio of the maximum rotation velocity over the local velocity dispersion  $V_{max}/\sigma$ . This description is however intrinsically better justified for rotators.

The various classes and parameters related to them are summarized in Table 4.

## 5. Discussion

Using the classification scheme described above, we were able to classify as rotating or non-rotating the 46 galaxies (including one companion) in the redshift range  $0.9 < z < 1.6$  for which some emission line was detected in SINFONI datacubes. For part of the discussion below we limit the sample to the 36 galaxies with an average SNR (defined in Section 2.4 and reported in Table 4) larger than 5 for which the kinematic classification is more robust (we note that these low SNR galaxies are the majority of galaxies with  $R_{last}/seeing < 1$ , thus for which the kinematic model might be the less robust). This means that among an initial sample of 46 secure galaxies with  $0.9 < z < 1.6$ , 22% are not robustly classified or not classified from their dynamical properties. This proportion is of the same order for the LSD/AMAZE (Gnerucci et al. 2010). In the MASSIV sample, these galaxies have on average lower stellar masses and star formation rates (see Table 5), the latter explaining the lower SNR of these observations. We also emphasize that the large dispersions are due to the two galaxies observed using AO and that have larger stellar masses and SFR than the rest of the unclassified galaxies. For those two galaxies the low SNR is due to the small pixel size rather than an intrinsically low SFR. Concerning the close environment criterion, the 41 systems classified with flags “A” and “B” are considered.

### 5.1. Rotating disks vs. non rotating galaxies

Rotating disks represent at least 44% (20 out of 46 detected galaxies) of the MASSIV “first epoch” sample and about 56% of the high SNR sample. We find a lower fraction of secure non-rotating systems (35% or about 44% of the high SNR sample), having no observed rotation in the gaseous component or having very disturbed kinematics with respect to their broad band morphology. The physical properties of these two classes of galaxies are on average different. We have performed Kolmogorov-Smirnov tests (Press et al. 1992) on stellar mass, SFR, half-light radius and velocity dispersion distributions. The two populations look different in term of stellar mass and SFR at a level slightly higher than  $1\sigma$  (the probability to follow the same distribution is lower than 0.2). Distributions for size and velocity dispersion are fully compatible. Rotating objects are on average more massive ( $M_{star} = 4.0 \times 10^{10} M_{\odot}$ ), more star-forming ( $SFR = 60 M_{\odot} \text{ yr}^{-1}$ ) and with larger radii ( $R_e = 3.8$  kpc) than non-rotating ones ( $M_{star} = 1.6 \times 10^{10} M_{\odot}$ ,  $SFR = 39 M_{\odot} \text{ yr}^{-1}$  and  $R_e = 2.7$  kpc). On the other hand, these two types of galaxies have very similar velocity dispersions around  $60 \text{ km s}^{-1}$  (see Table 5). At  $z \sim 2.2$ , Förster Schreiber et al. (2009) already noticed a similar trend from the SINS sample: dispersion-dominated systems are on average smaller than rotation-dominated ones.

The fraction of rotating systems is larger in MASSIV at  $z \sim 1.2$  than in the LSD/AMAZE sample at  $z \sim 3.3$ . Indeed, Gnerucci et al. (2010) found a lower limit of 34% of

rotators in their sample (11 out of 32 detected galaxies that they were able to classify). Their classification is the closest to ours since it relies both on velocity field modeling and on the agreement between morphological and kinematic position angle of the major axis. However, due to their small statistics and their different selection function it cannot be excluded that these proportions are compatible. At  $z \sim 2.2$ , the comparison with the SINS sample is more difficult due to the selection function, as for LSD/AMAZE, but also to the classification scheme which mainly relies on a kinemetry analysis (Shapiro et al. 2008) and on a visual inspection. They were able to unambiguously identify 18 rotating systems (Cresci et al. 2009), i.e. a lower fraction of 35% (18 out of 52 detected systems). They were also able to identify 14 dispersion-dominated systems (27% of the SINS sample) based on  $V_{max}/\sigma$  ratio. Considering only the reliably classified systems of SINS, we end up with similar fractions compared to MASSIV. At lower redshift, the results of the IMAGES sample ( $z \sim 0.6$ ) show that 63% of the sample show signs of rotation (both rotating disks and perturbed rotators classes, Puech et al. 2008). This fraction is higher than for MASSIV and favors an interpretation in which gas in star-forming systems is stabilizing into disks while the Universe evolves. As for the other comparisons, this conclusion has to be balanced with the various selection functions and classification methods. Concerning the selection, the various authors claim that they observe representative sets of star-forming galaxies in each redshift range.

In the MASSIV sample, the most massive galaxies ( $\log M_{star} > 10.5$ ) are mainly identified as disks in rotation. However, this is true for the gaseous phase and does not necessarily imply that the stars are settled into a disk. The best spheroid candidates may be the most compact and roundest massive galaxies. Indeed, elliptical galaxies can be flattened too but should be rounder than disks on average. There are four potential candidates even if only one of them has an axis ratio fully compatible with zero (see Figure 4). These may also be nearly face-on disks in case of very low observed velocity shear. In addition, given our definition of rotators, it is highly probable that gas and stars are within a common disk since both morphological and kinematic major axis are in good agreement. The morphology obtained from the CFHT imaging used for MASSIV has a too low spatial resolution in order to address unambiguously this issue but it is worth noticing that in the local Universe stellar disks are observed in elliptical galaxies (e.g. Kuntschner et al. 2010). Usually they are rather young ( $\sim 1$  Gyr) but they can also be as old as  $\sim 10$  Gyr which would be compatible with our observations.

The intermediate mass galaxies ( $\log M_{star} < 10.5$ ) are almost equally divided between rotating and non-rotating systems but the smallest ones are principally non-rotating systems (see Figure 4). Since both rotating and non-rotating systems are observed with small masses and radii, it is tentative to conclude that non-rotating systems are not due to observational artifacts. However, we cannot exclude the possibility that for some of the latter systems, when  $R_{last}/Seeing \sim 0.5$ , the absence of observed rotation is due to an episode of star formation in single non-resolved regions. The fact that we observe large non-rotating galaxies incompatible with face-on systems is also very intriguing. In addition, those with  $R_e > 2.8$  kpc are all in interaction. This property is probably related to the nature itself of these systems.

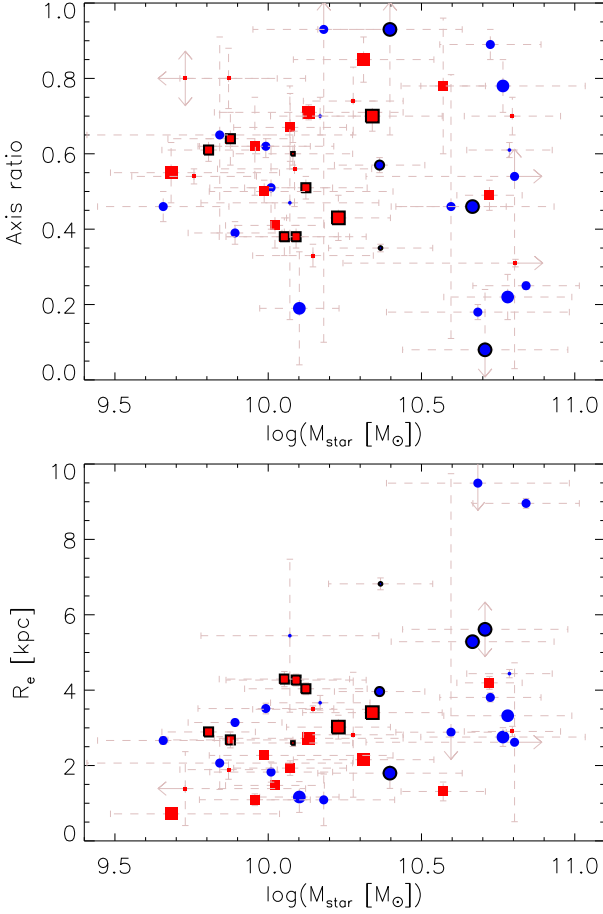


**Fig. 4.** **Top:** Axis ratio as a function of the stellar mass. **Bottom:** Half light radius as a function of the stellar mass. Blue dots and red squares represent respectively rotating and non-rotating galaxies. Symbols with black contours mark interacting galaxies. Symbol size is related to the SNR of the SINFONI data: small, medium and large symbols refers to galaxies with  $SNR < 5$ ,  $5 < SNR < 10$  and  $SNR > 10$  respectively. Arrows indicate that uncertainties are exceeding the displayed range.

### 5.2. Dynamical support of disks

In order to quantify the dynamical support, it is common to study the ratio of the rotation velocity over the local velocity dispersion. In Figure 5, we show this ratio as a function of the half-light radius. Only two out of the 20 secure rotators in MASSIV have a ratio lower than unity and are thus dispersion dominated. Only five out of these 20 secure rotators have  $V_{max}/\sigma < 2$  which indicates that the majority of rotating disks are clearly rotation-supported at  $z < 1.5$ . Moreover, there seems to exist a trend that the largest galaxies have the largest  $V_{max}/\sigma$  ratio. As seen in Table 5, for rotators, the median velocity dispersion is  $\sigma = 62 \text{ km s}^{-1}$ . In addition, the median rotation velocity  $V_{max} = 141 \text{ km s}^{-1}$  and the median  $V_{max}/\sigma$  ratio is 3.2. By restricting the analysis on rotating systems with  $R_e > 3.2 \text{ kpc}$  (median for all rotators), we end up with ten objects with a median velocity dispersion  $\sigma = 49 \text{ km s}^{-1}$ , a median rotation velocity  $V = 201 \text{ km s}^{-1}$  and a median  $V_{max}/\sigma = 3.7$  which clearly indicates that the largest disks are more stable. This seems to be supported in Figure 6 where we

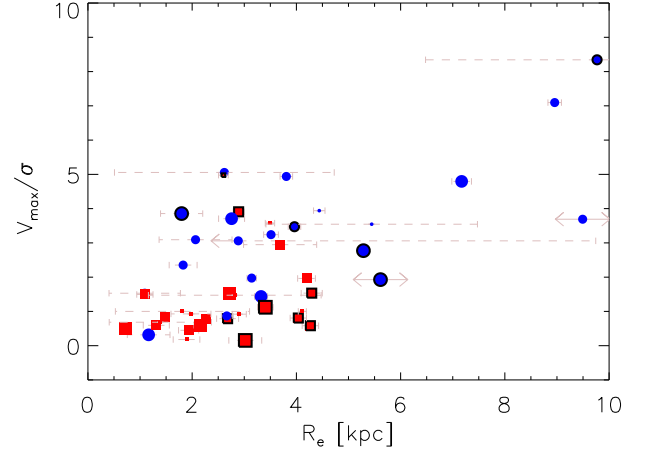


**Fig. 5.**  $V_{max}/\sigma$  as a function of the half light radius. Blue dots and red squares represent respectively rotating and non-rotating galaxies. Symbols with black contours mark interacting galaxies. Symbol size is related to the SNR of the SINFONI data: small, medium and large symbols refers to galaxies with  $SNR < 5$ ,  $5 < SNR < 10$  and  $SNR > 10$  respectively. Arrows indicate that uncertainties are exceeding the displayed range.

clearly see that the velocity dispersion is low for the largest rotators ( $R_e > 6 \text{ kpc}$ ).

At higher redshift, rotators in the LSD/AMAZE sample ( $z \sim 3.3$ ) have a typical gaseous velocity dispersion of  $\sigma = 90 \text{ km s}^{-1}$  and  $V_{max}/\sigma \sim 1.6$  (Gnerucci et al. 2010) whereas in the SINS sample ( $z \sim 2.2$ ), Cresci et al. (2009) found  $\sigma = 52 \text{ km s}^{-1}$  and  $V_{max}/\sigma \sim 4.5$  as median values for their unambiguous rotators. The comparison with SINS is not straightforward since they have made these measurements only for a fraction of these systems (12 out of 18). For their sample of rotating systems, the median rotation velocity is  $V_{max} \sim 240 \text{ km s}^{-1}$  and the median half-light radius (using the conversion between half-light radius and disk scale length  $R_e = 1.68R_d$  valid for an exponential disk distribution) is  $R_e = 3.4 \text{ kpc}$ . These median values are larger than those we obtain for our sample of 20 rotating galaxies ( $V_{max} \sim 140 \text{ km s}^{-1}$  and  $R_e = 3.2 \text{ kpc}$ ) which indicates that while their sample of rotation-dominated galaxies probes the massive disks population at  $z \sim 2.2$ , our sample of rotating systems spans a wider range in term of dynamical mass. At lower redshift, from the IMAGES sample ( $z \sim 0.6$ ), the typical gaseous velocity dispersion is  $\sigma \sim 45 \text{ km s}^{-1}$  and  $V_{max}/\sigma \sim 4$  considering both rotating disks and perturbed rotators, with a trend for higher  $V_{max}/\sigma$  for rotating disks (Puech, private communication). The GHASP sample is the largest 2D kinematics sample of local spiral galaxies with star-formation rates typical of the local Universe. We consider here the sub-sample of 136 galaxies that we have projected at  $z \sim 1.33$  with similar spatial resolution conditions than the MASSIV sample (see section 3.2.3). These galaxies have a median optical radius of  $8.5 \text{ kpc}$ . Since  $R_{opt} \sim 1.9R_e$  for an exponential disk distribution, this gives a median half-light radius of  $4.5 \text{ kpc}$ . The median rotational velocity is  $164 \text{ km s}^{-1}$ , the median velocity dispersion is  $24 \text{ km s}^{-1}$  and the median  $V_{max}/\sigma$  is  $\sim 7$ . Despite the small differences observed from  $z \sim 2.2$  to  $z \sim 0.6$ , observations of various samples suggest a trend of decreasing velocity dispersion with decreasing redshift.

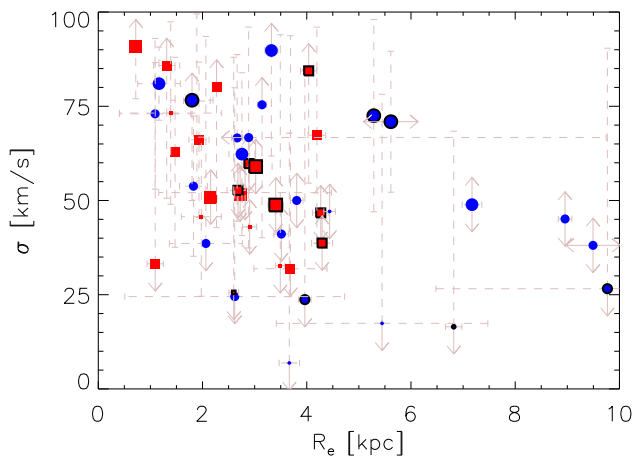


**Fig. 6.** Velocity dispersion as a function of the effective radius. Blue dots and red squares represent respectively rotating and non-rotating galaxies. Symbols with black contours mark interacting galaxies. Symbol size is related to the SNR of the SINFONI data: small, medium and large symbols refers to galaxies with  $SNR < 5$ ,  $5 < SNR < 10$  and  $SNR > 10$  respectively. Arrows indicate that uncertainties are exceeding the displayed range.

Associated to local and  $z \sim 3$  observations, this supports the idea that the gaseous phase of galaxy disks gets less turbulent with cosmic time.

We also observe that around half of the sample of rotators has a gaseous velocity dispersion unambiguously larger than  $60 \text{ km s}^{-1}$ . These may be interpreted as clumpy disks. Indeed, it has been claimed that a high velocity dispersion is expected for clumpy disks created from a smooth cold gas accretion (e.g. Bournaud & Elmegreen 2009). This mode of accretion is believed to be more efficient at  $z > 2$  (Kereš et al. 2009) and it is thus not surprising to observe also a significant fraction of galaxies in MASSIV that resemble stable rotating disks with velocity dispersions compatible with  $\sim 20 - 50 \text{ km s}^{-1}$  (cf. figure 7).

We also point out that the gaseous velocity dispersion is not significantly different when considering non-rotating systems which raises the question of the origin of such a gaseous velocity dispersion. If these non-rotating systems are in fact transient mergers of star-forming disks in an unstable phase, then a high velocity dispersion is expected (Bournaud et al. 2011), but then it is more difficult to explain cases of large non-rotating galaxies with relatively low gaseous velocity dispersion.

As pointed out by e.g. Lehnert et al. (2009); Green et al. (2010); Le Tiran et al. (2011), star formation might be responsible for the gaseous turbulence. In particular star formation intensity might be correlated with gaseous velocity dispersion. Within this hypothesis, the lowering of the velocity dispersion from high to low redshift might be explained by the fact that the samples discussed in this paper have on average a decreasing star formation rate from  $z \sim 3$  to  $z = 0$  (see Contini et al. 2011). This behaviour is due to cosmological surface brightness dimming but also to galaxy evolution itself: galaxies are getting bigger and form less stars from  $z \sim 2$  to  $z = 0$ . The relations between star formation and velocity dispersion will be addressed with the full MASSIV sample in a forthcoming paper.

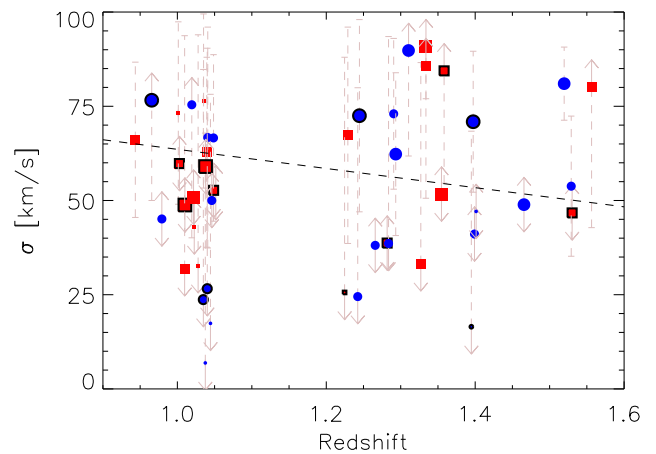


**Fig. 7.** Velocity dispersion as a function of the redshift. Blue dots and red squares represent respectively rotating and non-rotating galaxies. Symbols with black contours mark interacting galaxies. Symbol size is related to the SNR of the SINFONI data: small, medium and large symbols refers to galaxies with  $SNR < 5$ ,  $5 < SNR < 10$  and  $SNR > 10$  respectively. The dotted line represents the velocity dispersion corresponding to the spectral PSF of SINFONI. Arrows indicate that uncertainties are exceeding the displayed range.

### 5.3. Importance of merging at $z \sim 1.2$

The proportion of interacting galaxies in our sample is at least 29% (13 interacting systems with flag “A” or “B” out of the 45 detected systems with  $0.9 < z < 1.6$ ) and is 32% if we only consider the 41 systems having a flag “A” or “B” in the redshift range  $0.9 < z < 1.6$ . Due to our method to determine which systems are in interaction, this proportion is a lower limit. Indeed, on the one hand, it could be that a fraction of non-rotating galaxies are on-going mergers or merger remnants. On the other hand, close mergers could mimic rotators (elongation and velocity gradient along a common axis), as it is the case for VVDS020294045 (see Appendix A). In addition, due to the non circular final field-of-view of our SINFONI data we only cover a fraction of the area at a given radius around our targets. There is also a substantial fraction of objects for which close galaxies are observed in I-band but not in SINFONI datacubes (see Appendix A). It is possible that a fraction of these objects are passive galaxies at the same redshift as the MASSIV targets. It is interesting to notice that on average, galaxies in interaction are larger than isolated galaxies and have a lower gaseous velocity dispersion (see Table 5).

The proportion of interacting systems in MASSIV is comparable to the fraction of mergers in the SINS sample. However, SINS mergers (around one third of the sample) are mainly identified using kinemetry, a technique based on the degree of perturbation observed in the kinematic maps, whereas the 29% of interacting galaxies in MASSIV are mainly based on the detection of several components. On the one hand, only three pairs out of 52 detected systems were identified in SINS (and three pairs out of 29 systems in the LSD/AMAZE sample), which is much lower than the pair fraction observed in MASSIV. On the other hand, SINS mergers found from kinemetry may mainly correspond to our non-rotating galaxies (see Section 4.4). That

means that using this latter method, we would probably find that some MASSIV isolated galaxies are likely mergers. This is further supported by the fact that the fraction of non-rotating systems is larger in interacting galaxies: among the 11 systems with interactions in the sample (with both  $\text{SNR} > 5$  and isolation flag “A” or “B”), seven have at least one non-rotating component (64%) whereas among the 22 isolated systems (with both  $\text{SNR} > 5$  and isolation flag “A” or “B”), there is only eight non-rotating galaxies (36%). This could indicate that some isolated non-rotating galaxies are in fact on-going mergers or merger remnants. This seems to be also supported by the number of interacting galaxies that is larger at  $z \sim 1$  (e.g. Figure 7). The conclusion is thus that the fraction of mergers at  $z \sim 1.2$  is larger than at  $z \sim 2.2$  as observed in SINS.

At lower redshift, 44% of galaxies in the IMAGES sample have complex kinematics that could be explained by on-going mergers of star-forming galaxies (Yang et al. 2008). This is more than the proportion of interacting galaxies in MASSIV. However, as for the comparison with SINS, the definition of galaxies with complex kinematics is probably closer to our definition of non-rotating galaxies and the proportions of these two classes in each sample are fully comparable. It is probable that for IMAGES, a larger field of view would have led to the detection of close companions. Thus a direct comparison of merging with MASSIV is not straightforward.

From the pair number we have a higher number of mergers than SINS. Considering complex systems, our results are still consistent with a peak in the merger activity at  $1 < z < 2$ . However, it is not yet clear if these kinematic signatures of mergers are related to minor or major mergers whereas from the MASSIV sample we have a way to infer the mass ratio between pair members. A dedicated analysis on the merger rate from the observed pairs will be performed from the entire MASSIV sample (López-Sanjuan et al., in prep) and will probably enable to infer the rate of observed on-going mergers.

#### 5.4. Nature of non-rotating galaxies

It appears clearly that the non-rotating systems are mainly galaxies classified as low velocity shear galaxies plus some interacting galaxies. Among the 16 (and eight additional with  $\text{SNR} < 5$ ) low velocity shear galaxies only three (and two additional that have very poor SNRs) of them could be considered as rotating. Two of these galaxies are compatible with nearly face-on systems. The exact nature of these non-rotating objects is still unclear. Such a population of galaxies has already been observed at higher redshift both in the SINS sample at  $z \sim 2.2$  and in the LSD/AMAZE sample at  $z \sim 3.3$ . These objects are smaller on average than rotators and are often associated to interacting systems (see Table 5).

An unexpected trend is observed for these objects in the MASSIV sample (Figure 6): there exists an anti-correlation between the mean velocity dispersion of the gas and the effective radius of the stellar component. This correlation is the contrary of what would be expected for elliptical galaxies located in the fundamental plane (Dressler et al. 1987; Djorgovski & Davis 1987). However, the fundamental plane applies for the central stellar velocity dispersion which is a quantity that cannot be currently measured in high-redshift galaxies from spectroscopic data. Alternatively,

this correlation could reflect a beam smearing effect since an unresolved velocity gradient could reproduce this trend. However, the fact that we also observe velocity gradients in other galaxies with similar sizes is against such an interpretation but this is closely linked to the spatial distribution of the ionized gas. In the case of face-on disks (possible only for low velocity shear galaxies), it would be expected to recover the same trend than for rotators (i.e. lower velocity dispersion for large disks). This is however very unlikely since velocity gradients may be observed for the largest galaxies and also because we do not expect to observe more than four galaxies with an inclination lower than  $20^\circ$  (see Figure 2). It could however be that the gas being more concentrated collapses more violently to form stars at a higher density if we consider that star formation can drive the gaseous velocity dispersion as suggested by e.g. Green et al. (2010).

As it has been proposed in the previous sections, these non-rotating objects could be interpreted as:

- Merger remnants in a transient unstable state for the gaseous phase (e.g. collapse of gas due to interaction, anti-spin mergers, etc.).
- Rotators with a special gaseous distribution: the most plausible being a unique highly concentrated star-forming region when galaxies are small.
- Galaxies with an unstable gaseous phase. This could be supported by the relatively low mass (thus a low potential well) of these systems.
- Nearly face-on disks (for low velocity shear galaxies only): this would explain the similar velocity dispersion as for the rotators but the number of such galaxies is statistically low.
- Spheroids: however (i) these galaxies may be the most massive ones, (ii) there is no reason to think that the gas is not in a disk as observed at lower redshift (e.g. Peletier et al. 2007 in early-type spirals; e.g. Bournaud et al. 2007 in numerical simulations of gas-rich mergers) and (iii) if the gas is randomly distributed, a larger velocity dispersion than for rotators would be expected.

## 6. Summary and conclusions

This paper presents the data and its processing for a subsample of 50 galaxies of the MASSIV sample (described in Contini et al. 2011). It focuses on the analysis of the dynamical state of galaxies using kinematic maps derived from SINFONI data-cubes. We have classified this sample based on the modeling of these maps and based on a comparison between morphology and kinematics. This classification describes on the one hand the rotating or non-rotating nature of the objects and on the other hand the close environment of galaxies.

We have separated rotating galaxies and non-rotating galaxies based on two arguments: (i) the agreement between morphological and kinematic major axis position angle and (ii) the accuracy of the description of a rotating disk model. We show that around half of the sample displays rotation whereas one third does not show a dominant ordered rotation (the remaining fraction is not classified). However, the ionized gas turbulence in these two classes is similar ( $\sigma \sim 60 \text{ km s}^{-1}$ ) which marks a transition between higher redshift galaxies showing on average a larger velocity dispersion ( $\sigma \sim 60 - 90 \text{ km s}^{-1}$ ), as in SINS at  $z \sim 2.2$  or



LSD/AMAZE at  $z \sim 3.3$ , and lower galaxies in IMAGES at  $z \sim 0.6$  and GHASP at  $z = 0$ , which are characterized by a lower velocity dispersion ( $\sigma \sim 20 - 40 \text{ km s}^{-1}$ ). All these samples are 3D-spectroscopic samples observing ionized gas emission lines. This transition of the gaseous velocity dispersion seen from these high to low redshift samples is partly responsible for the increase of the rotational support (deduced from the  $V_{\text{max}}/\sigma$  ratio) when galaxies evolve. It could be related to a common process that would induce a decrease of the star formation rate. We observe that around half of our galaxies have a velocity dispersion compatible with that in local star-forming galaxies whereas the other half is more compatible with galaxies at higher redshift. At high redshift, this high velocity dispersion seen in isolated disks is though to be due to a mass assembly driven by cold flows. In this framework, our results suggest that at  $z \sim 1.2$  cold gas accretion is less efficient than at larger redshift but more efficient than at lower redshift, consistent with cosmological simulations (Kereš et al. 2005). When we compare our sample to these other high redshift samples, it seems that the fraction of disks increases in star-forming galaxies while the Universe evolves.

By studying strong kinematic signatures of merging and detecting pairs in our data-cubes and broad band images, we have shown that the fraction of interacting galaxies is up to at least one third of the sample. The fraction of non-rotating object in these systems is higher than in isolated ones. This suggests that a significant fraction of isolated non-rotating objects could be mergers in a transient state in which the gas is not dynamically stable. However, the nature of non-rotators is still unclear. Compared to higher and lower redshift 3D-spectroscopic surveys, our findings seem to indicate that at the peak of star formation activity, the fraction of star-forming galaxies in interaction is also at its maximum, corresponding to a peak in the merging activity (Ryan et al. 2008; Conselice et al. 2008; López-Sanjuan et al. 2009).

All these results favor a scenario in which the mass assembly of star-forming galaxies is progressively shifting from a predominance of smooth cold gas accretion to a predominance of merging as cosmic time evolves, with a transition epoch around a redshift  $z \sim 1 - 1.5$ .

*Acknowledgements.* We thank the referee for useful comments that helped in improving the paper. This work has been partially supported by the CNRS-INSU and its Programme National Cosmologie-Galaxies (France) and by the French ANR grant ANR-07-JCJC-0009

## References

- Basu-Zych, A. R., Gonçalves, T. S., Overzier, R., et al. 2009a, *ApJ*, 699, L118
- Basu-Zych, A. R., Schiminovich, D., Heinis, S., et al. 2009b, *ApJ*, 699, 1307
- Basu-Zych, A. R., Schiminovich, D., Johnson, B. D., et al. 2007, *ApJS*, 173, 457
- Bell, E. F., Wolf, C., Meisenheimer, K., et al. 2004, *ApJ*, 608, 752
- Bonnet, H., Abuter, R., Baker, A., et al. 2004, *The Messenger*, 117, 17
- Bouché, N., Dekel, A., Genzel, R., et al. 2010, *ApJ*, 718, 1001
- Bournaud, F., Chapon, D., Teyssier, R., et al. 2011, *ApJ*, 730, 4
- Bournaud, F. & Elmegreen, B. G. 2009, *ApJ*, 694, L158
- Bournaud, F., Jog, C. J., & Combes, F. 2007, *A&A*, 476, 1179
- Cassata, P., Le Fèvre, O., Garilli, B., et al. 2010, ArXiv e-prints
- Conselice, C. J., Rajgor, S., & Myers, R. 2008, *MNRAS*, 386, 909
- Contini, T., Garilli, B., Le Fèvre, O., et al. 2011, ArXiv e-prints
- Cresci, G., Hicks, E. K. S., Genzel, R., et al. 2009, *ApJ*, 697, 115
- de Ravel, L., Le Fèvre, O., Tresse, L., et al. 2009, *A&A*, 498, 379
- Dekel, A. & Birnboim, Y. 2006, *MNRAS*, 368, 2
- Dekel, A., Birnboim, Y., Engel, G., et al. 2009, *Nature*, 457, 451
- Djorgovski, S. & Davis, M. 1987, *ApJ*, 313, 59
- Dressler, A., Lynden-Bell, D., Burstein, D., et al. 1987, *ApJ*, 313, 42
- Eisenhauer, F., Abuter, R., Bickert, K., et al. 2003, in Society of Photo-Optical Instrumentation Engineers (SPIE) Conference Series, Vol. 4841, Society of Photo-Optical Instrumentation Engineers (SPIE) Conference Series, ed. M. Iye & A. F. M. Moorwood, 1548–1561
- Epinat, B., Amram, P., Balkowski, C., & Marcelin, M. 2010, *MNRAS*, 401, 2113
- Epinat, B., Amram, P., & Marcelin, M. 2008a, *MNRAS*, 390, 466
- Epinat, B., Amram, P., Marcelin, M., et al. 2008b, *MNRAS*, 388, 500
- Epinat, B., Contini, T., Le Fèvre, O., et al. 2009, *A&A*, 504, 789
- Flores, H., Hammer, F., Puech, M., Amram, P., & Balkowski, C. 2006, *A&A*, 455, 107
- Förster Schreiber, N. M., Genzel, R., Bouché, N., et al. 2009, *ApJ*, 706, 1364
- Förster Schreiber, N. M., Genzel, R., Lehnert, M. D., et al. 2006, *ApJ*, 645, 1062
- Garilli, B., Le Fèvre, O., Guzzo, L., et al. 2008, *A&A*, 486, 683
- Genel, S., Genzel, R., Bouché, N., et al. 2008, *ApJ*, 688, 789
- Genzel, R., Burkert, A., Bouché, N., et al. 2008, *ApJ*, 687, 59
- Gnerucci, A., Marconi, A., Cresci, G., et al. 2010, ArXiv e-prints
- Gonçalves, T. S., Basu-Zych, A., Overzier, R., et al. 2010, *ApJ*, 724, 1373
- Green, A. W., Glazebrook, K., McGregor, P. J., et al. 2010, *Nature*, 467, 684
- Hopkins, A. M. & Beacom, J. F. 2006, *ApJ*, 651, 142
- Kereš, D., Katz, N., Weinberg, D. H., & Davé, R. 2005, *MNRAS*, 363, 2
- Kereš, D., Katz, N., Fardal, M., Davé, R., & Weinberg, D. H. 2009, *MNRAS*, 395, 160
- Kuntschner, H., Emsellem, E., Bacon, R., et al. 2010, *MNRAS*, 408, 97
- Law, D. R., Steidel, C. C., Erb, D. K., et al. 2009, *ApJ*, 697, 2057
- Lawrence, A., Warren, S. J., Almaini, O., et al. 2007, *MNRAS*, 379, 1599
- Le Fèvre, O., Vettolani, G., Garilli, B., et al. 2005, *A&A*, 439, 845
- Le Tiran, L., Lehnert, M. D., Di Matteo, P., Nesvadba, N. P. H., & van Driel, W. 2011, *A&A*, 530, L6+
- Lehnert, M. D., Nesvadba, N. P. H., Tiran, L. L., et al. 2009, *ApJ*, 699, 1660
- Lin, L., Patton, D. R., Koo, D. C., et al. 2008, *ApJ*, 681, 232
- López-Sanjuan, C., Balcells, M., Pérez-González, P. G., et al. 2009, *A&A*, 501, 505
- López-Sanjuan, C., Le Fèvre, O., de Ravel, L., et al. 2011, *A&A*, 530, A20+
- Markwardt, C. B. 2009, in Astronomical Society of the Pacific Conference Series, Vol. 411, Astronomical Society of the Pacific Conference Series, ed. D. A. Bohlender, D. Durand, & P. Dowler, 251
- McCracken, H. J., Radovich, M., Bertin, E., et al. 2003, *A&A*, 410, 17
- Modigliani, A., Hummel, W., Abuter, R., et al. 2007, ArXiv Astrophysics e-prints
- Neichel, B., Hammer, F., Puech, M., et al. 2008, *A&A*, 484, 159
- Overzier, R. A., Heckman, T. M., Kauffmann, G., et al. 2008, *ApJ*, 677, 37
- Peletier, R. F., Falcón-Barroso, J., Bacon, R., et al. 2007, *MNRAS*, 379, 445
- Peng, C. Y., Ho, L. C., Impey, C. D., & Rix, H.-W. 2002, *AJ*, 124, 266
- Press, W., Teukolsky, S., Vetterling, W., & Flannery, B. 1992, *Numerical Recipes in C*, 2nd edn. (Cambridge, UK: Cambridge University Press)
- Puech, M., Flores, H., Hammer, F., et al. 2008, *A&A*, 484, 173
- Queyrel, J., Contini, T., Kissler-Patig, M., et al. 2011, ArXiv e-prints
- Rodrigues, M., Hammer, F., Flores, H., et al. 2008, *A&A*, 492, 371
- Ryan, Jr., R. E., Cohen, S. H., Windhorst, R. A., & Silk, J. 2008, *ApJ*, 678, 751
- Sarzi, M., Falcón-Barroso, J., Davies, R. L., et al. 2006, *MNRAS*, 366, 1151
- Sersic, J. L. 1968, *Atlas de galaxies australes*, ed. Sersic, J. L.
- Shapiro, K. L., Genzel, R., Förster Schreiber, N. M., et al. 2008, *ApJ*, 682, 231
- Shapiro, K. L., Genzel, R., Quataert, E., et al. 2009, *ApJ*, 701, 955
- Tresse, L., Ilbert, O., Zucca, E., et al. 2007, *A&A*, 472, 403

Williams, R. J., Quadri, R. F., Franx, M., van Dokkum, P., & Labbé, I. 2009, *ApJ*, 691, 1879  
 Xu, X., Narayanan, D., & Walker, C. 2010, *ApJ*, 721, L112  
 Yang, Y., Flores, H., Hammer, F., et al. 2008, *A&A*, 477, 789

## Appendix A: Individual comments

**VVDS020106882** This galaxy has a regular velocity field. The velocity dispersion is larger on the South-East side but remains low. Some external pixels are detected on the North-West side. They seem to be related to regions associated to the galaxy due to concordant velocities. Two objects (including a very faint one) are detected in I-band at less than  $6''$  but are not detected in the SINFONI datacube.

**VVDS020116027** This galaxy has a small companion at  $4''$  on the North. The companion is detected in  $H\alpha$  but with a low SNR and over a region of the size of the seeing. This companion is less exposed than the main galaxy. The main galaxy itself seems to have two components in the  $H\alpha$  flux distribution and has a very low velocity shear.

**VVDS020147106** Despite a low velocity gradient and some perturbations in the low SNR regions, the kinematic position angle of this galaxy is in good agreement with the I-band morphology. This galaxy may thus be a nearly face-on disk (at least the ionized gas) but with a large velocity dispersion. There are several objects detected in I-band but not in the SINFONI datacube at less than  $6''$ .

**VVDS020149061** The I-band image suggests small and extremely faint companions that are however not detected in the SINFONI datacube. The seeing is half the size of the  $H\alpha$  emission. The velocity field is irregular on the edges where the SNR is lower and the velocity dispersion is larger than  $70 \text{ km s}^{-1}$  everywhere in the galaxy (except at the edges).

**VVDS020164388** Except for the edge, the velocity field and the velocity dispersion map are regular. Velocity dispersion is not larger than  $60 \text{ km s}^{-1}$ . In the I-band image, the galaxy is rather round. Several faint close objects are also observed in this image but are not detected in  $H\alpha$ .

**VVDS020167131** Some [OIII] is detected in the center but there is only a few pixels and the SNR is lower than 4. In addition, some emission line is detected at the same redshift in the center of the galaxy on the East seen in the I-band. This indicates that these two galaxy are in interaction.

**VVDS020182331** The velocity gradient is clear even if we exclude low SNR regions (bluest and reddest velocities). However, the velocity field and velocity dispersion map look perturbed, probably due to the low SNR of the observation. In the I-band image, there is a very close companion that is undetected in  $H\alpha$ .

**VVDS020193070** Despite a globally low SNR, the velocity field is quite regular except in the outskirts. The velocity dispersion is low but a bit asymmetric. The

morphology is elongated both in I-band and in  $H\alpha$  (but with a difference of  $\sim 10^\circ$  between morphological and kinematic major axis position angles). Three very faint objects are detected at less than  $5''$  from the galaxy but are not detected in  $H\alpha$ .

**VVDS020208482** The SNR is rather low but there is however a clear velocity shear. The I-band image shows a close galaxy and other further objects that are not detected in  $H\alpha$ .

**VVDS020214655** This galaxy displays a rather smooth low velocity gradient, but not aligned with the morphology which is rather round. There are some perturbations in the low SNR regions of the velocity field. There are also small perturbations in the velocity dispersion map that is rather flat and with low values. There is a close galaxy in the I-band (at  $\sim 2''$ ) that is not detected in  $H\alpha$ .

**VVDS020239133** The morphology from I-band is well elongated and is more extended than the  $H\alpha$ . The velocity field is asymmetric but shows a clear gradient. The velocity dispersion map is also perturbed and has a large velocity dispersion in the south that could be explained by a sky line residual. Two objects are observed in I-band but not detected in  $H\alpha$  within the SINFONI field-of-view.

**VVDS020240675** The velocity field is perturbed, with a low velocity gradient. The velocity dispersion is rather low ( $\sim 40 \text{ km s}^{-1}$ ). In addition, the size of the  $H\alpha$  emission is not large compared to the seeing. There is some emission detected at  $2''$  at the East of the main galaxy, but nothing is detected in the I-band at this location. There are also several objects in I-band within  $6''$  that are not detected in  $H\alpha$ .

**VVDS020255799** The signal in  $H\alpha$  for this galaxy is not extended and with a mean SNR lower than 5. There is no clear regular velocity gradient. One object is detected at  $5''$  in I-band but not in  $H\alpha$ .

**VVDS020261328** The velocity field is not completely regular both in the blue and red sides. There is also a peak in the velocity dispersion where the SNR is lower. Several objects are detected in I-band but not in  $H\alpha$ .

**VVDS020278667** Some  $H\alpha$  is detected, but the extent is lower than the seeing, and the SNR is lower than 5. Thus its classification is very doubtful. There is a close galaxy ( $\sim 1.5''$ ) in the I-band but it is not detected in  $H\alpha$ .

**VVDS020283083** This galaxy looks asymmetric in the I-band and this coincides with the  $H\alpha$  distribution and with the main perturbation of the velocity field. This could be related to a tidal tail. That is why this galaxy is classified as non-isolated.

**VVDS020283830** In the  $H\alpha$  flux map there is a faint detection smaller than the seeing that coincides with a detection in the I-band (North-East). For the main object, the distribution is asymmetric. This is also true in the  $H\alpha$  distribution that is clumpy. These clumps may be either star forming regions in one single rotating galaxy or two small objects in the process of merging.



**VVDS020294045** The global velocity gradient is larger than  $50 \text{ km s}^{-1}$ . However, both the I-band and the  $\text{H}\alpha$  images are consistent with a system involving two components: one main component with a low velocity gradient (South) and one small component with a size comparable to the seeing (North). This interpretation is supported by the high velocity dispersion between the two components due to beam smearing between the two components at different radial velocities. There is a sky line residual at the velocity of the small component, but the flux detected is noticeable. It is thus not possible to classify the small component. This system is classified as interacting with a flag B since it could also be a single object but with strong perturbations.

**VVDS020363717** The I-band shows a close ( $\sim 1''$ ), very diffuse and faint object that is not detected in the  $\text{H}\alpha$  (South-West). The velocity shear is low. The velocity field is perturbed in the low SNR regions. The velocity dispersion map is also perturbed and the velocity dispersion is large ( $\sim 90 \text{ km s}^{-1}$ ) after beam smearing correction.

**VVDS020370467** Both velocity field and velocity dispersion map are perturbed. The velocity gradient of the model is low and the velocity dispersion is rather high (larger than  $70 \text{ km s}^{-1}$ ) in particular in the North edge (larger than  $150 \text{ km s}^{-1}$ ). This could be a sign for a strong interaction due to merging, but there is also a sky line residual that could induce the line width. In addition some objects are observed in the I-band image at less than  $6''$  but are not detected in  $\text{H}\alpha$ .

**VVDS020386743** The  $\text{H}\alpha$  distribution is very elongated for this galaxy, but no velocity gradient is visible. Both velocity field and velocity dispersion are smooth. The I-band image shows a distorted galaxy compatible with the  $\text{H}\alpha$  distribution. On the North, the distortion is compatible with a faint detection in  $\text{H}\alpha$  that could be related to a minor close companion.

**VVDS020461235** The velocity field of this galaxy is perturbed. There is a blob detected in  $\text{H}\alpha$  in the South-West side. This blob is also suggested in the I-band morphology but is less clear. This blob has velocities compatible with the rotation of the main component but could as well be a minor companion in the process of merging. This system is thus classified as interacting with a flag B.

**VVDS020461893** The velocity field is regular but the velocity dispersion is less regular and high and could suggest a high dispersion clump. An object is observed at  $3''$  southward in the I-band image but is not detected in SINFONI data.

**VVDS020465775** Both velocity field and velocity dispersion map are irregular. The gradient of the model is lower than  $50 \text{ km s}^{-1}$ . We claim that there is a companion on the north west that induces broad and non Gaussian (hence a lower SNR) lines interpreted as a sign of interaction that could also be responsible for the asymmetry in the I-band. Hence it is classified as interacting with a flag B since it could also be a single object but with strong

perturbations.

**VVDS140083410** The velocity field is perturbed and there is no clear overall velocity gradient. No galaxy is detected at less than  $8''$  in the I-band image.

**VVDS140096645** The velocity field is smooth but with some perturbations along the minor kinematic axis. The velocity dispersion map is perturbed and larger on the southern side probably due partially to a sky line residual. Some emission is detected in the  $\text{H}\alpha$  map outside the main component (North). This detection is smaller than the seeing and is not clearly confirmed in the I-band morphology (CFHT12k images are less deep than CFHTLS images). It could be a minor companion but it is also compatible with the velocity of the main component and could be associated to it. Thus it is classified as interacting with a flag B. This galaxy also has an AGN (see Queyrel et al. 2011).

**VVDS140123568** Some  $\text{H}\alpha$  is detected, but there is only a few pixels and the SNR is lower than 4. Thus its classification is very doubtful. In the I-band image, there is no detected object at less than  $6''$  around the galaxy. Since the kinematics does not allow to investigate a possible on-going merger, the isolation has a flag B.

**VVDS140137235** Some  $\text{H}\alpha$  is detected, but there is only a few pixels and the SNR is lower than 4. Thus its classification is very doubtful. In the I-band image, there is no detected objects at less than  $6''$  around the galaxy. Since the kinematics does not allow to investigate a possible on-going merger, the isolation has a flag B.

**VVDS140217425** The velocity field is regular and has the largest shear ( $\sim 600 \text{ km s}^{-1}$ ). The velocity dispersion map shows two regions with large velocity dispersions ( $> 150 \text{ km s}^{-1}$ ). These regions are associated with a lower SNR. This is due to the fact that there are double profiles in these regions that induce a non optimal fit. These double profiles are due to the beam smearing that mix regions with different velocities. This can be interpreted as the presence of star-forming clumps at the edge of the galaxy and a large clump in the center. The decomposition of the profile using two Gaussian scales down the velocity dispersion to usual values, and shows that the two external clumps have no velocity gradient whereas the central one has a velocity gradient. This picture is compatible with a rotating disk in which the rotational velocity reach a plateau before the external clumps. Using the double profile decomposition instead of the kinematics model to derive the maximum velocity, we find  $V_{max} \sim 312 \pm \sim 20 \text{ km s}^{-1}$ , which is much more realistic than the value found from the model. The velocity of the plateau are respectively  $\sim +313$  and  $\sim -312$  which shows that the rotation curve is fairly symmetric and thus in favor for a rotating disk hypothesis. Correcting for the inclination, we obtain  $V_{max} = 322 \text{ km s}^{-1}$ . However, the I-band image is asymmetric (which is not incompatible with the previous statement), and it cannot be ruled out that the external clumps are in fact objects about merging with the main component.

**VVDS140258511** The velocity field and velocity

dispersion map look perturbed on the North-East edge but this may be due to a sky line residual. Except at this location, the velocity dispersion is low (less than  $40 \text{ km s}^{-1}$ ).

**VVDS140262766** The velocity field and the velocity dispersion map are not strongly perturbed and the velocity dispersion is around  $50 \text{ km s}^{-1}$ . Several objects are seen at less than  $5''$  in the I-band image but are not detected in  $\text{H}\alpha$ .

**VVDS140545062** This object has a clear and smooth velocity shear compatible with the I-band and  $\text{H}\alpha$  morphology. However, the velocity field is not very well reproduced by the rotating disk model: one side is faster than the other. The velocity dispersion map shows a peak in the South-West side. This peak is due to the presence of a double profile that may be interpreted as a sign of merging (late stage or on-going merger). However, since the system as a whole is isolated (no galaxy at less than  $7''$  in I-band), this galaxy was classified as isolated with a flag B.

**VVDS220014252** Both velocity field and velocity dispersion map are perturbed. In addition, the morphology in I-band is asymmetric. This system has a large velocity dispersion ( $> 80 \text{ km s}^{-1}$ ) and is peaked on some edges. This may be a sign of merging (on-going or remnant). However, the system is isolated and there is no other evidence for some companion except one very faint object in I-band at  $\sim 5''$  which is not in SINFONI field-of-view. So this system is classified as isolated.

**VVDS220015726** The velocity field of this galaxy is well reproduced by a rotating disk model. The velocity dispersion map is peaked in the center, which is in agreement with the expected effect of beam smearing due to the inner velocity gradient. The velocity field and velocity dispersion map are slightly perturbed. One very faint component is detected in I-band at around  $4''$  but is not detected in  $\text{H}\alpha$ .

**VVDS220148046** This galaxy has been observed using adaptive optics and is thus less deep than seeing-limited observations. Some emission line was detected but with a low SNR ( $\sim 4$ ). It appears that the redshift determined from the VVDS was wrong and that we observed [OIII] at  $z = 2.2442$ . The emission is compact and thus it is not possible to conclude about the kinematics.

**VVDS220376206** A small component (smaller than the seeing, hence a flag B for the environment classification) is detected in  $\text{H}\alpha$  and is confirmed in the I-band image (North). The residual velocity field shows signs of interaction. The main component has two blobs in  $\text{H}\alpha$  and the I-band morphology is slightly asymmetric. The velocity dispersion map is also perturbed and peaked on the edges. This may be a sign of interaction or of the end of a merging event.

**VVDS220386469** This observation has been done using adaptive optics and is underexposed (due to the small pixel size, cf. Contini et al. 2011). Even if the adaptive optics observation does not allow a fair comparison with other galaxies in the same conditions due to the

smaller field of view, this system is classified as isolated with a flag B since the closest clear detection in the I-band image is farther than the  $6''$  that would be reached using the seeing-limited observing strategy. The velocity field is irregular and the velocity dispersion is very small but this may be due to the use of AO that provides more details and a lower SNR than seeing-limited observations. The extent of the velocity field is small so it is difficult to argue that there is no velocity gradient at all in this galaxy.

**VVDS220397579** This system is the clearest interacting system between two large galaxies. The two objects are detected in  $\text{H}\alpha$  and in the I-band. Both are elongated toward the same direction. The main object in  $\text{H}\alpha$  and in I-band has a smooth velocity field with no gradient except on the northern side, near the companion. This region coincides with a larger velocity dispersion and this is probably related to the interaction with the companion. Since the galaxies are aligned and since the overall velocity gradient is monotonic, the whole system could eventually be considered as a unique galaxy with two big clumps. However, such a system would be very much extended, a property which is physically unlikely at these redshifts. The companion show a clear velocity shear and has been classified as well. It is also worth noticing that the minor companion in I-band is the most luminous in the K-band (from UKIDSS Deep Extragalactic Survey, Lawrence et al. 2007), thus likely the most massive one.

**VVDS220544103** This galaxy has a clear velocity gradient. The object is distorted in the I-band image as well as in  $\text{H}\alpha$ . This can be explained by the presence of two components (the morphology has been decomposed using this hypothesis). In that case, the Southern component may be well described by a rotating galaxy and the brightest blob in  $\text{H}\alpha$  (North) maybe a companion in a merging stage or a relic of merging. However, it cannot be ruled out that this is a single object with disturbed morphology and kinematics hence the flag B.

**VVDS220544394** The  $\text{H}\alpha$  map clearly shows the presence of a main component and a faintest one on the North. Their velocity fields seem decorrelated enough to claim that these are two separated objects on a pre-merging stage. The small component is also clearly detected in the I-band. The velocity field of the main component is perturbed but shows a velocity shear. Its velocity dispersion is around  $50 \text{ km s}^{-1}$ . The small component is slightly larger than the seeing and may be as well considered as having a velocity shear.

**VVDS220576226** The velocity field is perturbed on the North where the SNR is the lowest. The velocity dispersion map is regular. Two objects are observed within  $6''$  in the I-band image but are not detected in  $\text{H}\alpha$ .

**VVDS220578040** The I-band image shows an asymmetric galaxy with a more diffuse emission on the East. The  $\text{H}\alpha$  map shows two blobs. These can be interpreted either as two distinct galaxies or as two clumps in one single galaxy. The velocity field is perturbed and is not fully reproduced by the model. The velocity dispersion map is slightly perturbed. Since no strong kinematics perturbation is observed, this galaxy is classified as isolated (with a flag

C) and thus its kinematics is interpreted as sign of rotation.

**VVDS220584167** The I-band morphology is distorted and the  $H\alpha$  distribution is asymmetric. The kinematic position angle is however in very good agreement with the morphology. The velocity field shows some perturbations such as a slight asymmetry. This could be due to the position of the kinematic center that would differ from the morphological one. The velocity dispersion map is however peaked in the center, but the beam smearing may not account for the whole amplitude of the peak. Two objects are detected in I-band but not in  $H\alpha$  at less than  $6''$ .

**VVDS220596913** This galaxy is a chain galaxy in the I-band. It has been observed both with and without adaptive optics (cf. Contini et al. 2011). Several blobs are detected in  $H\alpha$ . They can be interpreted as several clumps in a single edge-on galaxy since the velocity field is monotonic. They can also be interpreted as several small galaxies in a merging stage. The continuum has been extracted from the SINFONI data around  $H\alpha$  and seems to be peaked in the center, between the  $H\alpha$  blobs, more in favor for an edge-on hypothesis. Since no strong kinematics perturbation is observed, and since a previous seeing-limited observation (Epinat et al. 2009) revealed that no extra emission is detected, this galaxy is classified as isolated with a flag B and thus its kinematics is interpreted as sign of rotation.

**VVDS910193711** This observation has been done using adaptive optics. The extent is larger than  $1''$ . The velocity field is perturbed. The interpretation of the perturbations may not be comparable with seeing-limited observations because the SNR is lower and the scale of the perturbations smaller. The velocity dispersion is large (around  $100 \text{ km s}^{-1}$ ). In the close neighborhood that would be observed using the seeing-limited strategy, several objects are detected in the I-band image.

**VVDS910279515** This galaxy has been observed using adaptive optics and is thus less deep than seeing-limited observations. This galaxy is unclassified since there are only a few pixels with a SNR larger than 3. In the I-band image there are several objects at less than  $5''$  that would have been observed using a seeing limited strategy.

**Table 1.** MASSIV galaxies “first epoch” sample and SINFONI observation setups

VVDS ID	R.A.	Dec.	z	Scale	Pixel scale	Band	Line	$t_{exp}$	Seeing	R	Period
(1)	[J2000]	[J2000]	(4)	[kpc/'']	['']	(7)	(8)	[minutes]	['']	(11)	(12)
020106882	02:25:21.819	−04:46:18.35	1.3991	8.43	0.125×0.25	H	H $\alpha$	80	0.49	2477	P82G
020116027	02:25:51.085	−04:45:06.08	1.5302	8.47	0.125×0.25	H	H $\alpha$	75	0.60	2609	P75A
020126402 <sup>1</sup>	02:25:11.658	−04:43:40.12	1.2332	8.33	0.050×0.10	J	[OIII]	60	—	—	P79B
020147106	02:26:45.362	−04:40:47.50	1.5195	8.47	0.125×0.25	H	H $\alpha$	120	0.65	2598	P75A
020149061	02:27:05.226	−04:40:29.21	1.2905	8.37	0.125×0.25	H	H $\alpha$	80	0.85	2362	P82G
020164388	02:26:50.942	−04:38:20.72	1.3547	8.41	0.125×0.25	H	H $\alpha$	80	0.83	2430	P82G
020167131	02:26:47.307	−04:37:55.36	1.2246	8.32	0.125×0.25	J	[OIII]	120	0.68	2295	P79B
020182331	02:26:44.242	−04:35:52.01	1.2290	8.32	0.125×0.25	H	H $\alpha$	180	0.74	2302	P78A
020193070	02:25:18.713	−04:34:19.77	1.0279	8.06	0.125×0.25	J	H $\alpha$	120	0.58	2094	P82G
020208482	02:25:16.739	−04:32:11.92	1.0375	8.08	0.125×0.25	J	H $\alpha$	120	0.58	2104	P82G
020214655	02:26:23.441	−04:31:22.78	1.0395	8.08	0.125×0.25	J	H $\alpha$	80	0.87	2101	P82G
020217890 <sup>1</sup>	02:26:27.162	−04:30:51.83	1.5129	8.46	0.125×0.25	H	H $\alpha$	120	—	—	P78A
020239133	02:26:43.006	−04:28:31.20	1.0194	8.04	0.125×0.25	J	H $\alpha$	80	0.79	2084	P82G
020240675	02:26:54.140	−04:28:17.64	1.3270	8.40	0.125×0.25	H	H $\alpha$	80	0.85	2402	P82G
020255799	02:26:45.859	−04:26:15.80	1.0351	8.07	0.125×0.25	J	H $\alpha$	80	0.76	2101	P82G
020261328	02:27:11.023	−04:25:31.57	1.5290	8.47	0.125×0.25	H	H $\alpha$	60	0.62	2609	P75A
020278667	02:25:58.203	−04:23:11.67	1.0516	8.10	0.125×0.25	J	H $\alpha$	120	0.65	2115	P82G
020283083	02:26:30.832	−04:22:35.82	1.2818	8.36	0.125×0.25	H	H $\alpha$	80	0.78	2353	P82G
020283830	02:26:28.926	−04:22:31.14	1.3949	8.43	0.125×0.25	H	H $\alpha$	120	0.77	2472	P82G
020294045	02:25:47.152	−04:21:07.41	1.0028	8.01	0.125×0.25	J	H $\alpha$	120	0.59	2067	P79B
020306817 <sup>1</sup>	02:25:50.316	−04:19:22.93	1.2225	8.32	0.125×0.25	J	[OIII]	120	—	—	P79B
020363717	02:26:23.709	−04:11:57.87	1.3339	8.40	0.125×0.25	H	H $\alpha$	80	0.64	2407	P82G
020370467	02:26:14.690	−04:11:05.44	1.3338	8.40	0.125×0.25	H	H $\alpha$	80	0.71	2407	P82G
020386743	02:27:13.989	−04:08:59.73	1.0487	8.09	0.125×0.25	J	H $\alpha$	120	0.73	2111	P79B
020461235	02:26:47.102	−04:23:55.70	1.0349	8.07	0.125×0.25	J	H $\alpha$	120	0.63	2101	P79B
020461893	02:27:12.252	−04:23:11.28	1.0486	8.09	0.125×0.25	J	H $\alpha$	80	0.60	2115	P82G
020465775	02:26:59.366	−04:19:00.08	1.3583	8.41	0.125×0.25	H	H $\alpha$	80	0.88	2434	P82G
140083410	13:57:50.595	+04:17:38.71	0.9435	7.89	0.125×0.25	J	H $\alpha$	80	0.69	2005	P81D
140096645	13:58:26.336	+04:19:47.75	0.9655	7.94	0.125×0.25	J	H $\alpha$	120	0.56	2024	P81D
140123568	13:55:57.628	+04:24:20.11	1.0012	8.01	0.125×0.25	J	H $\alpha$	120	0.76	2067	P79A
140137235	13:56:12.729	+04:26:31.74	1.0445	8.09	0.125×0.25	J	H $\alpha$	80	0.76	2111	P79A
140217425	13:57:56.405	+04:38:37.00	0.9792	7.97	0.125×0.25	J	H $\alpha$	100	0.95	2040	P81D
140258511	14:00:19.658	+04:44:45.86	1.2423	8.33	0.125×0.25	H	H $\alpha$	80	0.49	2315	P79A
140262766	13:59:55.518	+04:45:30.04	1.2836	8.37	0.125×0.25	H	H $\alpha$	120	0.51	2353	P79A
140545062	13:59:35.598	+05:30:31.11	1.0408	8.08	0.125×0.25	J	H $\alpha$	120	0.70	2104	P81D
220014252	22:17:45.677	+00:28:39.52	1.3105	8.38	0.125×0.25	H	H $\alpha$	120	0.70	2384	P75A
220015726	22:15:42.435	+00:29:03.58	1.2933	8.37	0.125×0.25	H	H $\alpha$	120	0.46	2384	P79B
220071601 <sup>1</sup>	22:18:01.569	+00:45:34.69	1.3538	8.41	0.050×0.10	H	H $\alpha$	80	—	—	P79B
220148046	22:14:37.904	+01:08:20.65	2.2442	8.24	0.050×0.10	H	[OIII]	80	0.27	2450	P81E
220376206	22:20:05.772	−00:08:21.74	1.2445	8.34	0.125×0.25	H	H $\alpha$	120	0.50	2315	P79B
220386469	22:19:56.603	−00:03:03.78	1.0226	8.05	0.050×0.10	J	H $\alpha$	40	0.23 <sup>2</sup>	2090	P79B
220397579	22:20:36.512	+00:01:46.85	1.0379	8.08	0.125×0.25	J	H $\alpha$	120	0.64	2101	P79B
220544103	22:15:25.689	+00:06:40.31	1.3973	8.43	0.125×0.25	H	H $\alpha$	120	0.76	2472	P75A
220544394	22:14:24.153	+00:06:46.67	1.0101	8.03	0.125×0.25	J	H $\alpha$	120	0.58	2073	P79B
220576226	22:16:11.417	+00:16:30.46	1.0217	8.05	0.125×0.25	J	H $\alpha$	120	0.58	2087	P79B
220578040	22:17:04.113	+00:16:56.80	1.0462	8.09	0.125×0.25	J	H $\alpha$	120	0.62	2111	P79B
220584167	22:15:22.917	+00:18:48.82	1.4655	8.45	0.125×0.25	H	H $\alpha$	120	0.75	2541	P75A
220596913	22:14:29.179	+00:22:18.93	1.2658	8.35	0.050×0.10	H	H $\alpha$	120	0.18	2340	P79B
910193711	02:25:46.285	−04:32:33.43	1.5564	8.47	0.050×0.10	H	H $\alpha$	80	0.27	2636	P82F
910279515	02:25:36.233	−04:21:16.13	1.4013	8.43	0.050×0.10	H	H $\alpha$	80	0.21	2477	P82F

The coordinates of the galaxies are given in column (2) and (3). The redshift (4) is determined from SINFONI data. The physical scale (5) is computed from the redshift. The SINFONI pixel scale is given in column (6). In column (7), the wavelength band used to observe the emission line (8) is given. Column (9) is the on-source exposure time. The seeing of SINFONI observations (10) is derived from observed PSF stars. Column (11) is the spectral resolution. The ESO observing period is given in column (12).

<sup>1</sup> These galaxies are those for which no line was detected in SINFONI data. The redshift is the one derived from VIMOS spectra, the line is the targeted one and both spectral and spatial resolution have not been measured.

<sup>2</sup> No PSF star was observed: the resolution is the mean resolution of AO observations.

**Table 2.** CFHT observations and morphological parameters from GALFIT modeling

VVDS ID	Survey	Pixel scale ["]	Seeing ["]	$PA$ [°]	$b/a$	$R_e$ [kpc]	$n$
(1)	(2)	(3)	(4)	(5)	(6)	(7)	(8)
020106882	LS	0.186	0.604	$294 \pm 4$	$0.62 \pm 0.03$	$3.51 \pm 0.14$	$0.77 \pm 0.16$
020116027	LS	0.186	0.604	$184 \pm 2$	$0.38 \pm 0.03$	$4.27 \pm 0.16$	$0.70 \pm 0.15$
020126402	LS	0.186	0.615	$15 \pm 8$	$0.56 \pm 0.10$	$2.12 \pm 0.31$	$0.59 \pm 0.58$
020147106	LS	0.186	0.615	$310 \pm 1$	$0.19 \pm 0.15$	$1.17 \pm 0.41$	$0.41 \pm 1.82$
020149061	LS	0.186	0.649	$201 \pm 369$	$0.93 \pm 0.83$	$1.09 \pm 0.69$	$0.11 \pm 6.68$
020164388	LS	0.186	0.618	$162 \pm 3$	$0.71 \pm 0.02$	$2.72 \pm 0.05$	$0.85 \pm 0.09$
020167131	LS	0.186	0.618	$272 \pm 3$	$0.60 \pm 0.03$	$2.60 \pm 0.09$	$1.64 \pm 0.26$
020167131s	LS	0.186	0.618	$57 \pm 1$	$0.37 \pm 0.02$	$4.11 \pm 0.08$	$0.31 \pm 0.09$
020182331	LS	0.186	0.618	$268 \pm 4$	$0.49 \pm 0.04$	$4.19 \pm 0.17$	$0.63 \pm 0.21$
020193070	LS	0.186	0.615	$215 \pm 2$	$0.33 \pm 0.03$	$3.49 \pm 0.09$	$0.47 \pm 0.13$
020208482	LS	0.186	0.600	$355 \pm 7$	$0.70 \pm 0.05$	$3.67 \pm 0.20$	$0.82 \pm 0.21$
020214655	LS	0.186	0.604	$32 \pm 4$	$0.41 \pm 0.06$	$1.47 \pm 0.08$	$1.97 \pm 0.53$
020217890	LS	0.186	0.604	$171 \pm 2$	$0.21 \pm 0.04$	$3.57 \pm 0.14$	$1.13 \pm 0.22$
020239133	LS	0.186	0.608	$123 \pm 2$	$0.39 \pm 0.03$	$3.14 \pm 0.09$	$0.25 \pm 0.13$
020240675	LS	0.186	0.619	$190 \pm 13$	$0.62 \pm 0.13$	$1.09 \pm 0.16$	$2.03 \pm 1.19$
020255799	LS	0.186	0.607	$164 \pm 12$	$0.80 \pm 0.08$	$1.89 \pm 0.26$	$0.24 \pm 0.44$
020261328	LS	0.186	0.634	$171 \pm 8$	$0.51 \pm 0.11$	$1.83 \pm 0.27$	$0.64 \pm 0.53$
020278667	LS	0.186	0.596	$140 \pm 12$	$0.74 \pm 0.09$	$2.82 \pm 1.66$	$9.60 \pm 5.68$
020283083	LS	0.186	0.596	$301 \pm 3$	$0.38 \pm 0.05$	$4.29 \pm 0.20$	$0.46 \pm 0.18$
020283830	LS	0.186	0.596	$142 \pm 1$	$0.35 \pm 0.01$	$6.82 \pm 0.16$	$0.09 \pm 0.06$
020294045	LS	0.186	0.606	$1 \pm 3$	$0.61 \pm 0.03$	$2.89 \pm 0.10$	$1.00 \pm 0.17$
020306817	LS	0.186	0.606	$86 \pm 2$	$0.54 \pm 0.02$	$4.22 \pm 0.09$	$0.27 \pm 0.08$
020363717	LS	0.186	0.626	$154 \pm 6$	$0.55 \pm 0.08$	$0.72 \pm 0.09$	$3.59 \pm 1.01$
020370467	LS	0.186	0.626	$50 \pm 24$	$0.78 \pm 0.18$	$1.31 \pm 0.25$	$0.54 \pm 0.97$
020386743	LS	0.186	0.639	$203 \pm 8$	$0.64 \pm 0.07$	$2.68 \pm 0.21$	$1.15 \pm 0.42$
020461235	LS	0.186	0.597	$332 \pm 3$	$0.57 \pm 0.02$	$3.96 \pm 0.12$	$0.47 \pm 0.11$
020461893	LS	0.186	0.634	$283 \pm 3$	$0.46 \pm 0.04$	$2.66 \pm 0.11$	$1.04 \pm 0.23$
020465775	LS	0.186	0.623	$146 \pm 3$	$0.51 \pm 0.03$	$4.04 \pm 0.16$	$0.09 \pm 0.17$
140083410	12K	0.204	0.958	$311 \pm 10$	$0.67 \pm 0.09$	$1.93 \pm 0.19$	$1.90 \pm 0.82$
140096645	12K	0.204	0.747	$217 \pm 114$	$0.93 \pm 0.28$	$1.80 \pm 0.40$	$0.85 \pm 1.26$
140123568	12K	0.204	0.968	$227 \pm 229$	$0.80 \pm 1.14$	$1.39 \pm 0.98$	$0.08 \pm 32.82$
140137235	12K	0.204	0.920	$116 \pm 24$	$0.47 \pm 0.31$	$5.45 \pm 2.03$	$0.88 \pm 1.73$
140217425	12K	0.204	0.713	$260 \pm 1$	$0.25 \pm 0.01$	$8.96 \pm 0.13$	$0.33 \pm 0.04$
140258511	12K	0.204	0.768	$265 \pm 42$	$0.54 \pm 0.51$	$2.62 \pm 2.11$	$0.40 \pm 3.22$
140262766	12K	0.204	0.613	$142 \pm 28$	$0.65 \pm 0.26$	$2.07 \pm 0.70$	$0.63 \pm 1.34$
140545062	12K	0.204	0.724	$216 \pm 41$	$0.46 \pm 0.35$	$2.89 \pm 6.86$	$0.06 \pm 4.03$
220014252	LS	0.186	0.687	$136 \pm 2$	$0.22 \pm 0.06$	$3.32 \pm 0.12$	$0.94 \pm 0.23$
220015726	LS	0.186	0.686	$193 \pm 12$	$0.78 \pm 0.07$	$2.76 \pm 0.25$	$0.26 \pm 0.35$
220071601	LS	0.186	0.665	$74 \pm 1$	$0.31 \pm 0.01$	$8.13 \pm 0.13$	$0.21 \pm 0.04$
220148046	LS	0.186	0.800	$236 \pm 10$	$0.10 \pm 0.87$	$1.98 \pm 0.38$	$2.10 \pm 2.36$
220376206	LS	0.186	0.749	$235 \pm 1$	$0.46 \pm 0.01$	$5.29 \pm 0.08$	$0.21 \pm 0.05$
220386469	LS	0.186	0.725	$168 \pm 7$	$0.70 \pm 0.05$	$2.90 \pm 0.13$	$0.73 \pm 0.26$
220397579	LS	0.186	0.707	$331 \pm 5$	$0.43 \pm 0.06$	$3.02 \pm 0.32$	$0.21 \pm 0.37$
220397579s	LS	0.186	0.707	$332 \pm 2$	$0.14 \pm 0.03$	$9.77 \pm 3.29$	$3.77 \pm 1.49$
220544103	LS	0.186	0.686	$208 \pm 55$	$0.08 \pm 0.16$	$5.61 \pm 19.89$	$0.02 \pm 0.91$
220544103s	LS	0.186	0.686	$161 \pm 5$	$0.26 \pm 0.06$	$5.47 \pm 0.44$	$1.67 \pm 0.77$
220544394	LS	0.186	0.624	$234 \pm 7$	$0.70 \pm 0.04$	$3.40 \pm 0.15$	$0.48 \pm 0.13$
220544394s	LS	0.186	0.624	$233 \pm 10$	$0.30 \pm 0.17$	$3.69 \pm 0.70$	$1.18 \pm 1.02$
220576226	LS	0.186	0.675	$237 \pm 15$	$0.85 \pm 0.06$	$2.16 \pm 0.12$	$1.58 \pm 0.36$
220578040	LS	0.186	0.658	$112 \pm 14$	$0.89 \pm 0.04$	$3.81 \pm 0.12$	$0.42 \pm 0.10$
220584167	LS	0.186	0.684	$193 \pm 2$	$0.52 \pm 0.01$	$7.17 \pm 0.19$	$0.14 \pm 0.06$
220596913	LS	0.186	0.623	$255 \pm 1$	$0.18 \pm 0.02$	$9.49 \pm 11.54$	$0.04 \pm 0.12$
910193711	LS	0.186	0.597	$9 \pm 3$	$0.50 \pm 0.03$	$2.27 \pm 0.06$	$0.50 \pm 0.17$
910279515	LS	0.186	0.602	$131 \pm 3$	$0.61 \pm 0.02$	$4.44 \pm 0.11$	$0.28 \pm 0.08$

In column (2), “LS” refers to the CFHT Legacy Survey (<http://www.cfht.hawaii.edu/Science/CFHLS/>) whereas “12K” refers to the CFH12K/CFHT survey (McCracken et al. 2003). The pixel scale of the CFHT image and the seeing determined from close stars are respectively given in column (3) and (4). The parameters of the model are the position angle of the major axis (5), the axis ratio (6), the effective radius (7), the Sersic index (7) and the magnitude (not given here due to a zero point magnitude mismatch between the two CFHT surveys).

The suffix “s” refers to secondary objects which have been detected both in H $\alpha$  and in the I-band image. The companions parameters are only given when they are resolved.

**Table 3.** Physical parameters from kinematic modeling

VVDS ID	$i$	$PA_k$	$r_t$	$V_t$	$V_t/r_t$	$\text{Res}_V$	$\chi^2$	$V_{max}$	$\sigma$	$R_{last}$
(1)	[°]	[°]	[kpc]	[km s <sup>-1</sup> ]	[km s <sup>-1</sup> kpc <sup>-1</sup> ]	[km s <sup>-1</sup> ]	(8)	[km s <sup>-1</sup> ]	[km s <sup>-1</sup> ]	[kpc]
(1)	(2)	(3)	(4)	(5)	(6)	(7)	(8)	(9)	(10)	(11)
020106882	52 ± 3	317 ± 1	1.1 ± 0.1	133 ± 3	126	12	1.6	133 ± 25	41 ± 31	5.1
020116027	68 ± 4	207 ± 6	4.3 ± 3.0	27 ± 6	6	10	3.7	27 ± 10	47 ± 15	6.5
020147106	60 ± 24	317 ± 3	1.6 ± 4.6	26 ± 3	16	6	1.9	26 ± 51	81 ± 10	7.8
020149061	60 ± 24	235 ± 3	42.0	976	23	15	1.9	112 ± 216	73 ± 20	4.8
020164388	45 ± 4	97 ± 4	7.2 ± 4.9	79 ± 44	11	8	0.9	79 ± 19	52 ± 19	8.2
020167131	53 ± 4	185 ± 10	1.0 ± 0.1	127 ± 43	123	13	0.9	127 ± 29	26 ± 37	1.8
020182331	61 ± 2	234 ± 4	27.0	647	24	11	0.9	132 ± 26	67 ± 29	5.5
020193070	71 ± 4	184 ± 2	108.7	3217	30	15	1.8	117 ± 23	33 ± 27	3.9
020208482	46 ± 3	336 ± 10	1.0 ± 0.1	158 ± 38	157	11	0.6	158 ± 31	7 ± 11	1.4
020214655	66 ± 11	341 ± 4	1.0 ± 0.1	52 ± 4	51	8	1.1	52 ± 14	63 ± 25	5.7
020239133	67 ± 4	109 ± 6	24.6	766	31	13	0.9	149 ± 33	75 ± 35	4.8
020240675	60 ± 24	183 ± 12	8.9	116	13	13	1.5	50 ± 97	33 ± 17	3.8
020255799	37 ± 15	89 ± 76	1.0 ± 0.1	14 ± 16	14	10	0.6	14 ± 26	76 ± 23	4.0
020261328	59 ± 11	179 ± 2	6.2	154	25	10	1.6	127 ± 35	54 ± 19	5.1
020278667	42 ± 20	175 ± 6	3.7	224	60	16	1.5	77 ± 189	52 ± 37	1.3
020283083	68 ± 2	359 ± 4	1.0 ± 0.1	59 ± 5	57	11	1.4	59 ± 12	39 ± 23	5.6
020283830	70 ± 1	156 ± 2	1.9 ± 3.4	186 ± 5	96	21	4.7	186 ± 30	17 ± 24	7.9
020294045	52 ± 5	3 ± 1	31.1	1332	43	33	12.4	234 ± 51	60 ± 45	5.5
020363717	60 ± 24	106 ± 6	16.4	123	8	9	1.3	45 ± 86	91 ± 14	6.0
020370467	39 ± 14	19 ± 11	1.0 ± 0.1	51 ± 10	49	18	1.2	51 ± 64	86 ± 35	5.5
020386743	50 ± 4	136 ± 3	37.0	286	8	9	2.5	42 ± 10	53 ± 18	5.4
020461235	55 ± 1	351 ± 2	1.2 ± 7.7	82 ± 4	67	11	1.8	82 ± 16	24 ± 22	5.4
020461893	63 ± 4	279 ± 4	1.2 ± 9.1	58 ± 6	46	8	1.1	58 ± 13	67 ± 22	6.5
020465775	59 ± 2	178 ± 5	1.1 ± 0.1	68 ± 7	65	13	1.5	68 ± 15	84 ± 30	4.9
140083410	48 ± 16	39 ± 6	1.0 ± 0.1	30 ± 4	30	10	2.3	30 ± 33	66 ± 21	5.3
140096645	22 ± 15	197 ± 1	1.1 ± 1.1	295 ± 12	258	12	6.1	295 ± 709	77 ± 27	4.5
140123568	60 ± 24	184 ± 14	1.0	108	108	6	0.7	50 ± 99	73 ± 24	0.5
140137235	62 ± 1	123 ± 16	2.2	200	91	4	0.6	62 ± 11	17 ± 27	0.7
140217425	76 ± 2	258 ± 1	16.1	499	31	29	20.7	320 ± 46 <sup>1</sup>	45 ± 33	14.5
140258511	57 ± 3	213 ± 1	1.0 ± 0.1	124 ± 4	119	19	5.2	124 ± 26	25 ± 29	5.2
140262766	60 ± 24	175 ± 2	18.1	524	29	9	1.2	119 ± 231	39 ± 16	4.1
140545062	63 ± 5	229 ± 1	13.9	378	27	13	3.6	204 ± 46	67 ± 29	7.5
220014252	77 ± 2	141 ± 1	1.0 ± 0.1	129 ± 1	123	15	4.5	129 ± 27	90 ± 28	10.3
220015726	39 ± 15	186 ± 1	1.5 ± 0.4	231 ± 4	155	10	3.1	231 ± 356	62 ± 22	3.7
220148046	60 ± 24	261 ± 15	1.3	61	49	10	2.9	42 ± 83	46 ± 21	0.9
220376206	63 ± 2	225 ± 1	8.3 ± 0.2	201 ± 4	24	15	4.8	201 ± 27	73 ± 26	10.0
220386469	46 ± 7	151 ± 10	63.0	973	15	16	2.0	40 ± 11	43 ± 25	2.6
220397579	65 ± 6	1 ± 9	35.9	32	1	9	7.0	9 ± 10	59 ± 17	10.2
220397579s	80 ± 5	344 ± 2	3.8 ± 1.2	222 ± 9	59	17	2.6	222 ± 15	27 ± 37	6.2
220544103	80 ± 4	198 ± 1	1.1 ± 0.1	137 ± 2	130	12	4.4	137 ± 24	71 ± 19	7.6
220544394	46 ± 2	180 ± 2	2.0 ± 1.5	55 ± 4	27	5	0.8	55 ± 11	49 ± 17	5.0
220544394s	73 ± 5	198 ± 4	1.0 ± 0.1	94 ± 8	94	16	1.7	94 ± 18	32 ± 28	4.5
220576226	32 ± 6	283 ± 3	1.0 ± 0.1	30 ± 1	30	4	1.1	30 ± 12	51 ± 14	6.1
220578040	27 ± 9	103 ± 2	18.5	654	35	16	5.1	247 ± 205	50 ± 23	7.0
220584167	59 ± 1	178 ± 1	9.7 ± 0.2	234 ± 2	24	15	7.9	234 ± 35	49 ± 21	13.1
220596913	80 ± 2	247 ± 1	0.9 ± 0.1	141 ± 2	153	22	4.3	141 ± 10	38 ± 28	9.3
910193711	60 ± 8	39 ± 4	3.5 ± 0.7	63 ± 8	18	17	2.6	63 ± 12	80 ± 37	4.1
910279515	52 ± 4	108 ± 7	3.8	265	70	34	5.3	186 ± 14	47 ± 40	2.7

The parameters of the kinematics modeling are the inclination (2), the position angle of the major axis (3), the turnover radius (4) and velocity (5). The inner slope is given in column (6). The mean residual of the velocity field is given in column (7) and the fit chi square in column (8). The maximum rotational velocity (9) and the mean velocity dispersion corrected from beam smearing (10) are computed after from the results of the fit. The extent of the velocity field (11) is derived using a SNR threshold of 3.

The suffix “s” refers to secondary objects which have been detected in H $\alpha$  and large enough to perform kinematics modeling. No error is given for  $r_t$  and  $V_t$  when the plateau is not reached (see Section 3.2.3).

<sup>1</sup>  $V_{max}$  is not coming from the model but from a detailed analysis (see Appendix A).

**Table 4.** Kinematics and close environment classification of MASSIV “first epoch” sample galaxies

VVDS ID	SNR	$\frac{R_{last}}{Seeing}$	$\Delta PA [^\circ]$	$\frac{Res}{V_{shear}/2}$	$V_{max}/\sigma$	Shear	Rotator	Isolated	Isolation flag
(1)	(2)	(3)	(4)	(5)	(6)	(7)	(8)	(9)	(10)
020106882	7.6	1.2	$23 \pm 4$	0.07	3.2	High	Yes	Yes	B
020116027	8.2	1.3	$23 \pm 6$	0.27	0.6	Low	No	No	A
020126402	< 3	—	—	—	—	—	—	—	—
020147106	12.2	1.4	$7 \pm 3$	0.18	0.3	Low	Yes	Yes	B
020149061	6.2	0.7	$34 \pm 90$	0.17	1.5	Low	Yes	Yes	B
020164388	11.0	1.2	$65 \pm 5$	0.11	1.5	Low	No	Yes	B
020167131	3.7	0.3	$87 \pm 11$	0.22	5.0	Low	No	No	A
020182331	6.1	0.9	$34 \pm 6$	0.09	2.0	High	No	Yes	B
020193070	4.9	0.8	$31 \pm 3$	0.10	3.6	High	No	Yes	B
020208482	4.1	0.3	$20 \pm 12$	0.18	22.9	Low	Yes	Yes	B
020214655	7.5	0.8	$51 \pm 5$	0.17	0.8	Low	No	Yes	B
020217890	< 3	—	—	—	—	—	—	—	—
020239133	5.3	0.8	$14 \pm 6$	0.11	2.0	High	Yes	Yes	B
020240675	5.5	0.5	$7 \pm 18$	0.40	1.5	Low	No	Yes	B
020255799	4.5	0.6	$75 \pm 77$	1.04	0.2	Low	No	Yes	B
020261328	7.8	1.0	$8 \pm 8$	0.07	2.4	High	Yes	Yes	B
020278667	4.1	0.2	$35 \pm 14$	0.34	1.5	Low	No	Yes	C
020283083	7.0	0.9	$58 \pm 5$	0.18	1.5	Low	No	No	B
020283830	4.8	1.2	$14 \pm 2$	0.08	11.3	High	Yes	No	B
020294045 <sup>1</sup>	7.0	1.2	$2 \pm 4$	0.12	3.9	Low	No	No	B
020306817	< 3	—	—	—	—	—	—	—	—
020363717	11.4	1.1	$49 \pm 8$	0.19	0.5	Low	No	Yes	B
020370467	5.5	0.9	$31 \pm 27$	0.45	0.6	Low	No	Yes	B
020386743	8.8	0.9	$67 \pm 8$	0.26	0.8	Low	No	No	A
020461235	5.8	1.1	$19 \pm 4$	0.10	3.5	High	Yes	No	B
020461893	7.0	1.3	$4 \pm 5$	0.10	0.9	Low	Yes	Yes	B
020465775	6.8	0.7	$31 \pm 5$	0.24	0.8	Low	No	No	B
140083410	6.0	1.0	$88 \pm 12$	0.35	0.4	Low	No	Yes	A
140096645	10.3	1.0	$20 \pm 90$	0.07	3.9	High	Yes	No	B
140123568	3.5	0.1	$43 \pm 90$	0.44	0.7	Low	No	Yes	B
140137235	3.2	0.1	$8 \pm 29$	0.11	3.5	Low	Yes	Yes	B
140217425	6.8	1.9	$2 \pm 1$	0.04	7.1	High	Yes	Yes	B
140258511	8.1	1.3	$52 \pm 42$	0.12	5.1	High	Yes	Yes	A
140262766	6.5	1.0	$32 \pm 28$	0.07	3.1	High	Yes	Yes	B
140545062	8.5	1.3	$14 \pm 41$	0.06	3.1	High	Yes	Yes	B
220014252	11.0	1.7	$5 \pm 2$	0.08	1.4	High	Yes	Yes	B
220015726	10.4	1.0	$8 \pm 12$	0.04	3.7	High	Yes	Yes	B
220071601	< 3	—	—	—	—	—	—	—	—
220148046	4.0	0.4	$25 \pm 18$	0.39	0.9	Low	No	Yes	C
220376206	12.6	2.4	$10 \pm 1$	0.05	2.8	High	Yes	No	B
220386469	4.5	1.1	$17 \pm 12$	0.42	0.9	Low	No	Yes	B
220397579	15.7	2.0	$31 \pm 10$	0.68	0.2	Low	No	No	A
220397579s	5.4	1.2	$11 \pm 3$	0.06	8.3	High	Yes	No	A
220544103	10.4	1.2	$11 \pm 55$	0.07	1.9	High	Yes	No	B
220544394	10.5	1.1	$54 \pm 7$	0.08	1.1	Low	No	No	A
220576226	11.6	1.3	$45 \pm 15$	0.15	0.6	Low	No	Yes	B
220578040	5.9	1.4	$10 \pm 14$	0.08	4.9	High	Yes	Yes	C
220584167	13.8	2.1	$15 \pm 2$	0.04	4.8	High	Yes	Yes	B
220596913	5.7	6.2	$8 \pm 1$	0.09	3.7	High	Yes	Yes	B
910193711	6.0	1.8	$30 \pm 4$	0.22	0.8	Low	No	Yes	C
910279515	3.5	1.5	$23 \pm 8$	0.11	3.9	High	Yes	Yes	C

Column (2) gives the average SNR of the SNR map. The size of the galaxy with respect to the seeing is given in column (3). The criteria used to determine if galaxies are in rotation or not (8) are the mismatch between morphological and kinematic position angles (4) and the residuals normalized by the velocity shear (5). The ratio of the rotation velocity over the local velocity dispersion is given in column (6). Galaxies are classified according the observed velocity shear in column (7): galaxies with  $V_{shear} < 100 \text{ km s}^{-1}$  or  $V_{shear} < 100 \text{ km s}^{-1}$  are respectively classified as low and high shear). The close environment classification and its associated quality flag are given in (9) and (10).

The suffix “s” refers to secondary objects which have been detected both in H $\alpha$  and in the I-band image.

<sup>1</sup> This galaxy is classified as non-rotating even if it fulfill the criteria because the kinematics seem to indicate that this system is composed of two close companions (cf. Appendix A).



**Table 5.** Physical properties of MASSIV sub-classes

Class	N	$M_{star}$ [ $10^{10} M_{\odot}$ ]			$SFR$ [ $M_{\odot} \text{ yr}^{-1}$ ]			$R_e$ [kpc]			$\sigma$ [ $\text{km s}^{-1}$ ]		
		Med	Mean	Dev	Med	Mean	Dev	Med	Mean	Dev	Med	Mean	Dev
Rotating	19	3.9	4.0	3.7	46	60	44	3.1	3.8	2.4	62	58	19
Non-Rotating	16	1.2	1.6	1.2	30	39	29	2.7	2.7	1.2	60	61	17
Detected but unclassified	10	1.5	2.3	2.1	24	34	30	2.3	2.3	1.0	43	39	24
Isolated	28	1.4	3.0	3.4	37	47	41	2.7	3.1	2.2	62	56	22
Interacting	13	1.7	2.1	1.4	30	43	32	4.0	3.9	1.4	53	52	21
Rotating + Isolated	14	3.9	4.1	4.3	58	63	49	2.9	3.8	2.7	62	57	19
Rotating + Interacting	4	4.6	3.6	1.4	64	55	33	5.3	4.2	1.7	73	61	25
Non-Rotating + Isolated	8	1.4	2.0	1.7	42	37	22	1.9	2.0	1.1	66	64	19
Non-Rotating + Interacting	7	1.2	1.3	0.5	26	35	33	3.4	3.5	0.7	53	56	15

N is the number of galaxies in each sub-class; Med: median value; Mean: average; Dev: standard deviation. Only the main objects are considered.

## Appendix B: Kinematic maps

This Appendix shows the kinematic maps for all the detected galaxies. For galaxies with detected companions, there are several sets of maps: one for the whole system (with no kinematics modeling) and one for each modeled component.

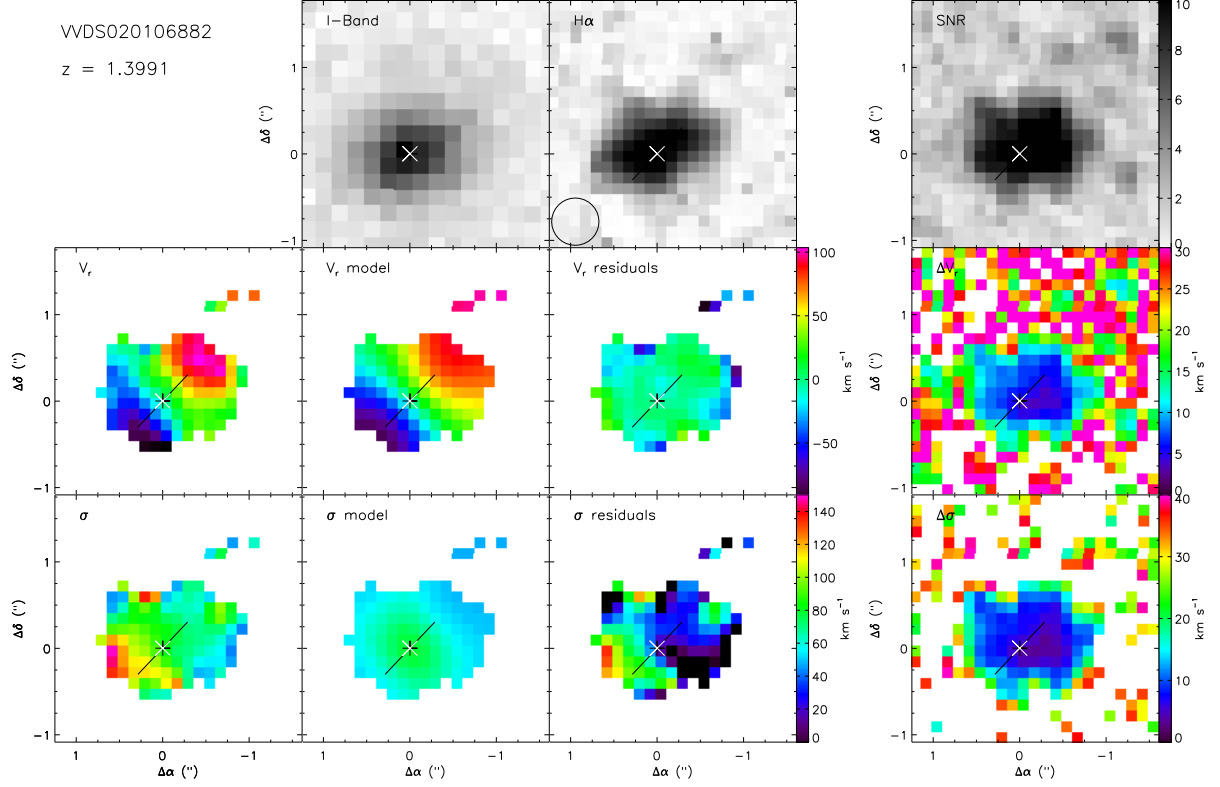


**Fig. B.1.** Maps for VVDS020106882. From left to right: (top) the I-band CFHT image (arbitrary scale), the  $H\alpha$  flux map (arbitrary scale) and the SNR map, (middle) the observed velocity field, the rotating disk modeled velocity field, the residual velocity field, the uncertainty map on the velocity field, (bottom) the observed uncorrected velocity dispersion, the velocity dispersion map deduced from the velocity field model (beam smearing effect and spectral PSF), the beam smearing corrected velocity dispersion map and the uncertainty on the velocity dispersion. The redshift is indicated on the top-left. On each map, North is up and East is left. The center used for kinematics modeling is indicated as a double black and white cross, the position angle is indicated by the black line. This line ends at the effective radius. The seeing FWHM is indicated on the  $H\alpha$  map as a circle.

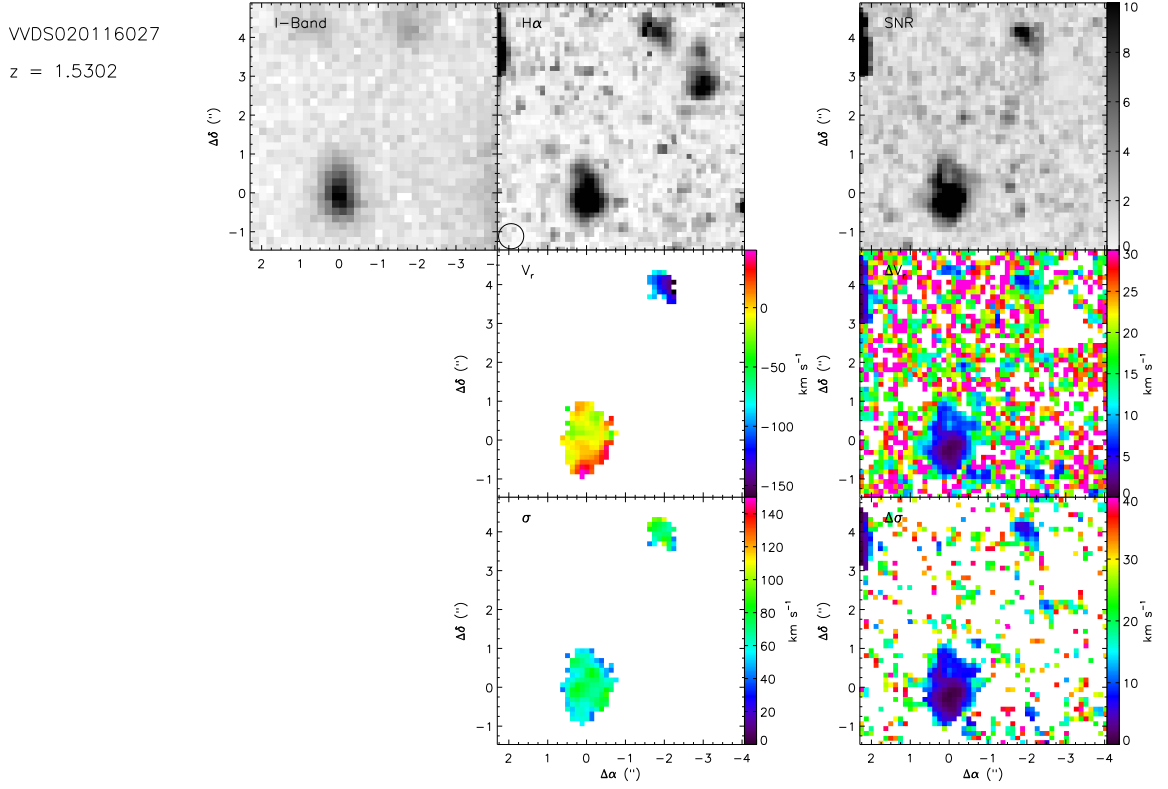


**Fig. B.2.** Maps for VVDS020116027 system. From left to right: (top) the I-band CFHT image (arbitrary scale), the H $\alpha$  flux map (arbitrary scale) and the SNR map, (middle) the observed velocity field, the uncertainty map on the velocity field, (bottom) the observed uncorrected velocity dispersion and the uncertainty on the velocity dispersion. The redshift is indicated on the top-left. On each map, North is up and East is left. The seeing FWHM is indicated on the H $\alpha$  map as a circle.

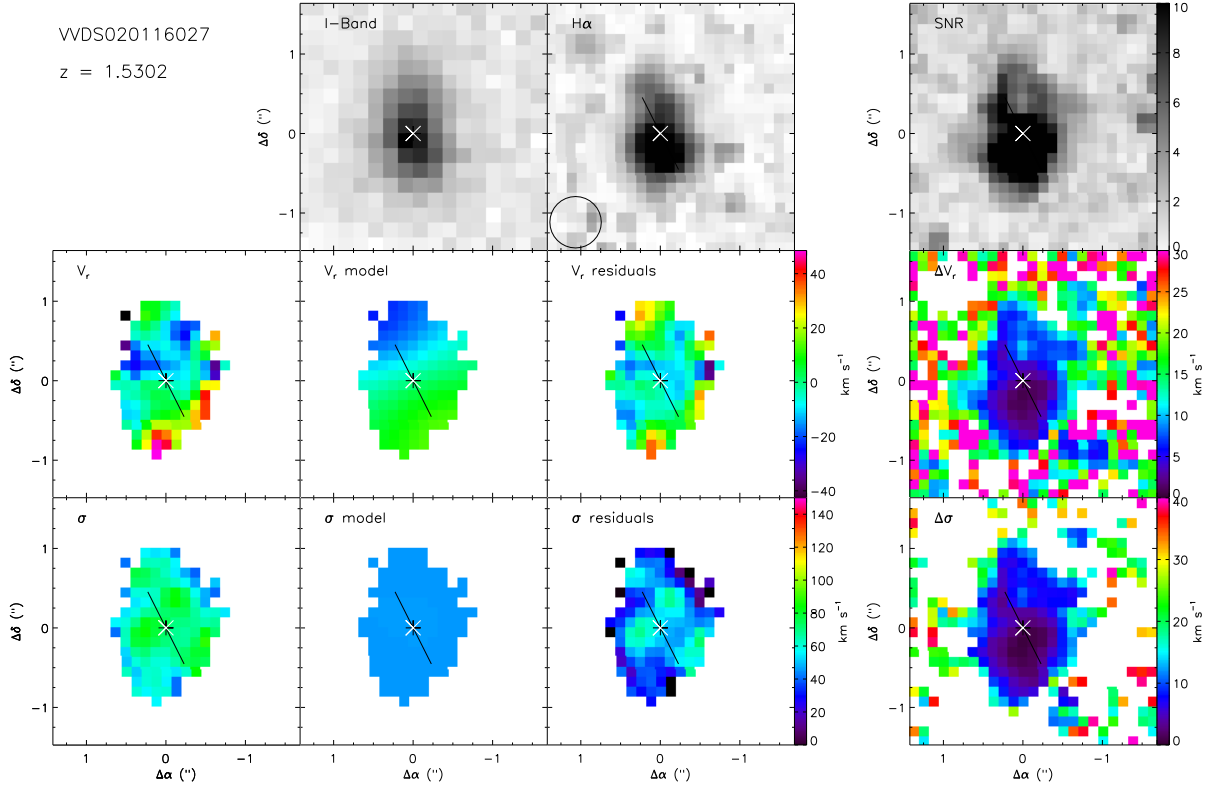


**Fig. B.3.** Maps for VVDS020116027. Same caption as Figure B.1.

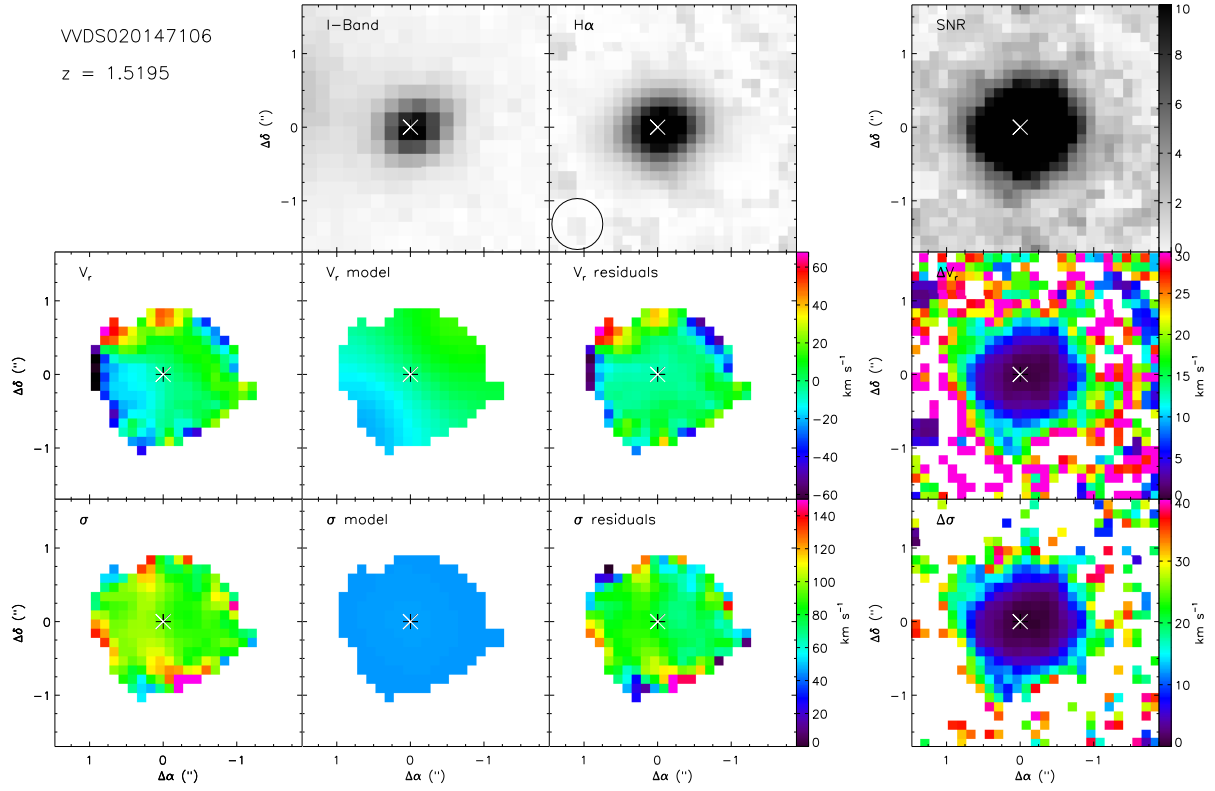


**Fig. B.4.** Maps for VVDS020147106. Same caption as Figure B.1.

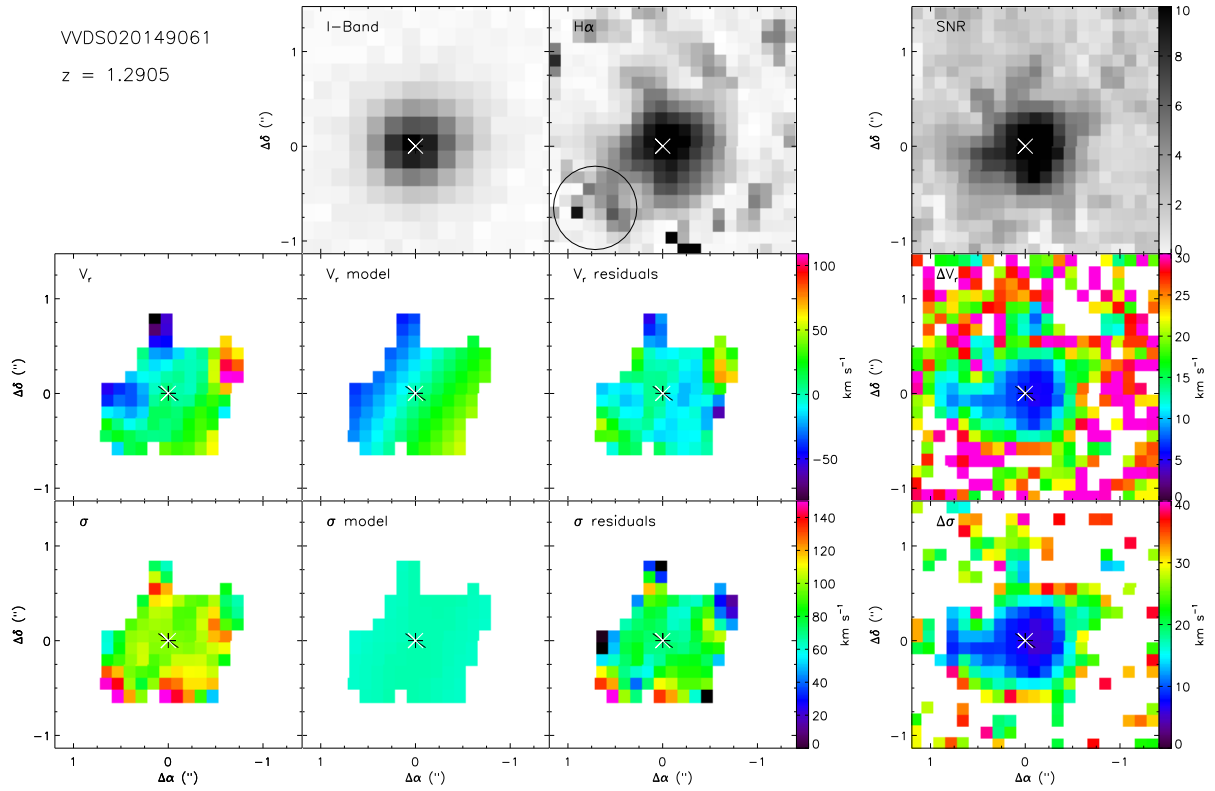


**Fig. B.5.** Maps for VVDS020149061. Same caption as Figure B.1.

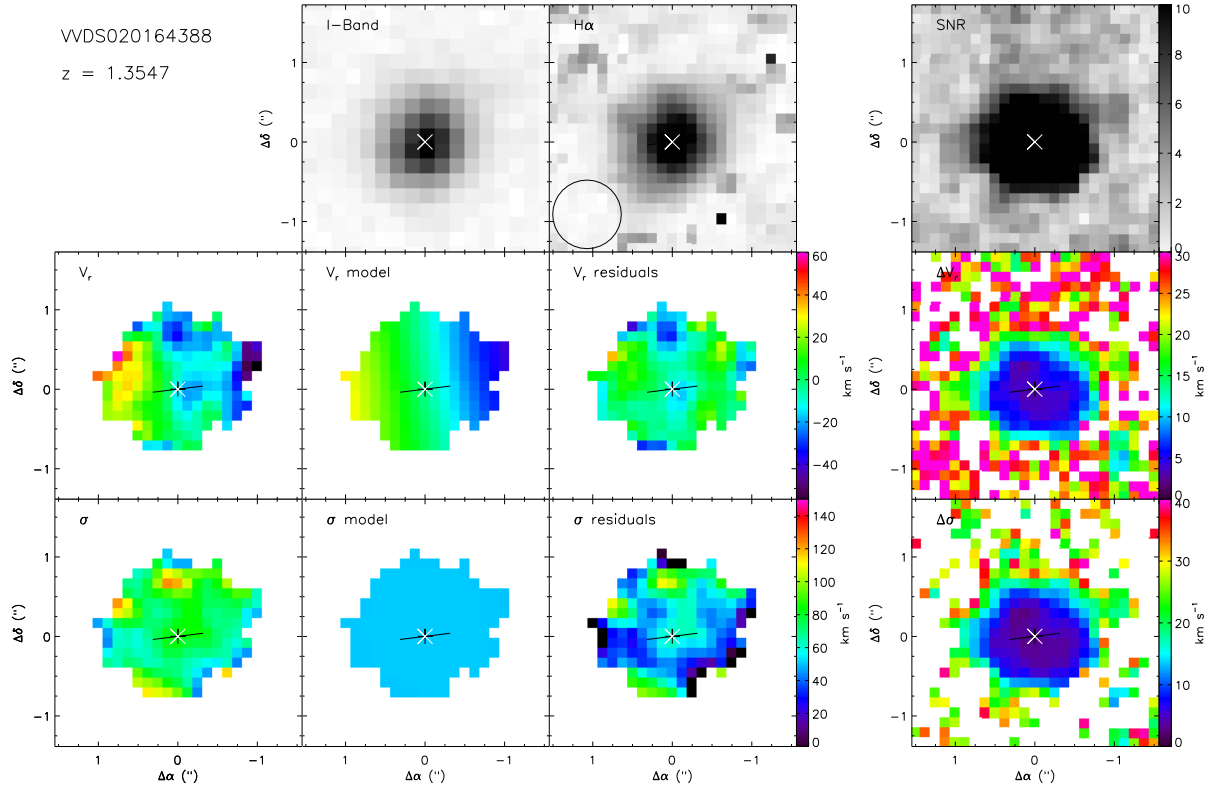


**Fig. B.6.** Maps for VVDS020164388. Same caption as Figure B.1.

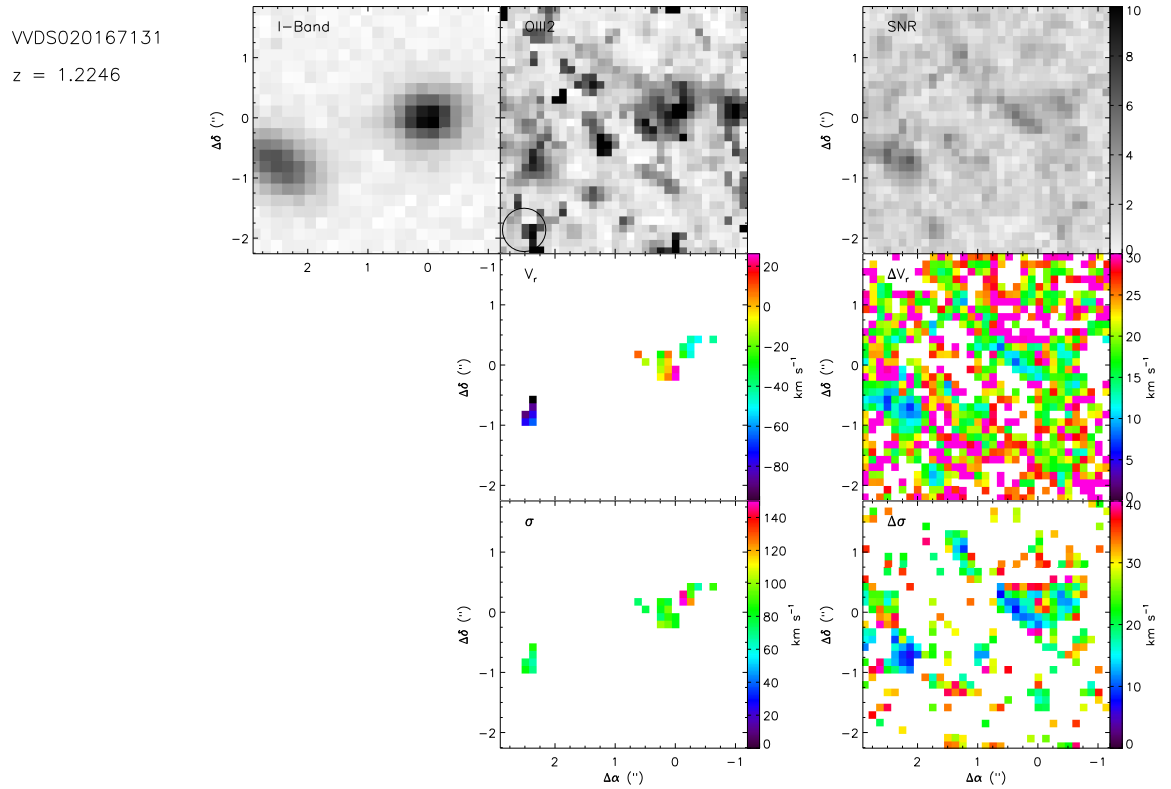


**Fig. B.7.** Maps for VVDS020167131 system. Same caption as Figure B.2.

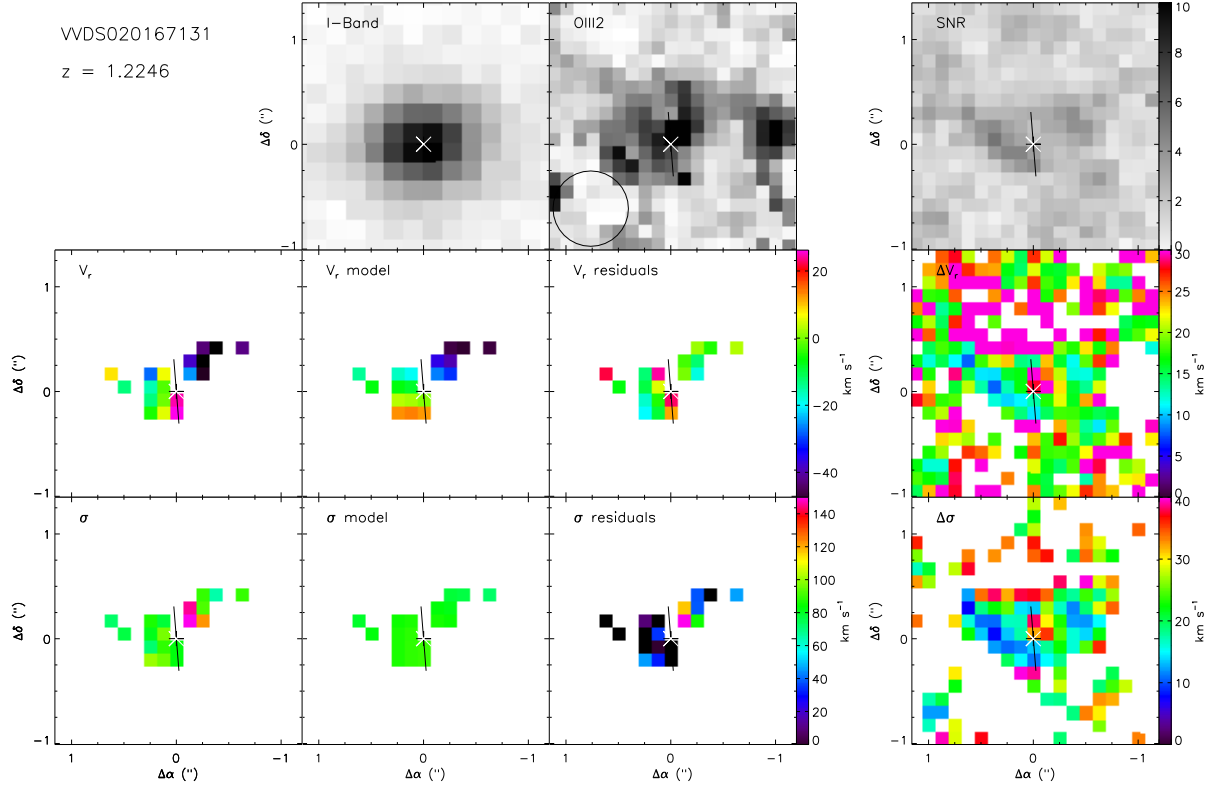


**Fig. B.8.** Maps for VVDS020167131. Same caption as Figure B.1.

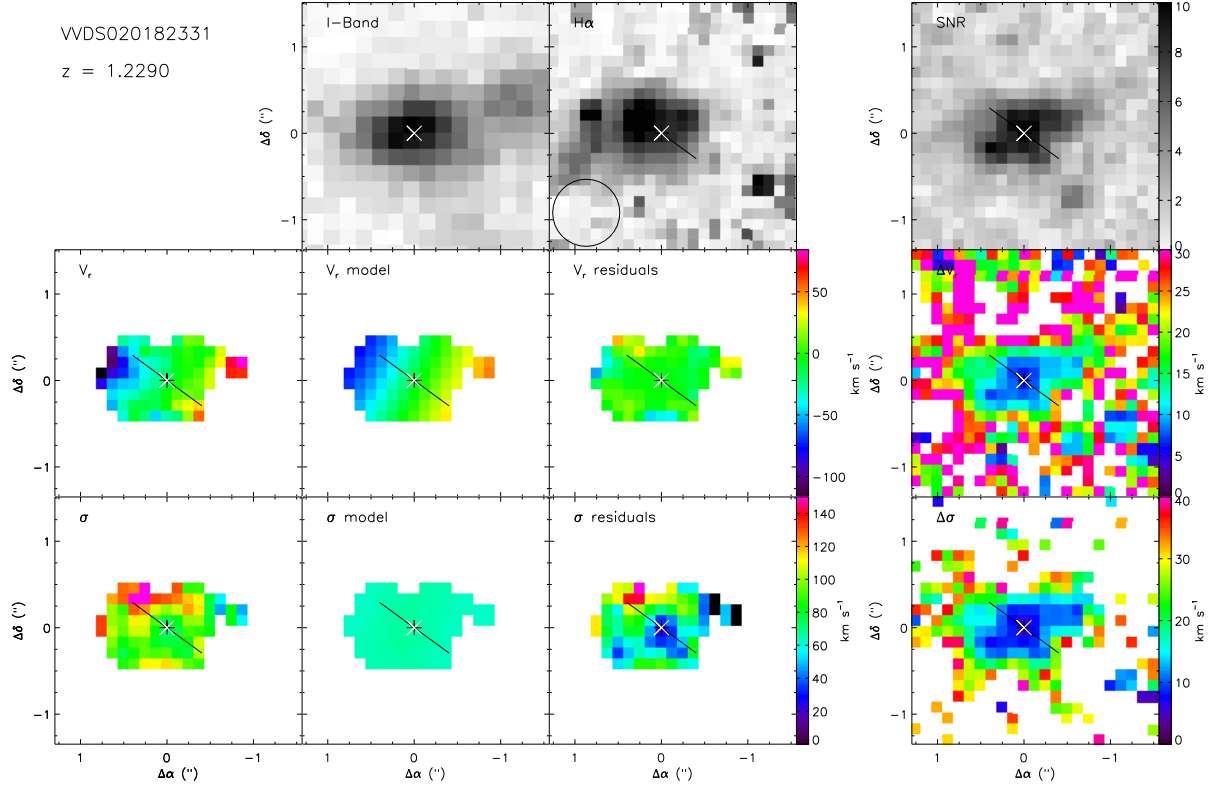


**Fig. B.9.** Maps for VVDS020182331. Same caption as Figure B.1.

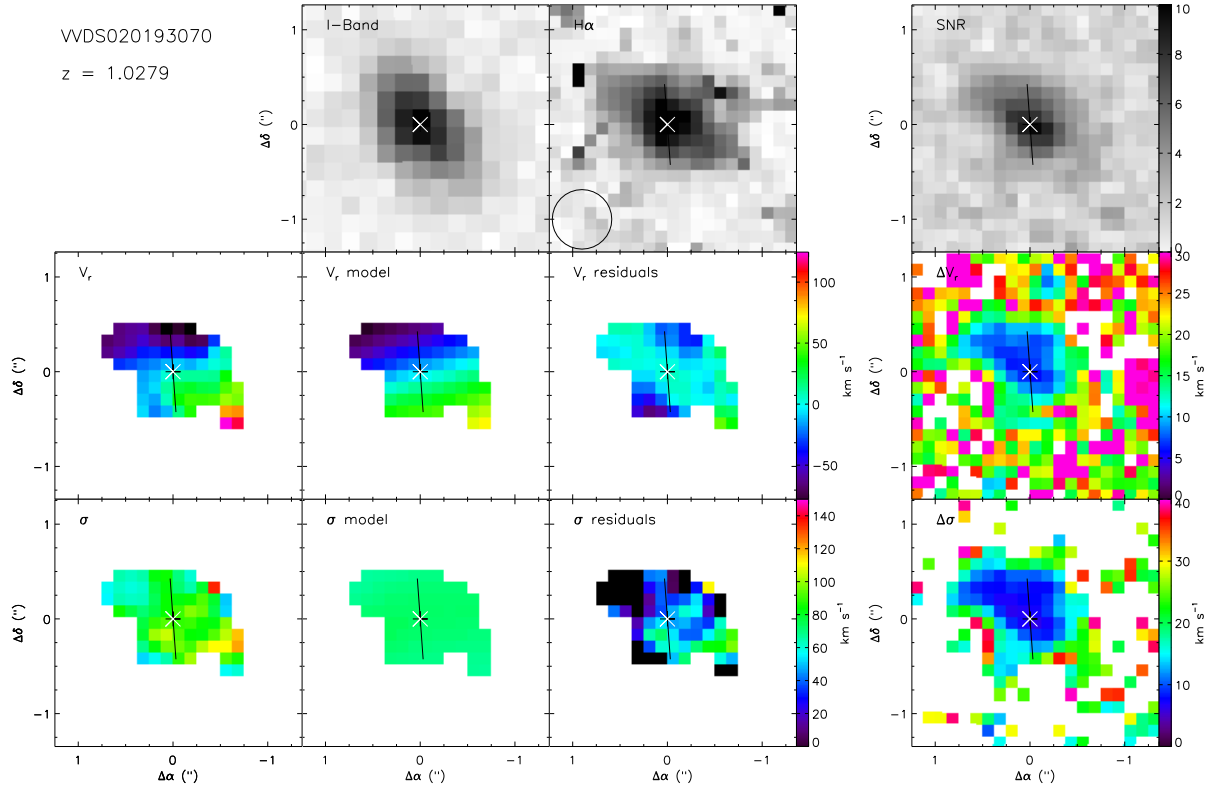


Fig. B.10. Maps for VVDS020193070. Same caption as Figure B.1.

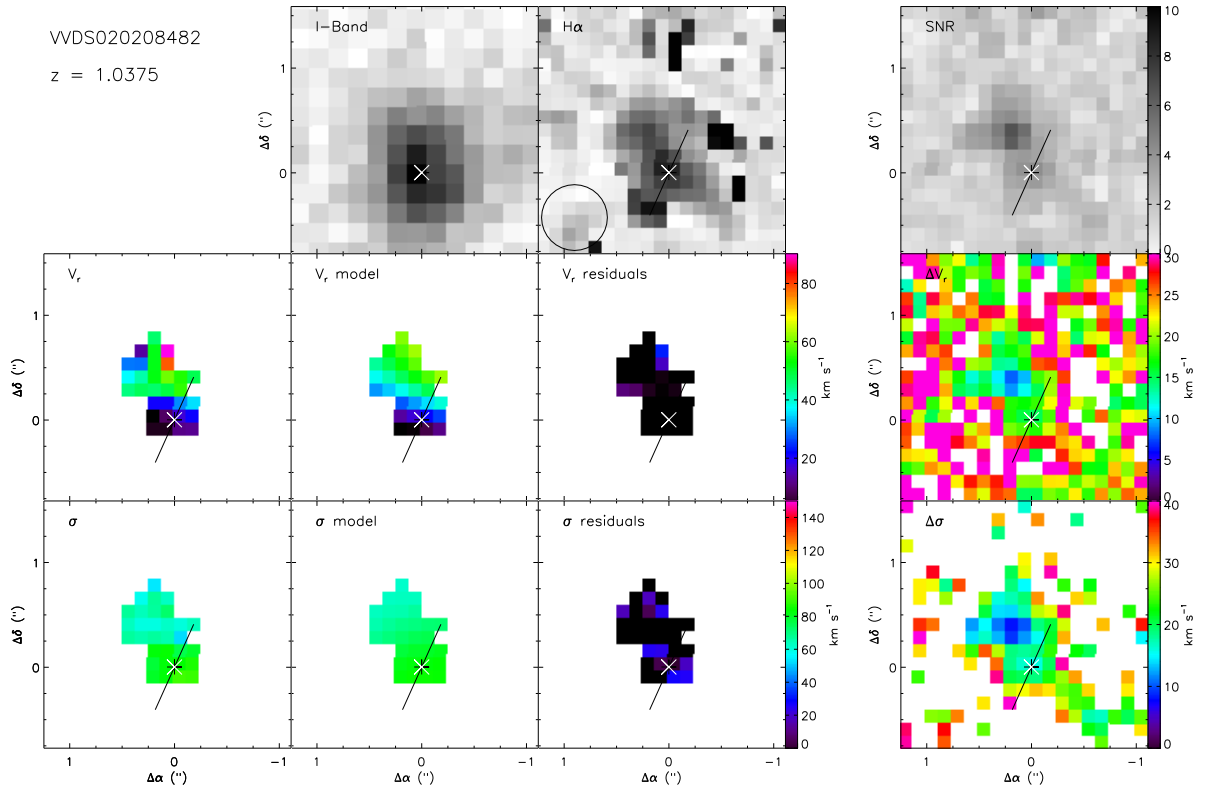
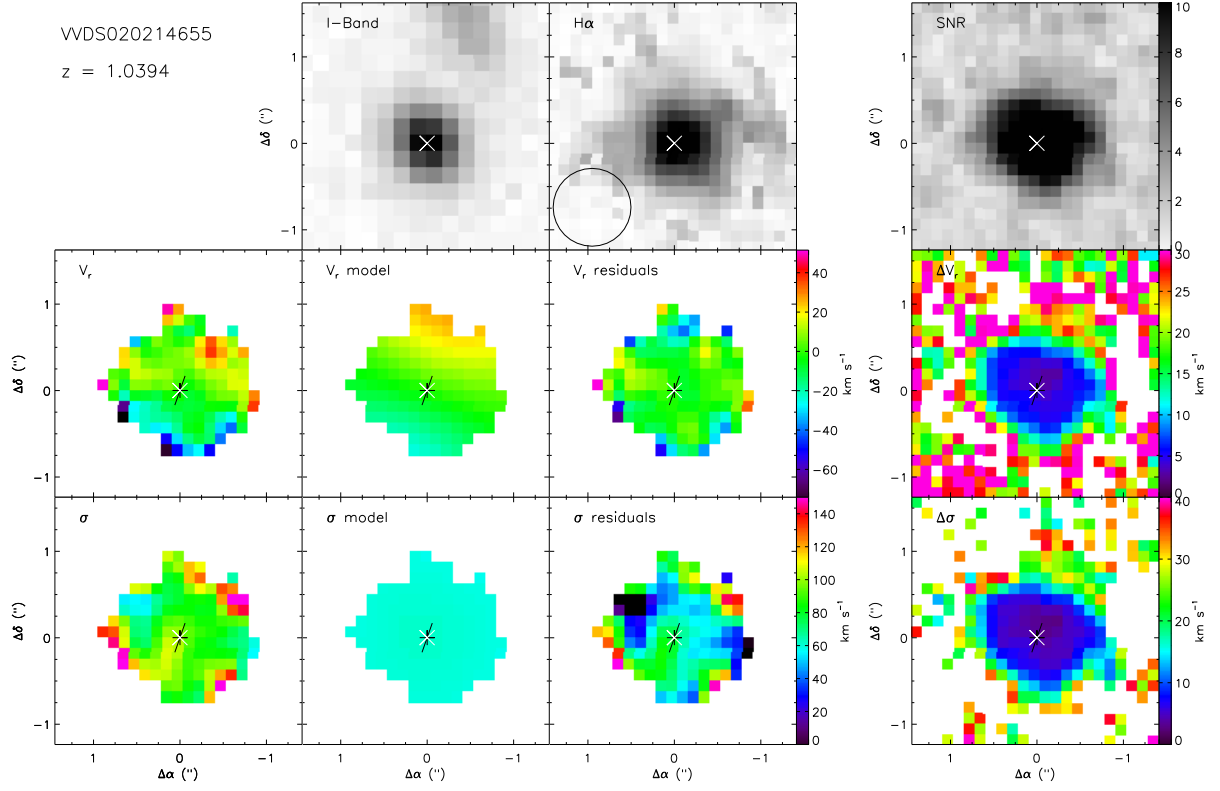
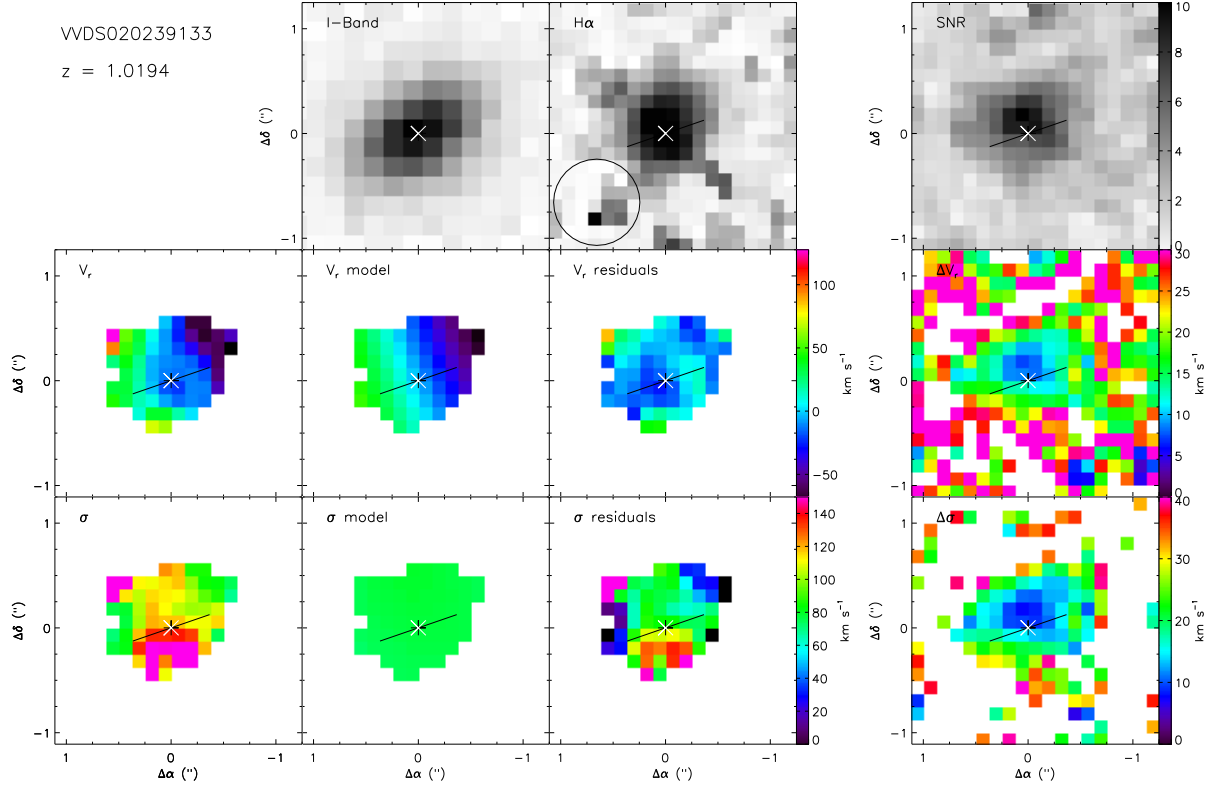


Fig. B.11. Maps for VVDS020208482. Same caption as Figure B.1.





**Fig. B.12.** Maps for VVDS020214655. Same caption as Figure B.1.



**Fig. B.13.** Maps for VVDS020239133. Same caption as Figure B.1.

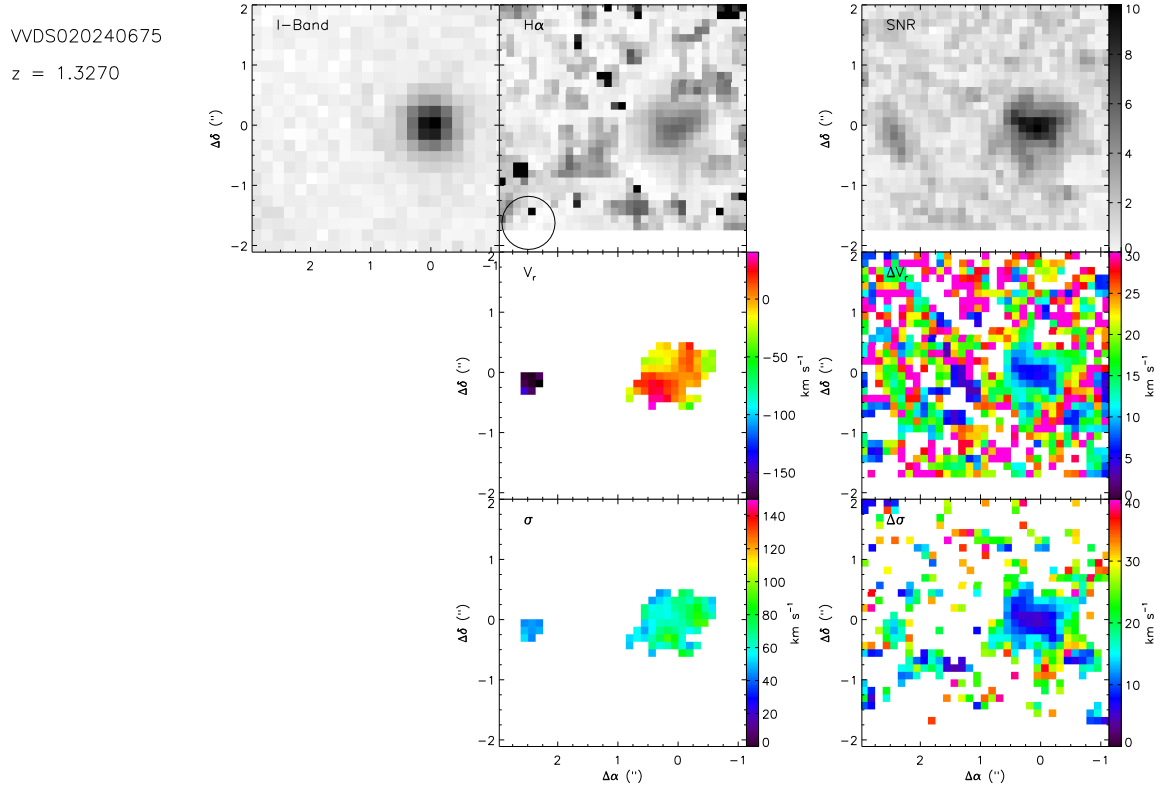


**Fig. B.14.** Maps for VVDS020240675 system. Same caption as Figure B.2.

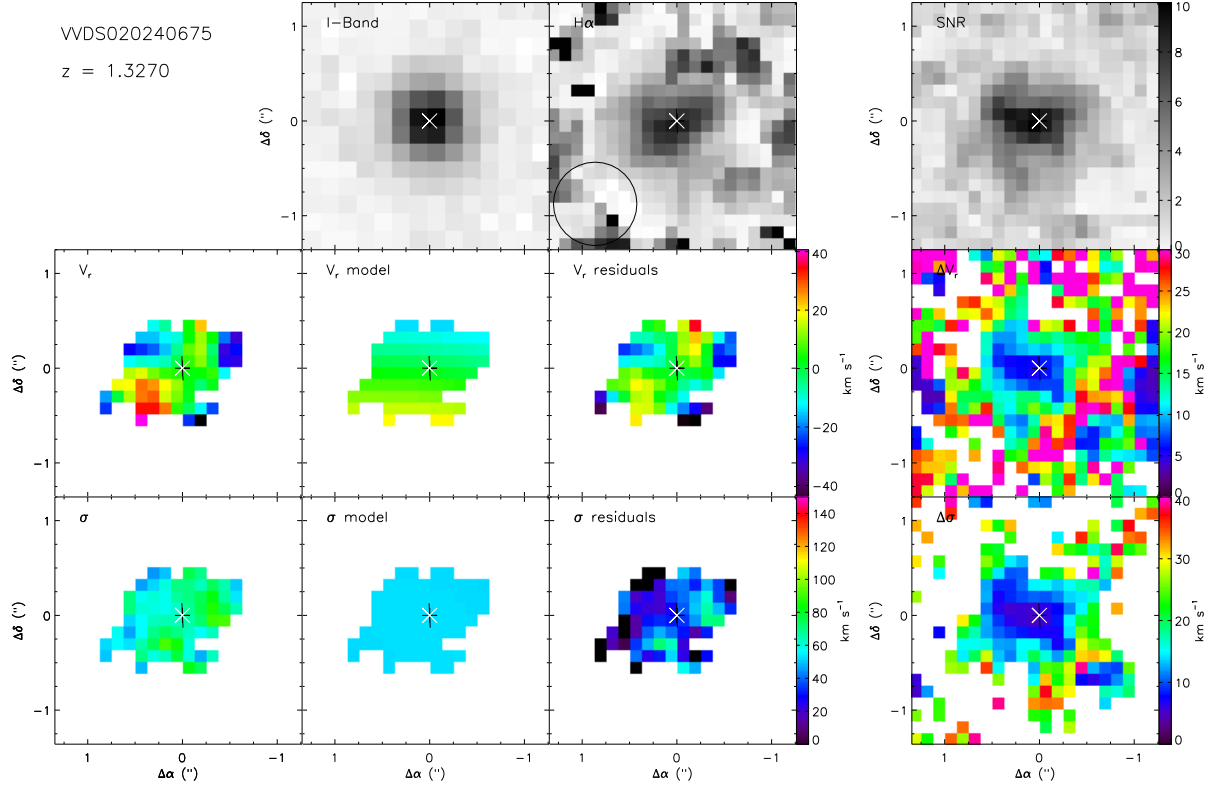


**Fig. B.15.** Maps for VVDS020240675. Same caption as Figure B.1.

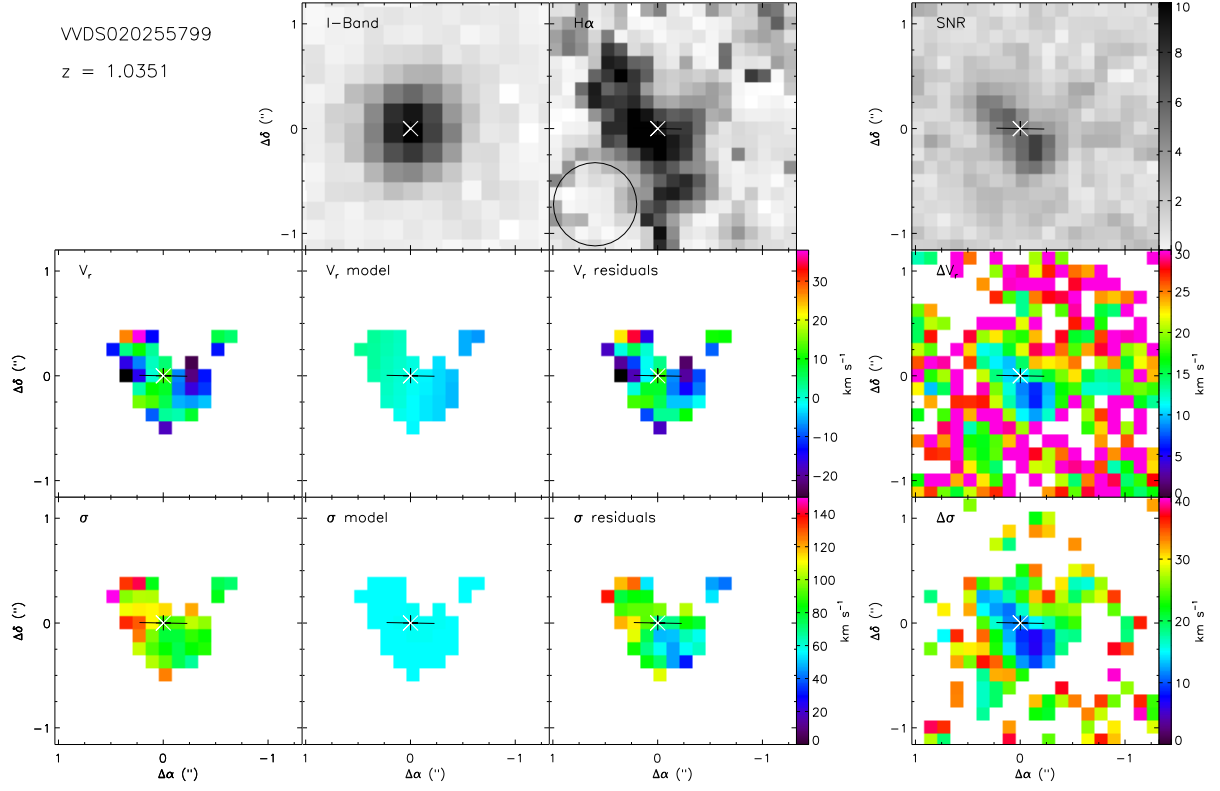


Fig. B.16. Maps for VVDS020255799. Same caption as Figure B.1.

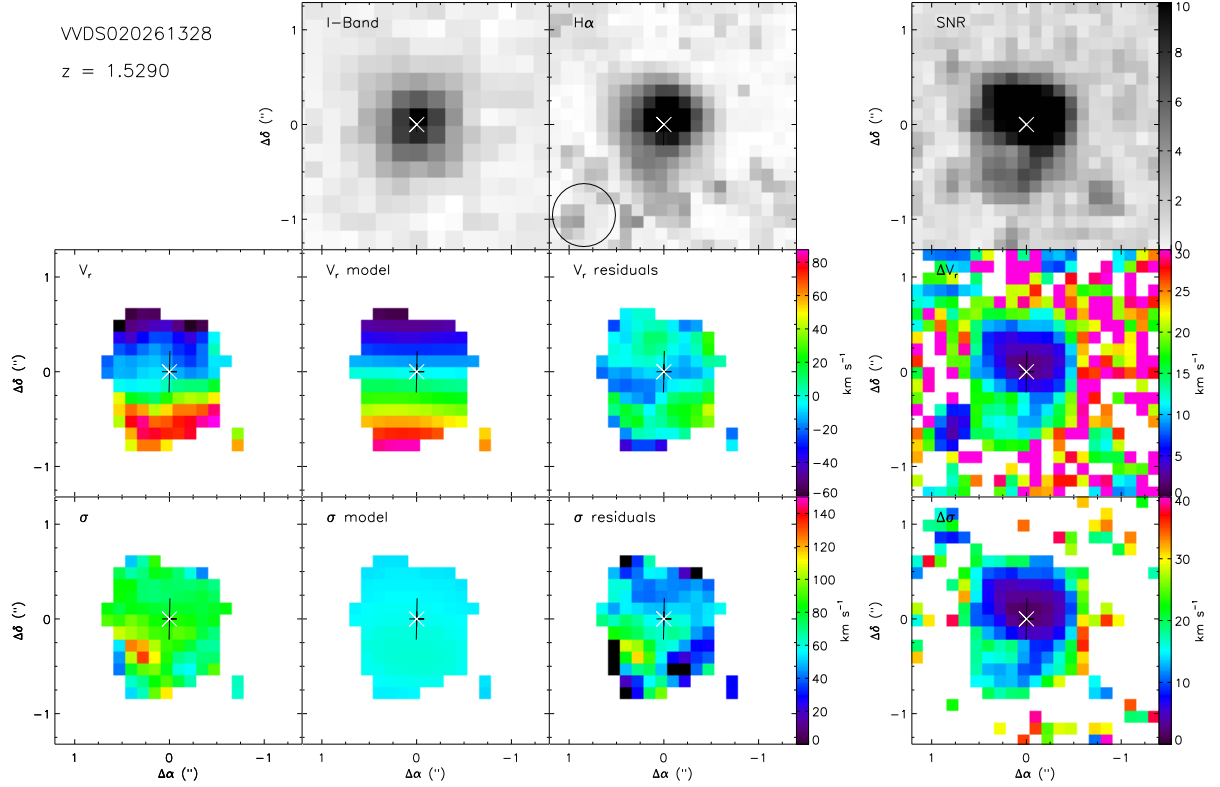


Fig. B.17. Maps for VVDS020261328. Same caption as Figure B.1.

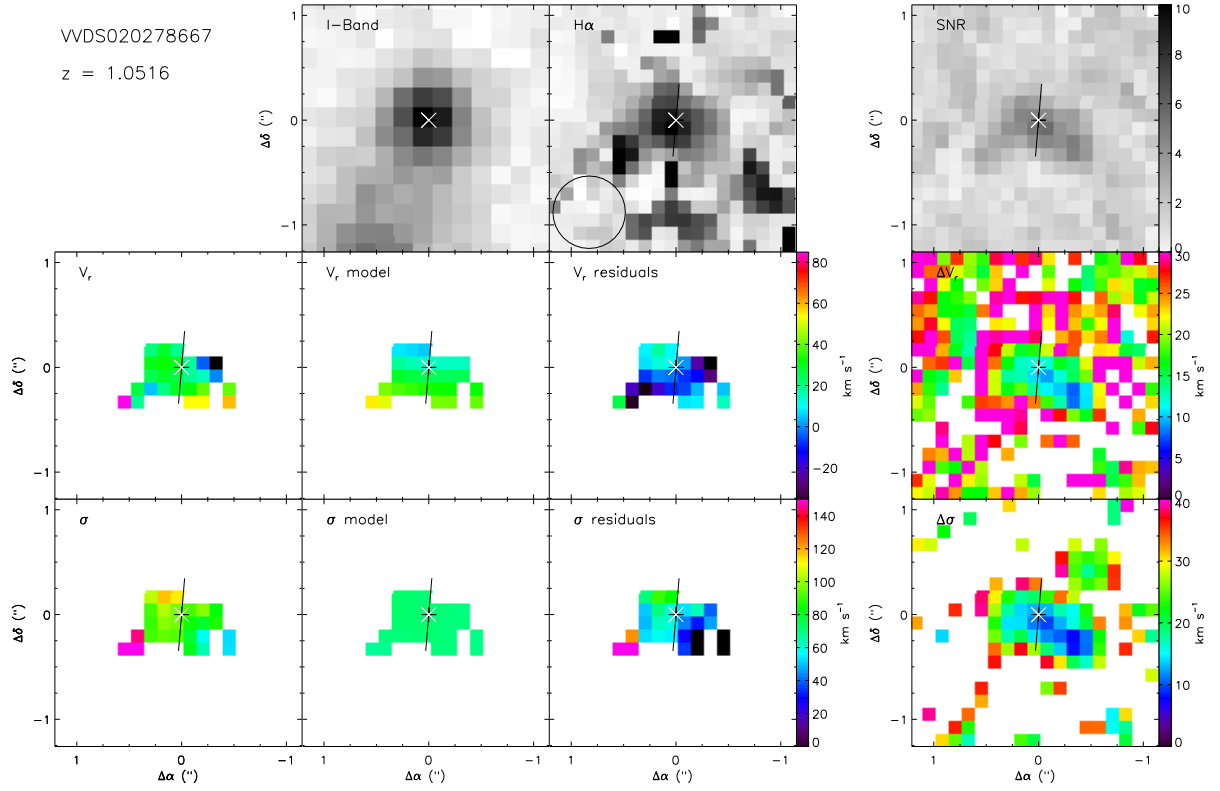


Fig. B.18. Maps for VVDS020278667. Same caption as Figure B.1.

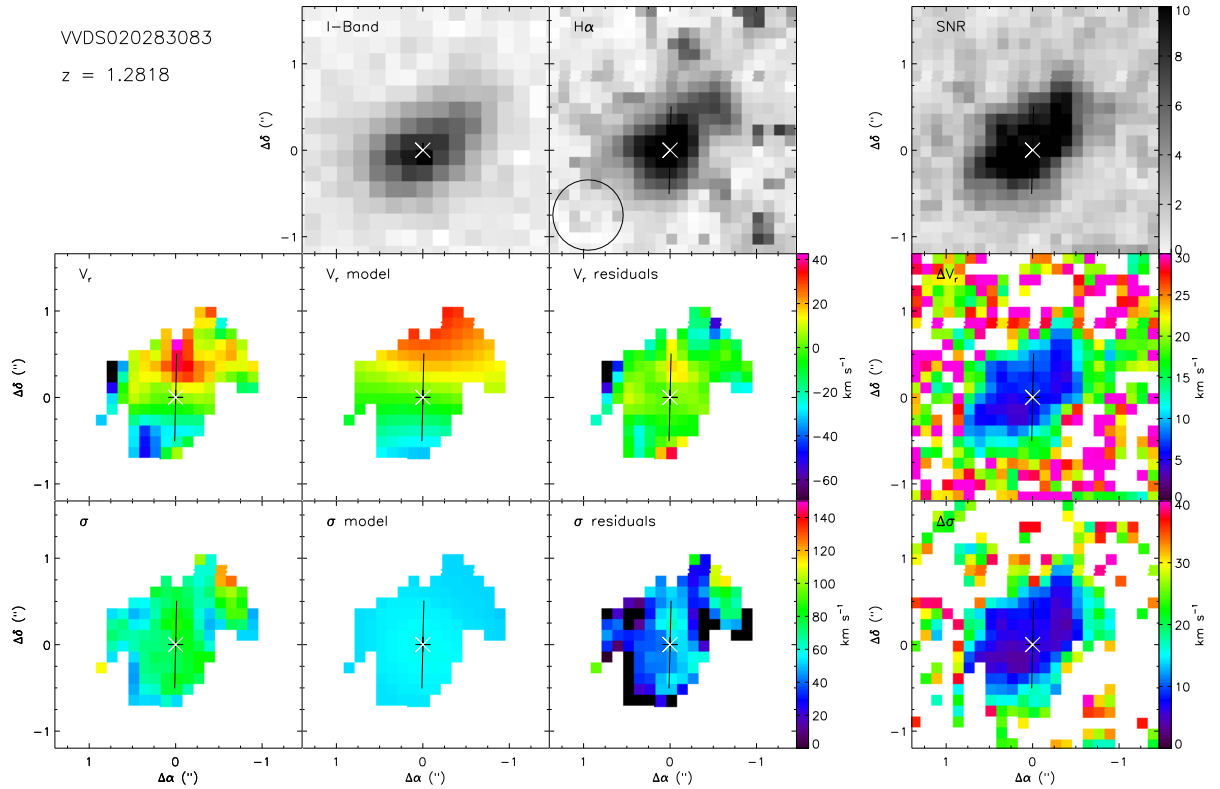
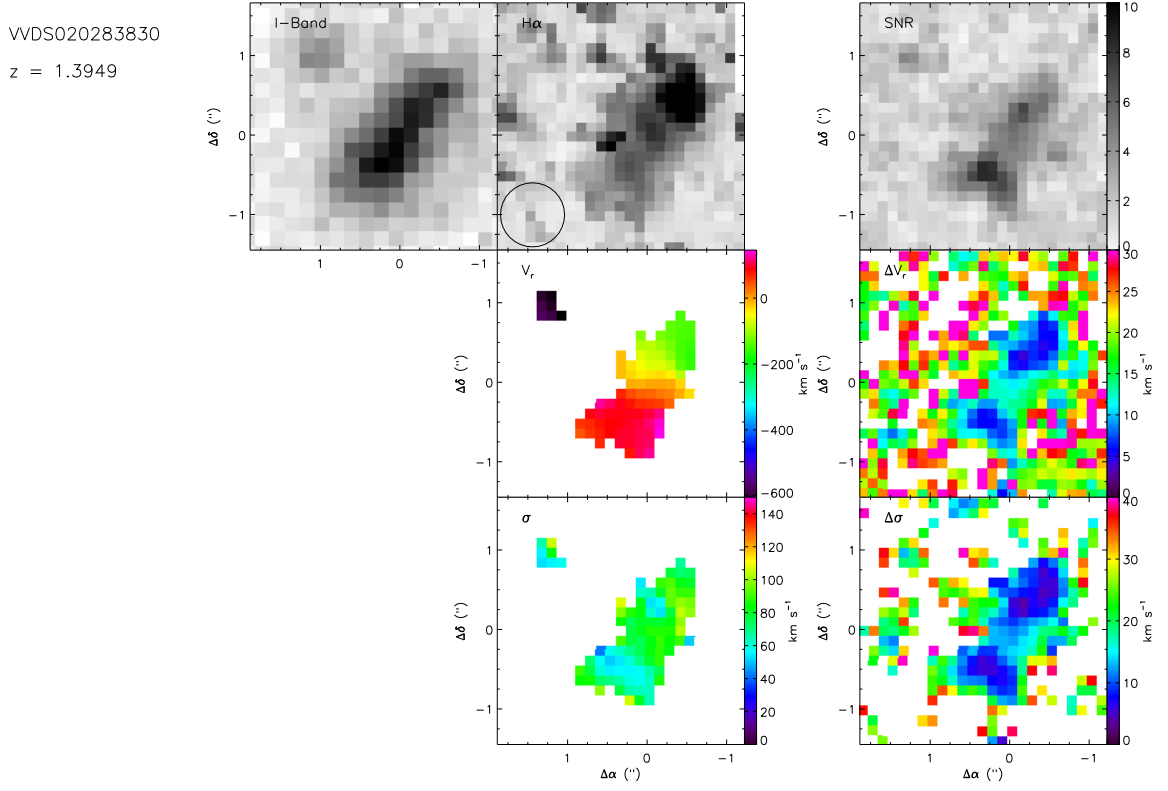
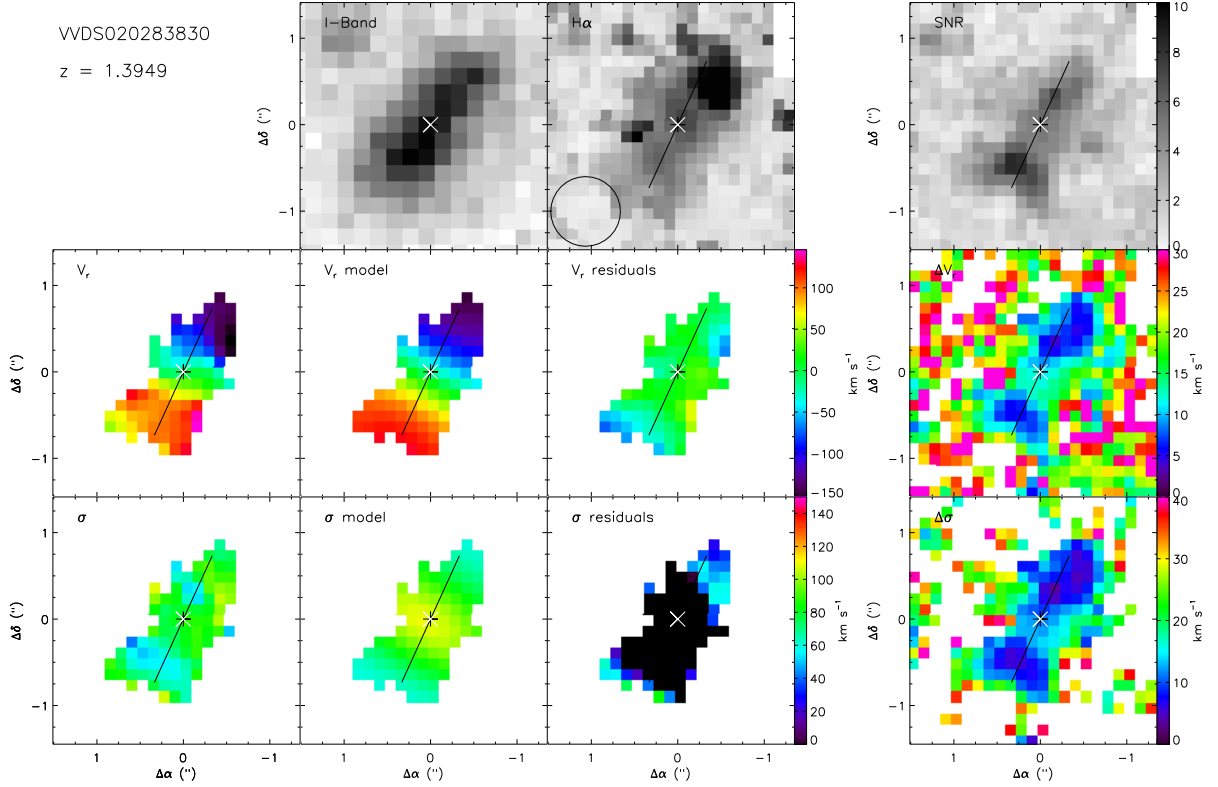


Fig. B.19. Maps for VVDS020283083. Same caption as Figure B.1.



**Fig. B.20.** Maps for VVDS020283830 system. Same caption as Figure B.2.



**Fig. B.21.** Maps for VVDS020283830. Same caption as Figure B.1.

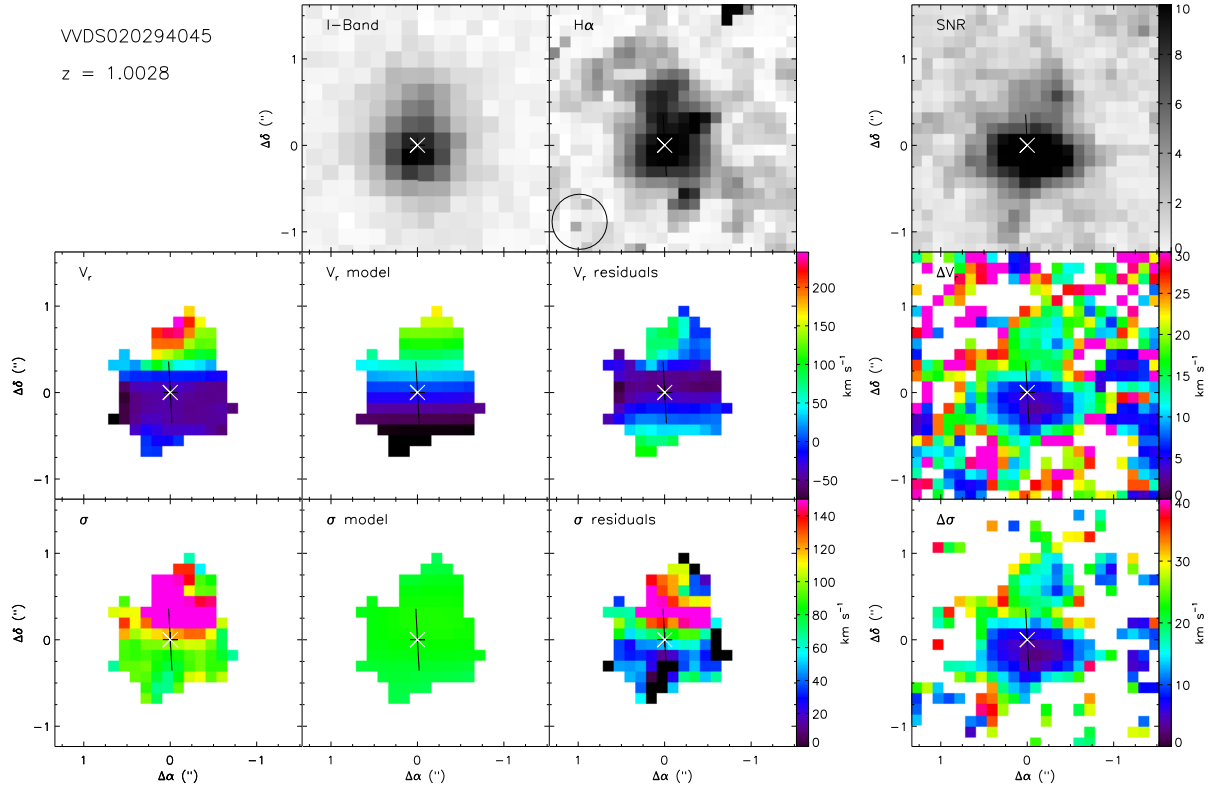


Fig. B.22. Maps for VVDS020294045. Same caption as Figure B.1.

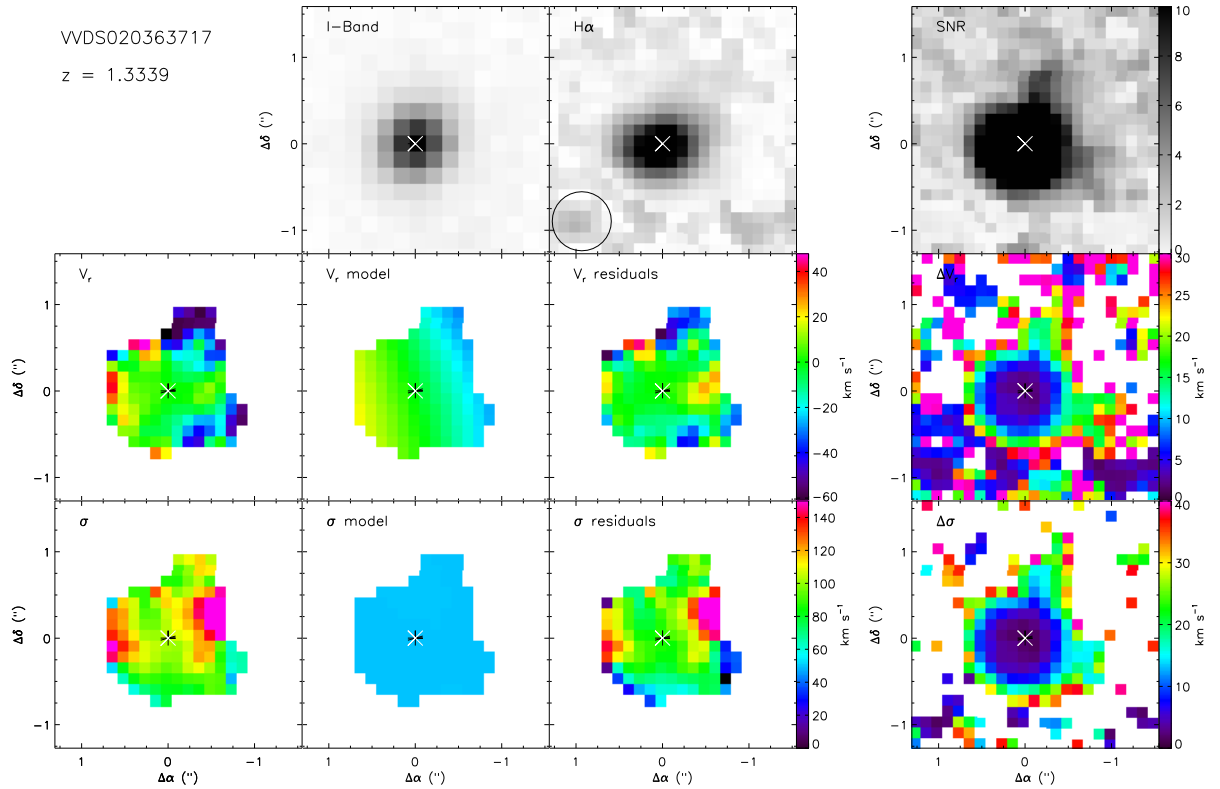
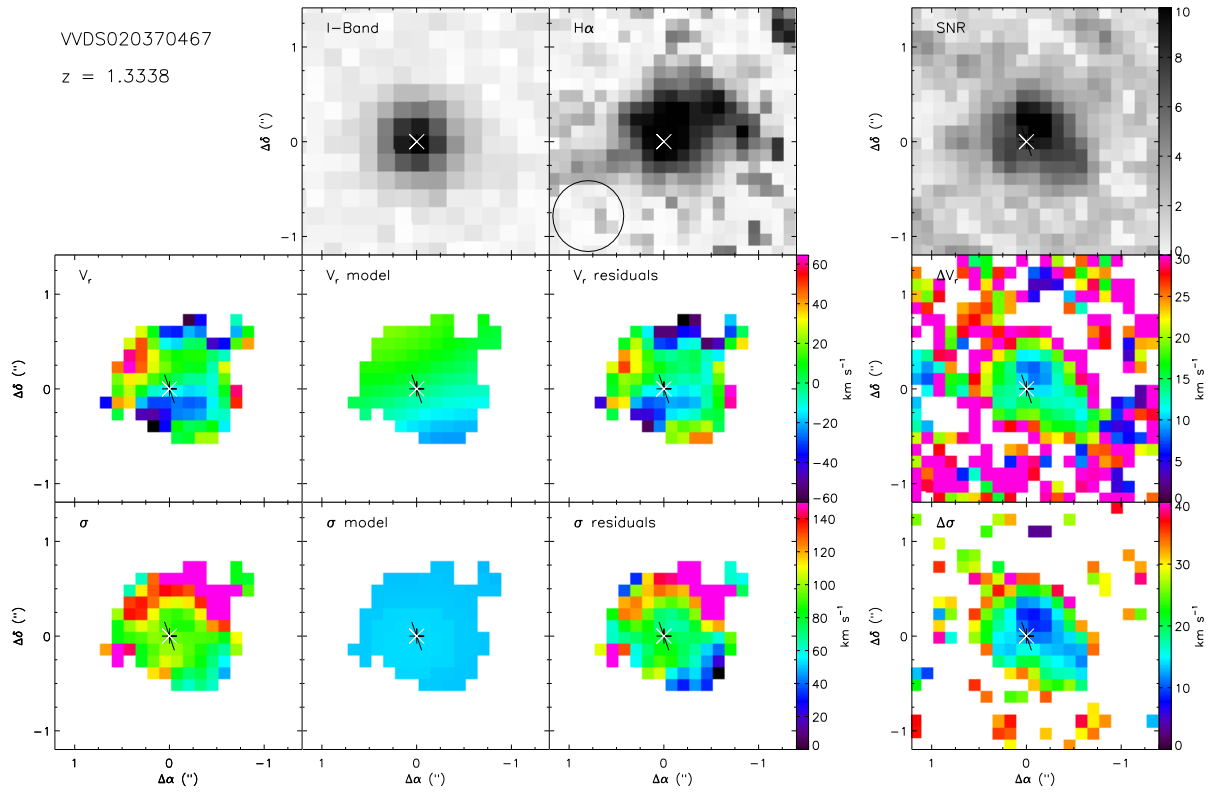
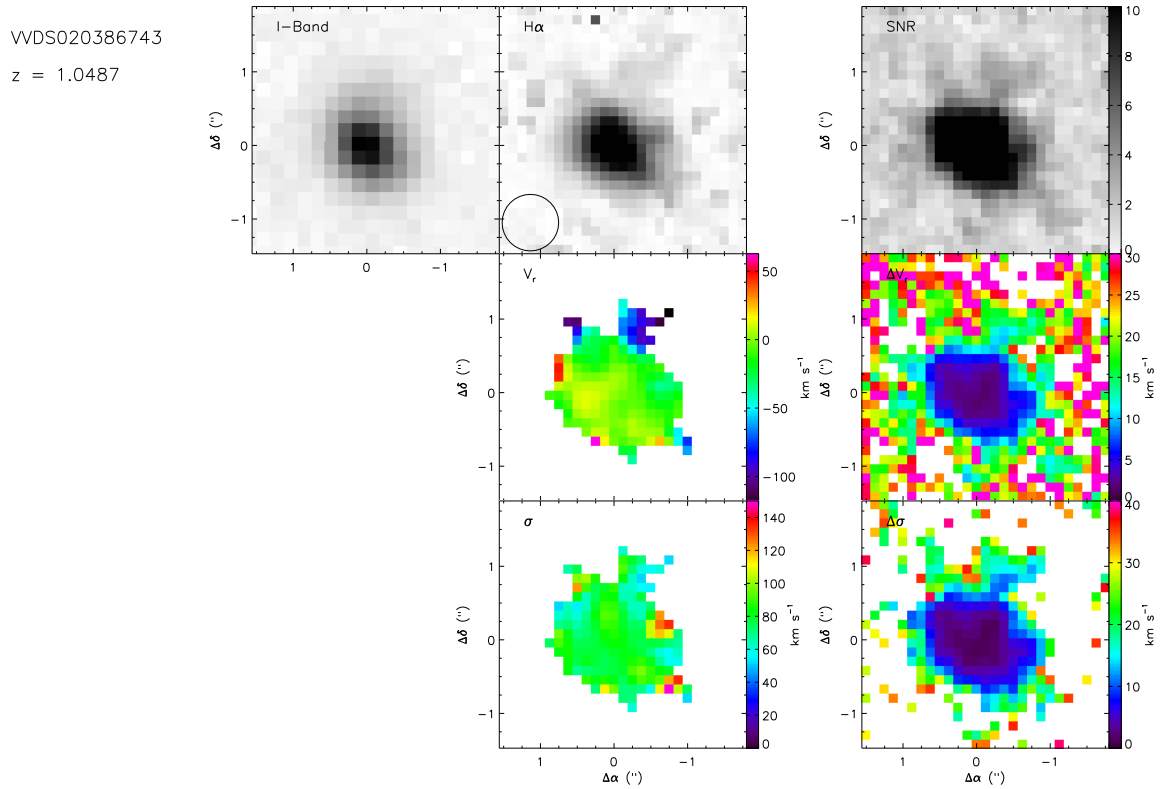


Fig. B.23. Maps for VVDS020363717. Same caption as Figure B.1.



**Fig. B.24.** Maps for WVDS020370467. Same caption as Figure B.1.



**Fig. B.25.** Maps for WVDS020386743 system. Same caption as Figure B.2.



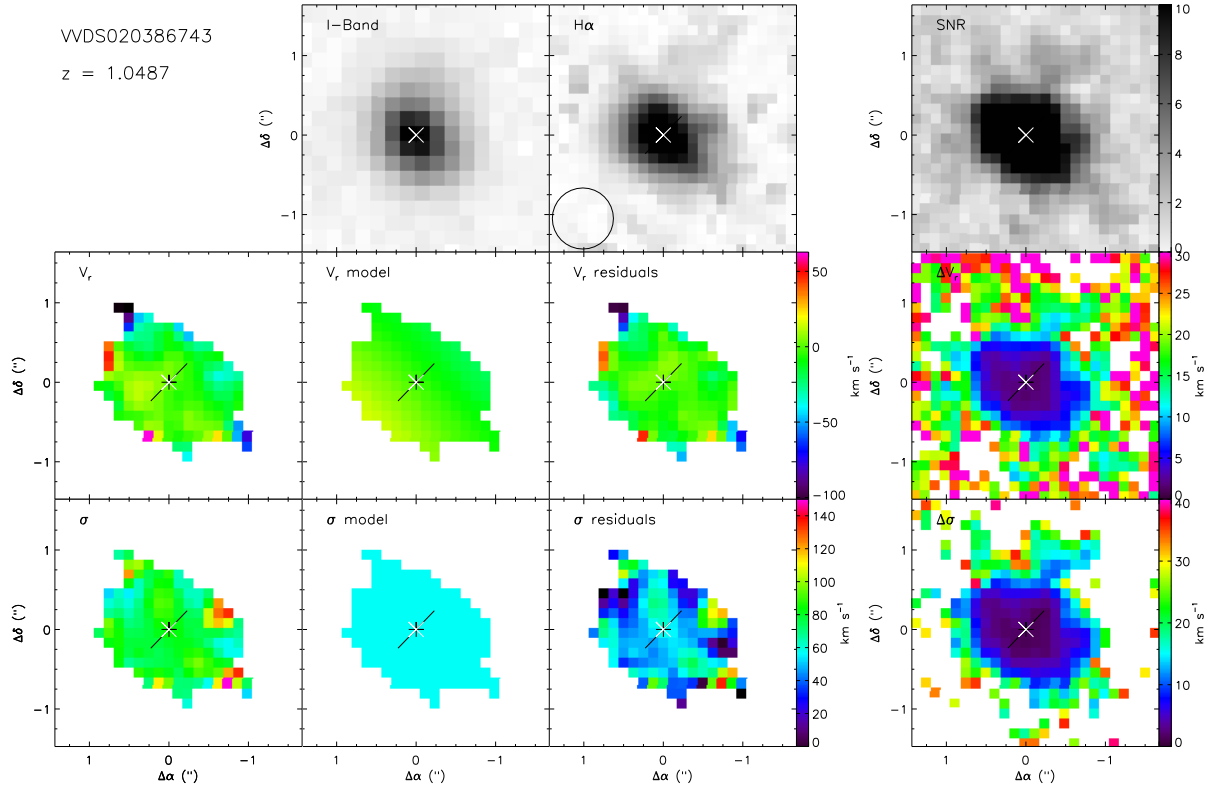


Fig. B.26. Maps for VVDS020386743. Same caption as Figure B.1.

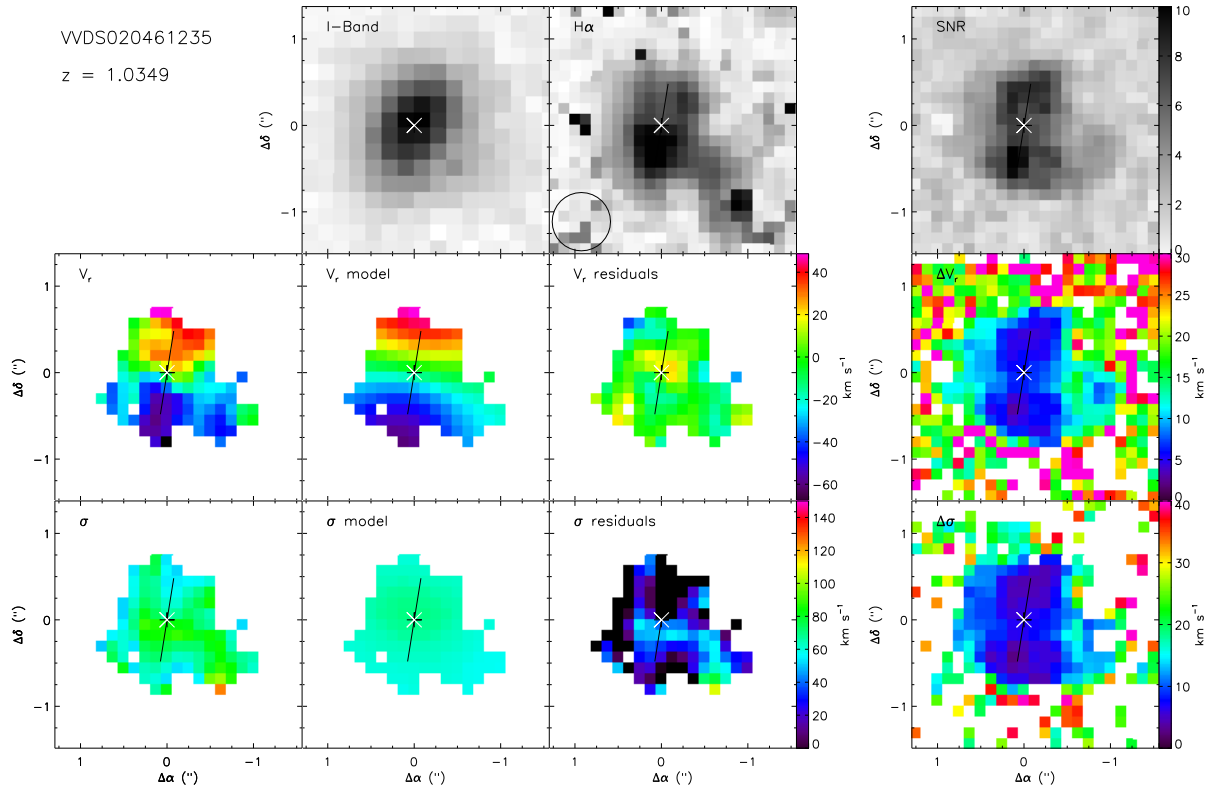
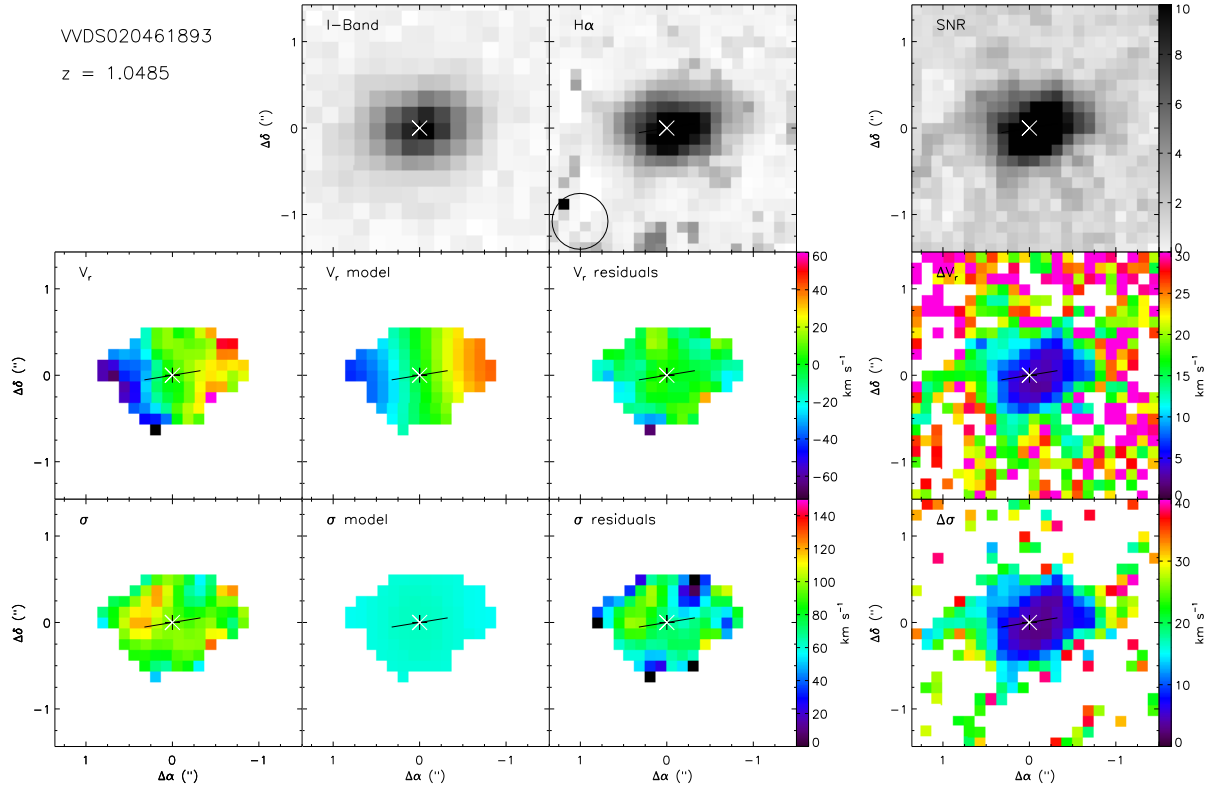
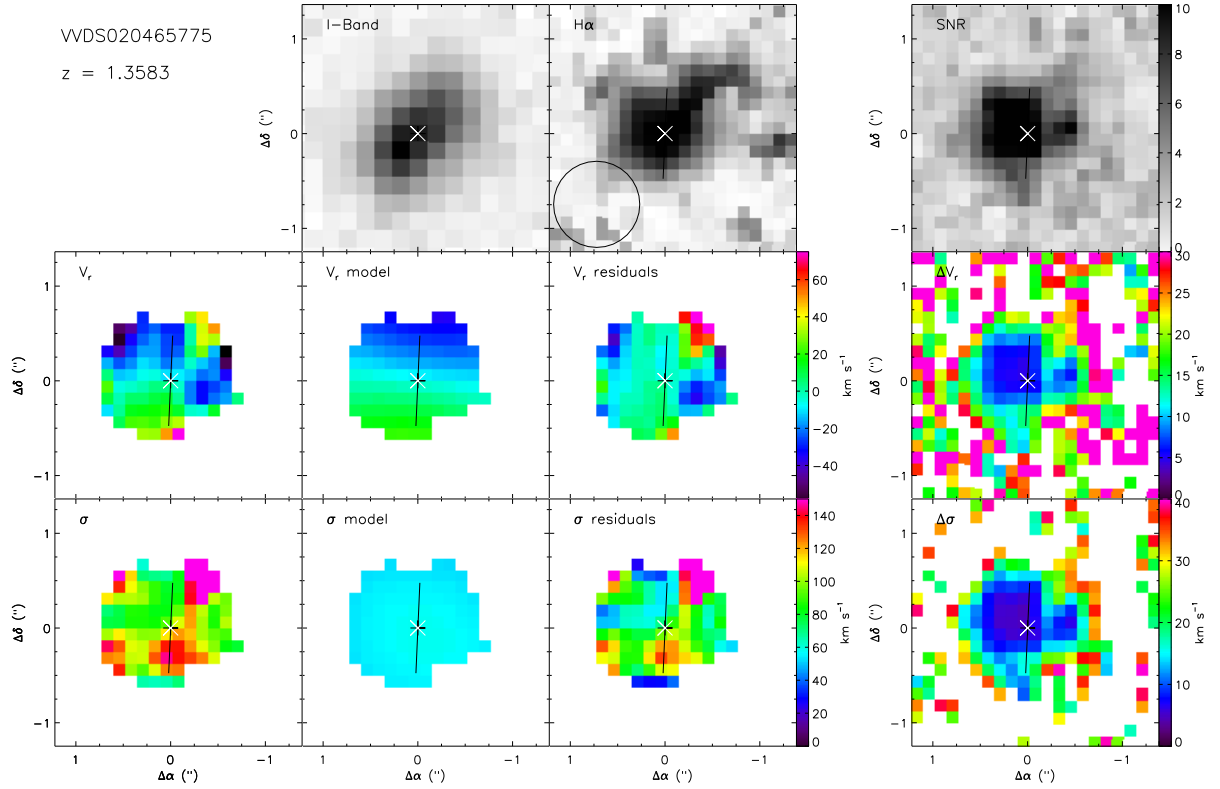


Fig. B.27. Maps for VVDS020461235. Same caption as Figure B.1.



**Fig. B.28.** Maps for VVDS020461893. Same caption as Figure B.1.



**Fig. B.29.** Maps for VVDS020465775. Same caption as Figure B.1.

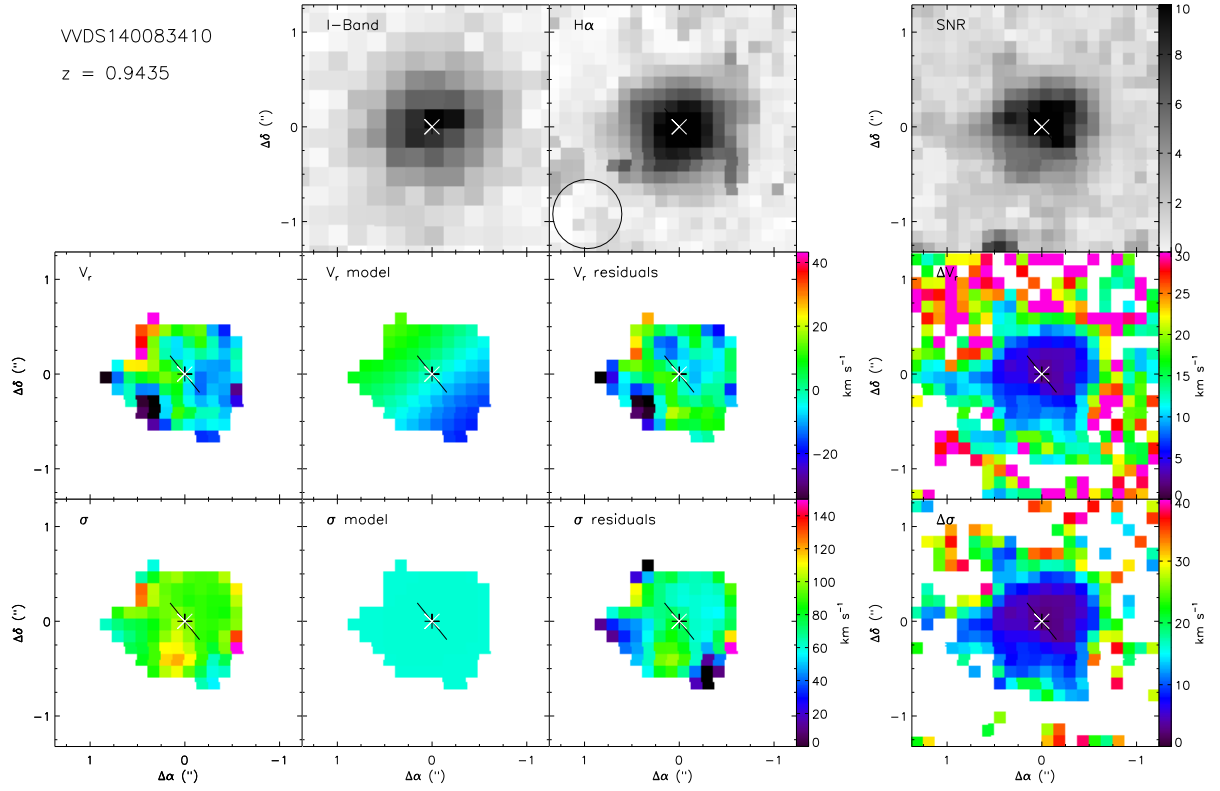


**Fig. B.30.** Maps for VVDS140083410. Same caption as Figure B.1.

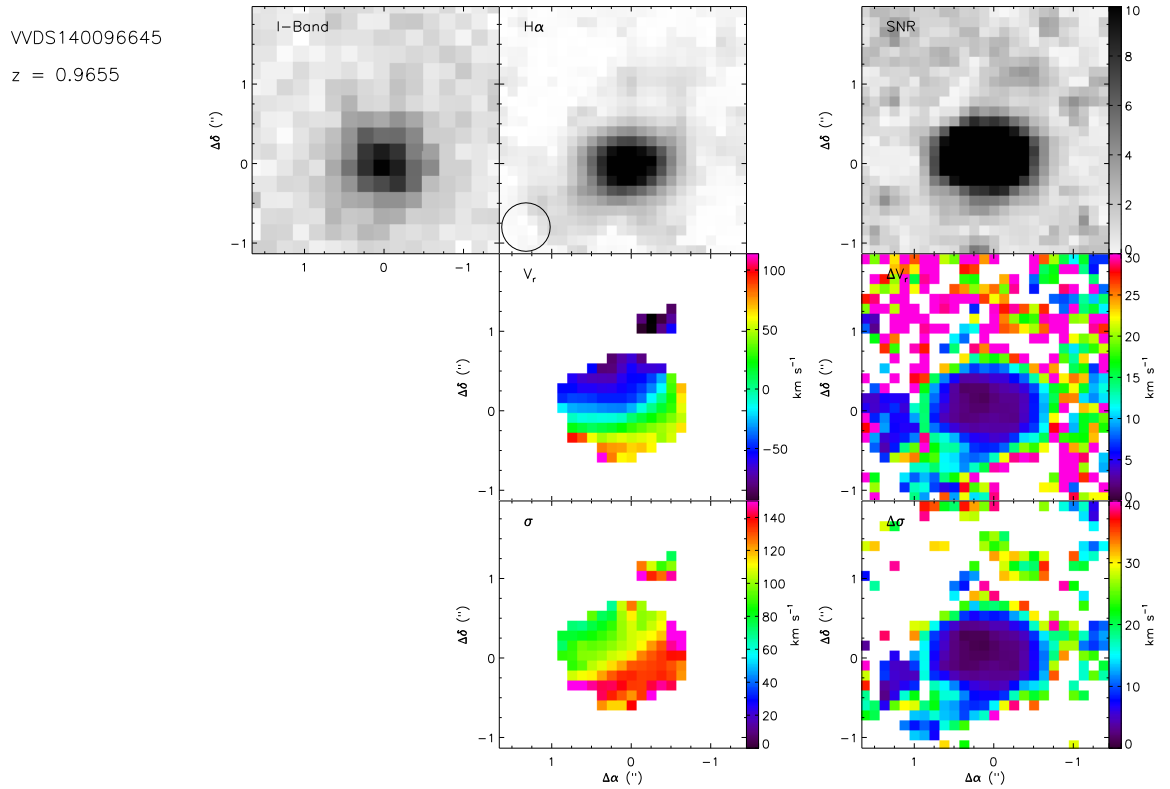


**Fig. B.31.** Maps for VVDS140096645 system. Same caption as Figure B.2.

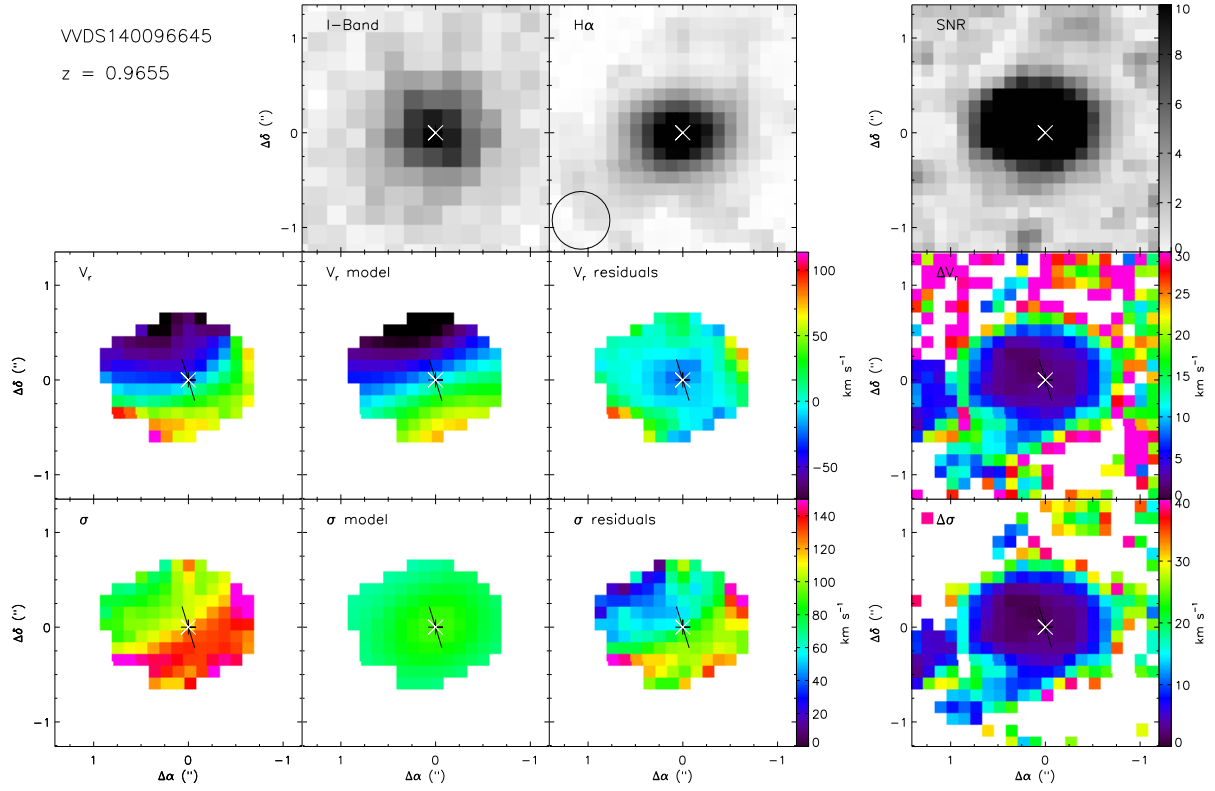


**Fig. B.32.** Maps for WVDS140096645. Same caption as Figure B.1.

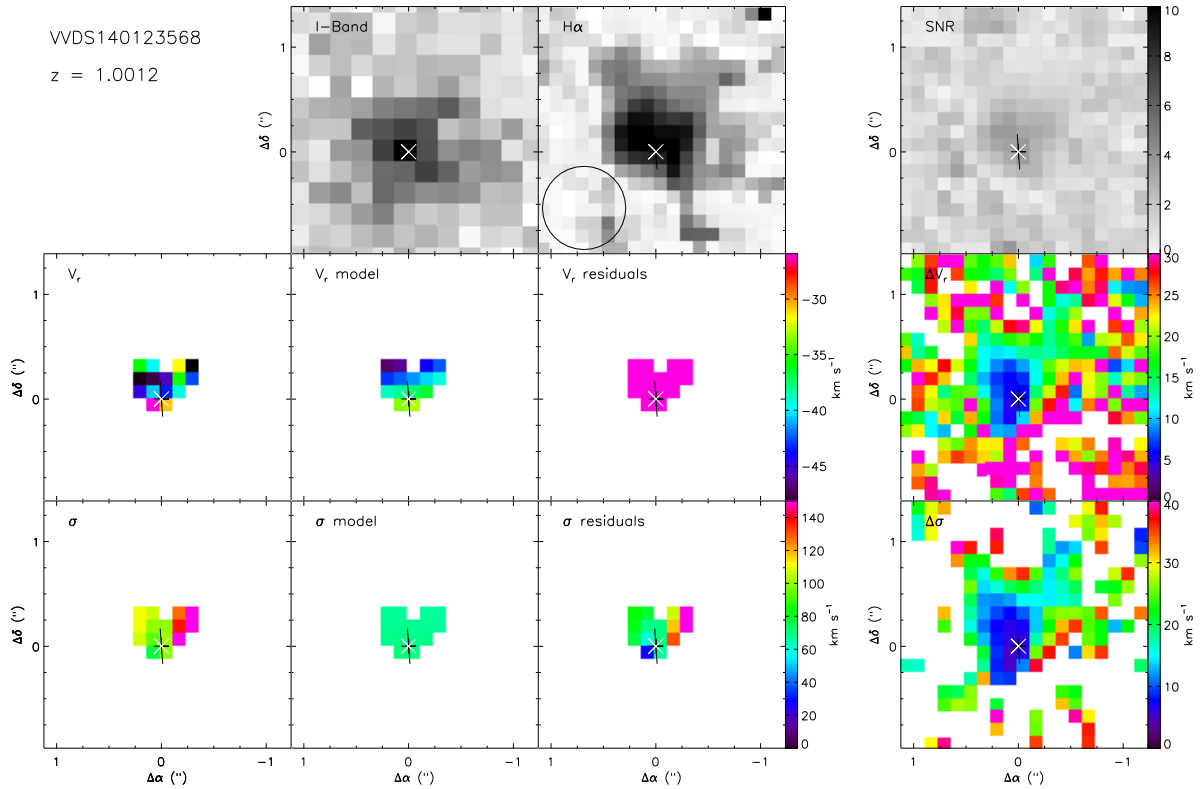


**Fig. B.33.** Maps for WVDS140123568. Same caption as Figure B.1.

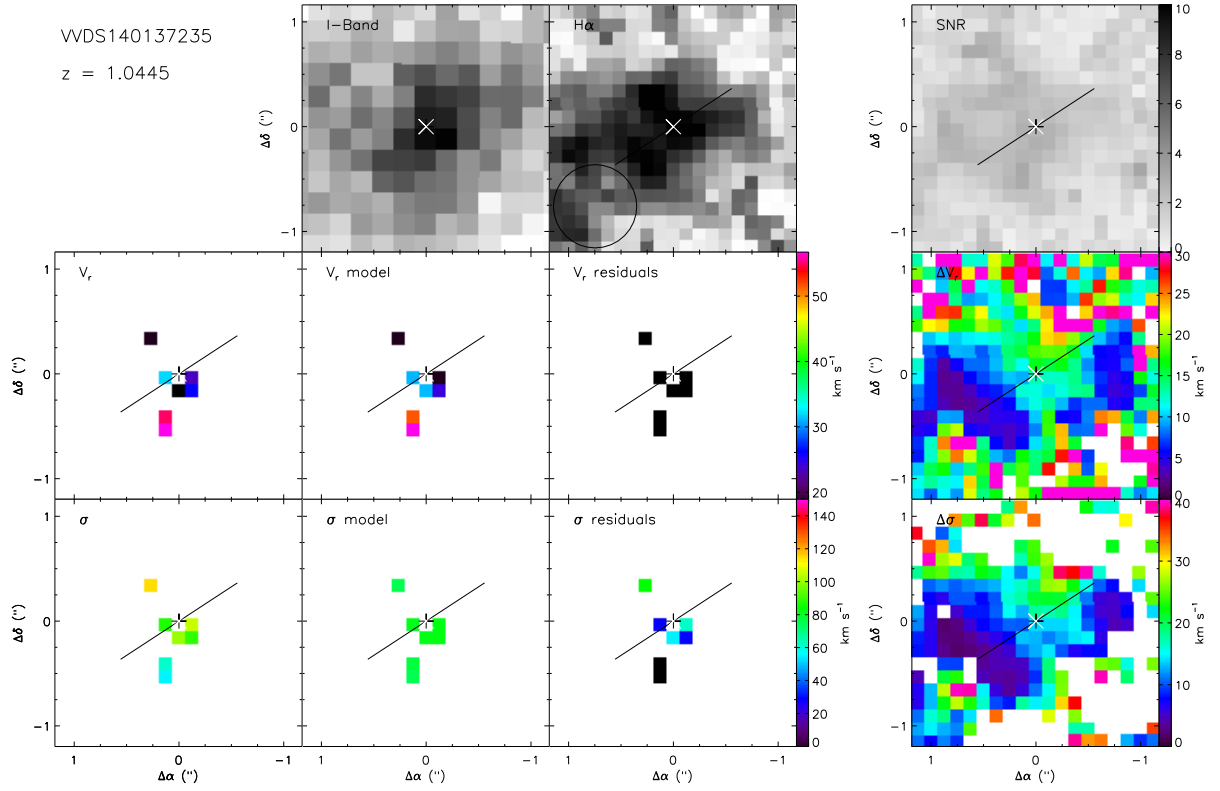


Fig. B.34. Maps for WVDS140137235. Same caption as Figure B.1.

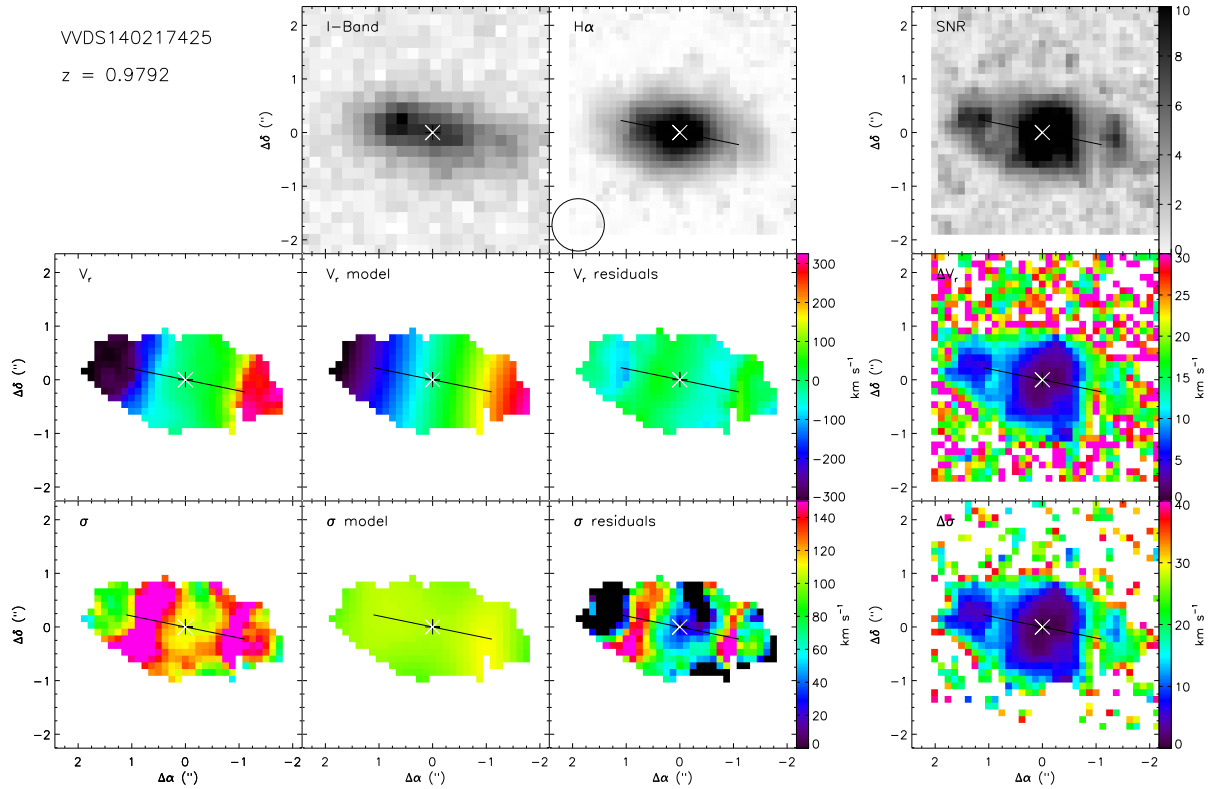


Fig. B.35. Maps for WVDS140217425. Same caption as Figure B.1.

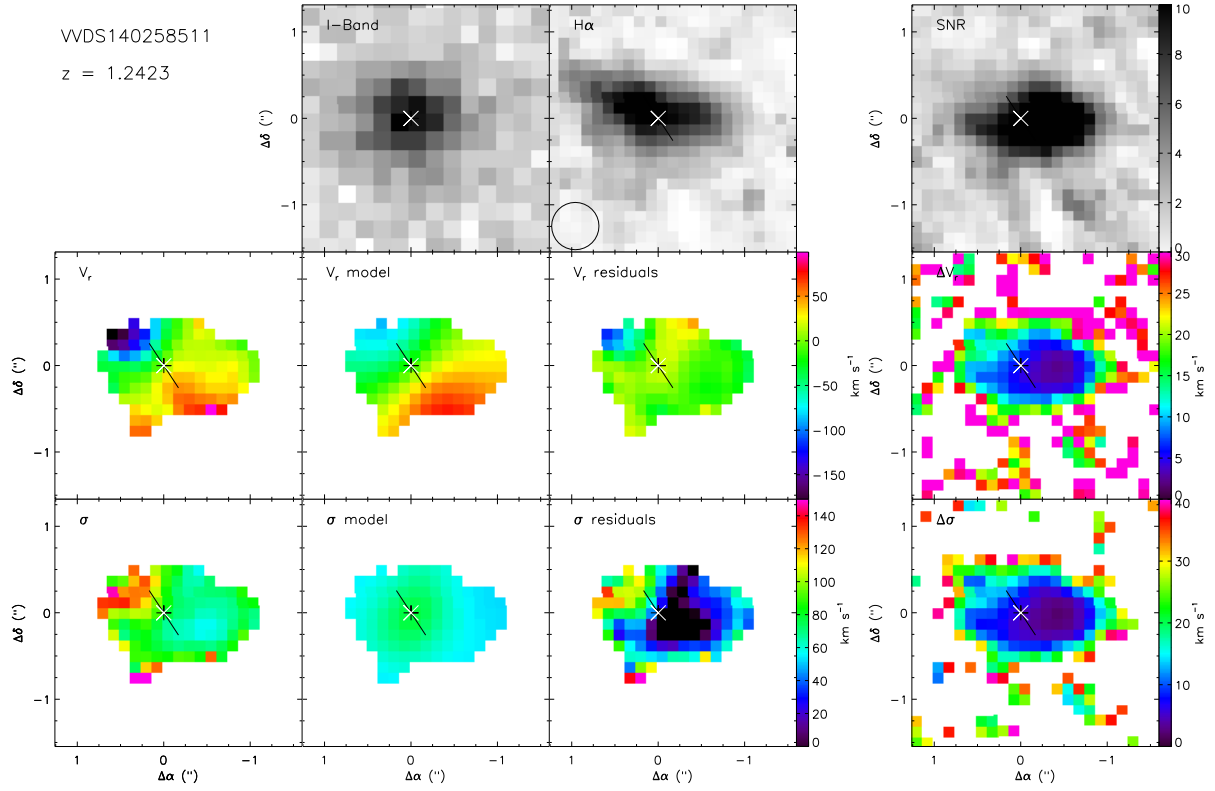


Fig. B.36. Maps for VVDS140258511. Same caption as Figure B.1.

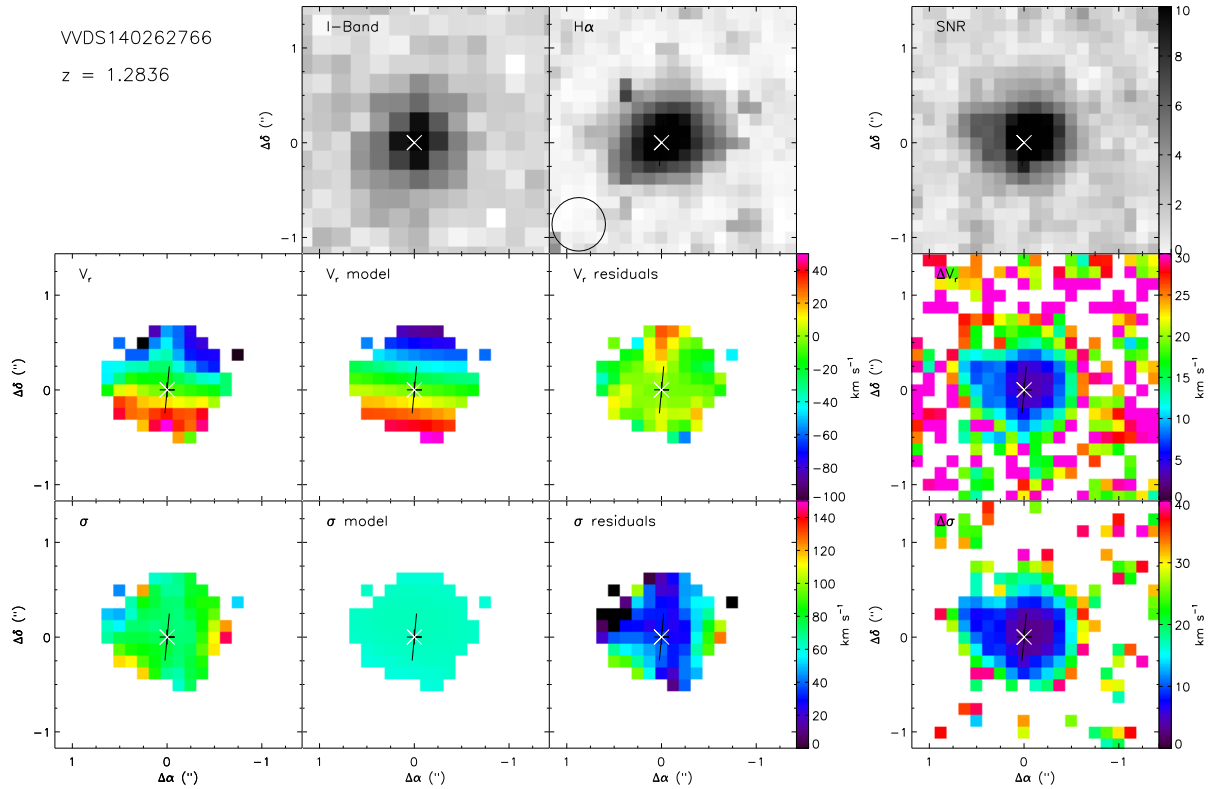


Fig. B.37. Maps for VVDS140262766. Same caption as Figure B.1.

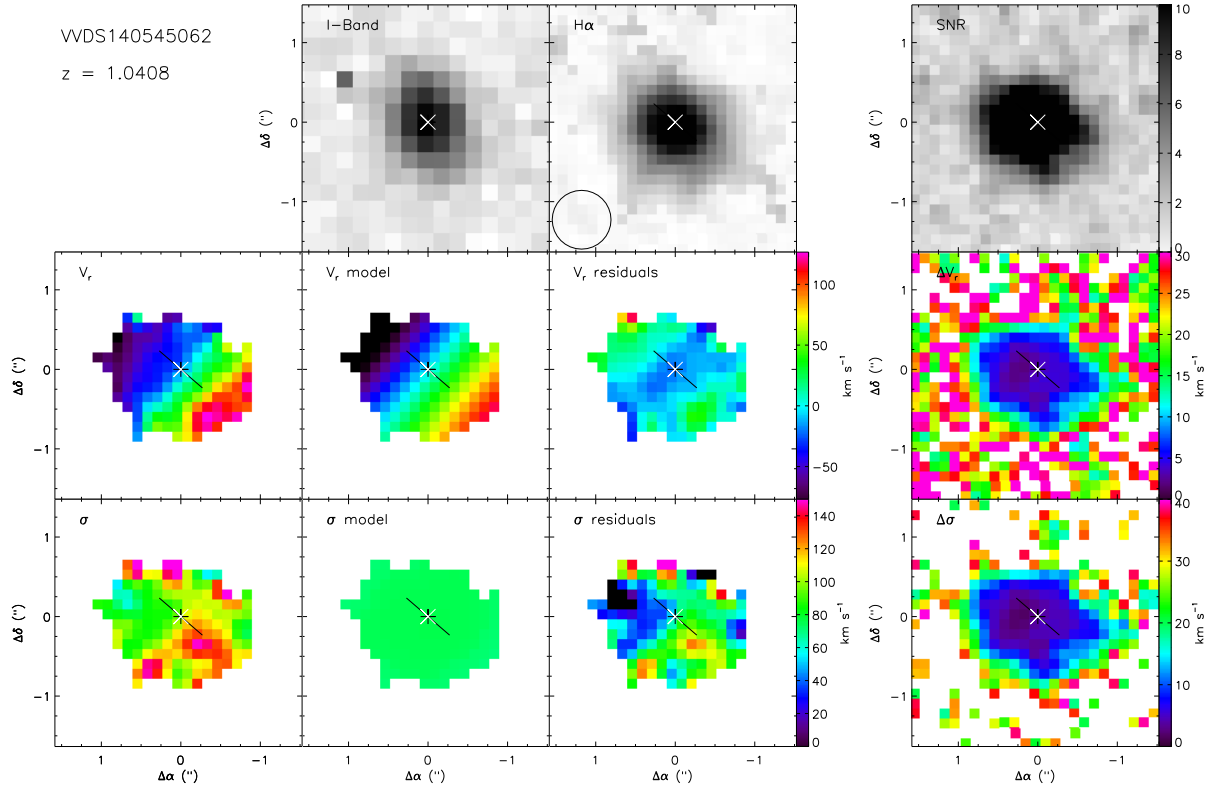


Fig. B.38. Maps for VVDS140545062. Same caption as Figure B.1.

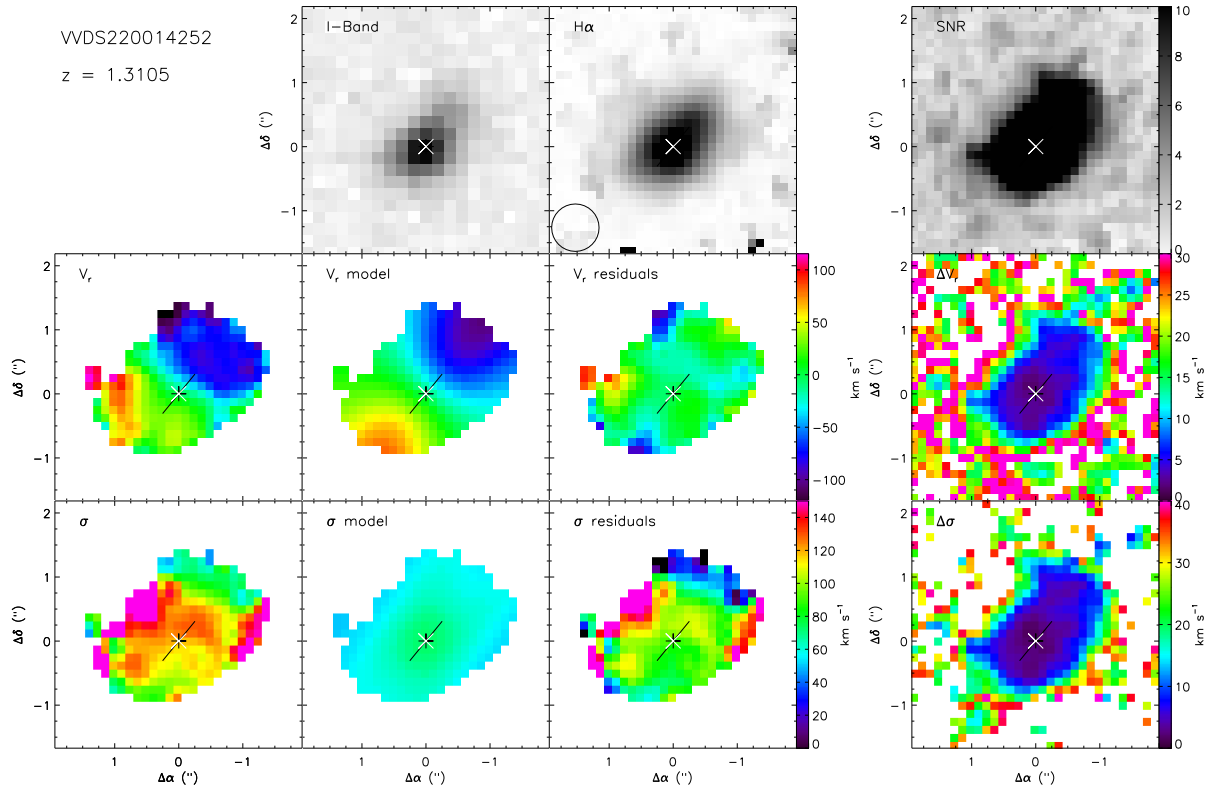


Fig. B.39. Maps for VVDS220014252. Same caption as Figure B.1.

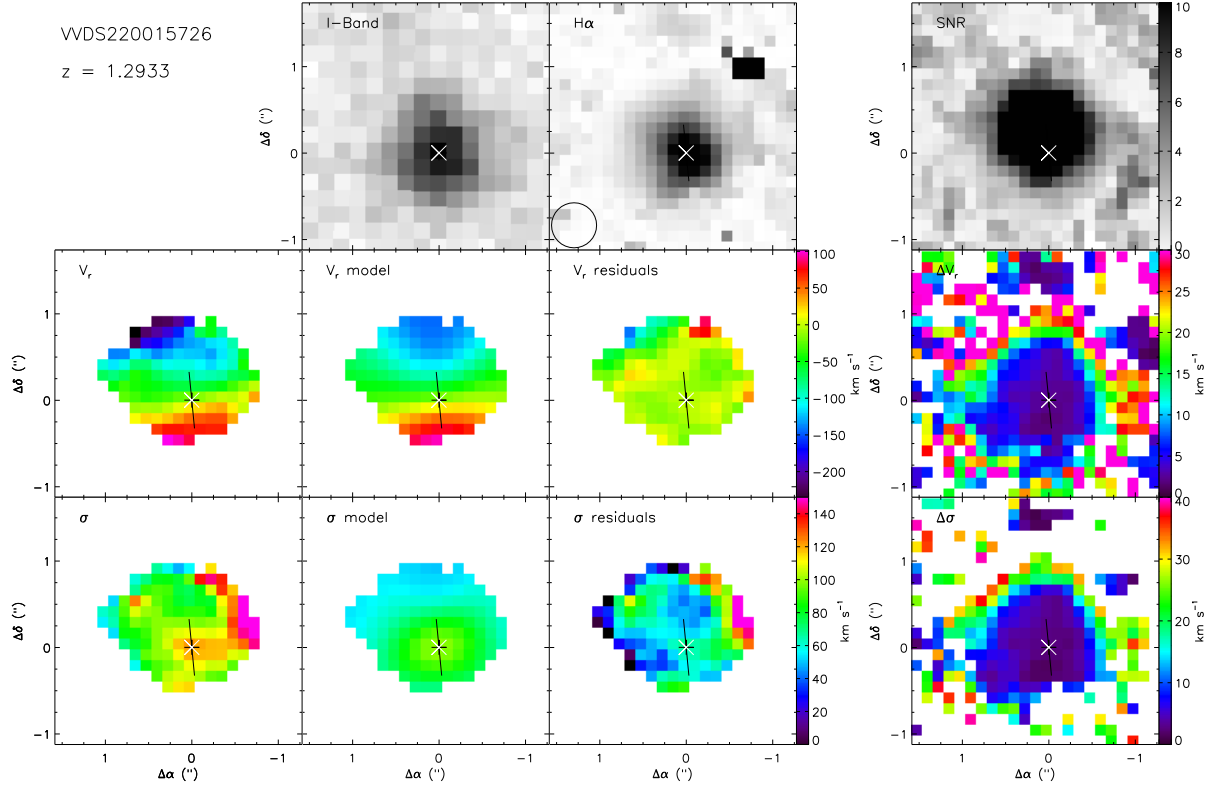


Fig. B.40. Maps for VVDS220015726. Same caption as Figure B.1.

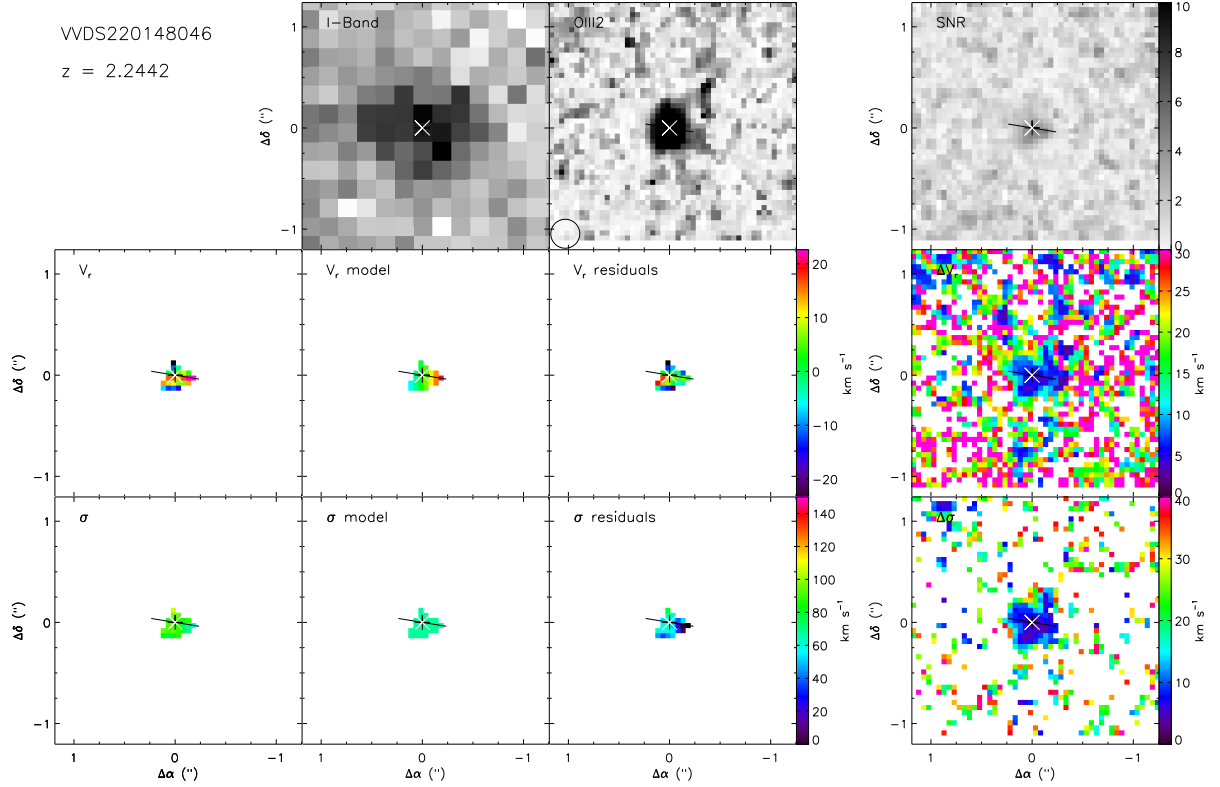
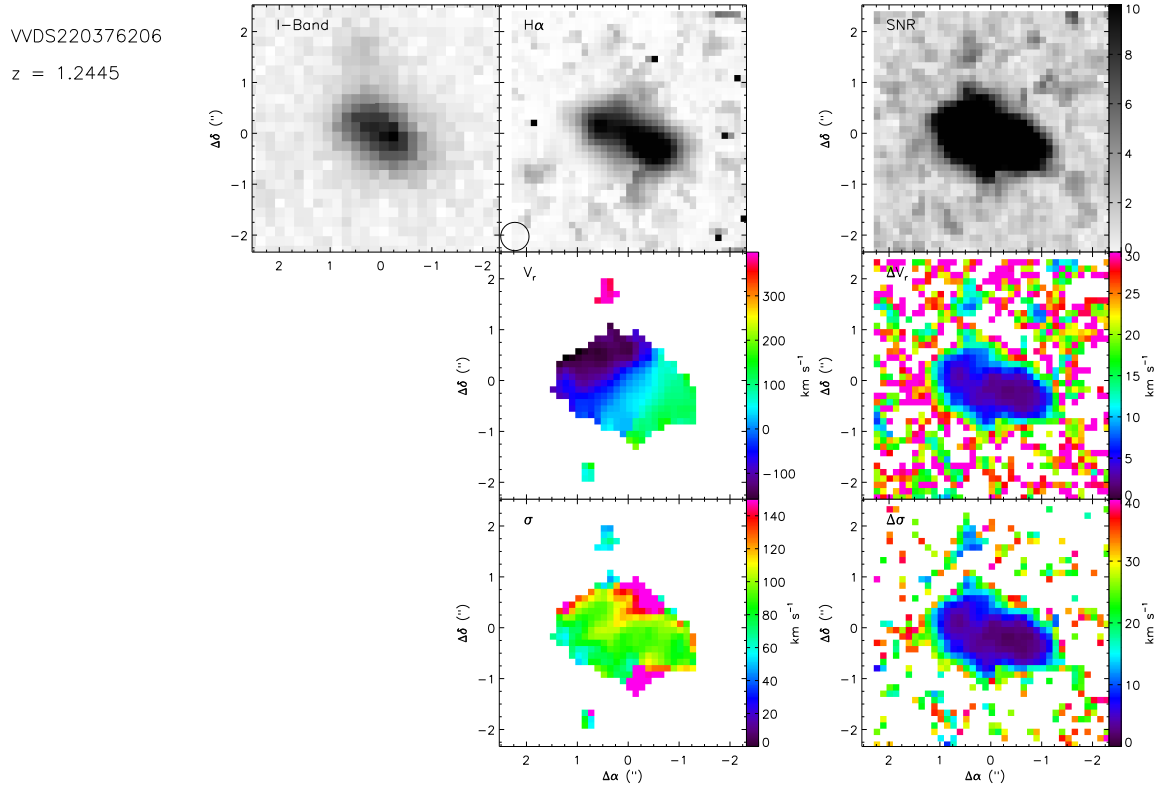
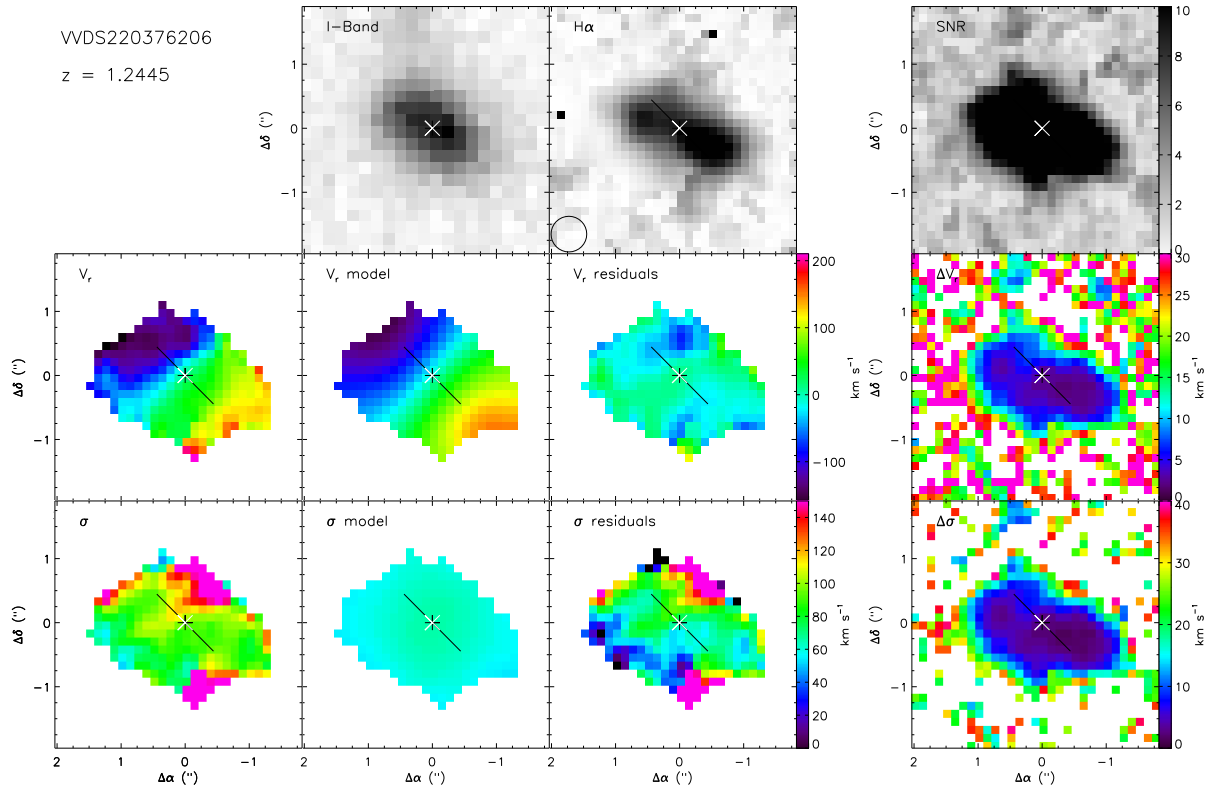


Fig. B.41. Maps for VVDS220148046. Same caption as Figure B.1.





**Fig. B.42.** Maps for VVDS220376206 system. Same caption as Figure B.2.



**Fig. B.43.** Maps for VVDS220376206. Same caption as Figure B.1.

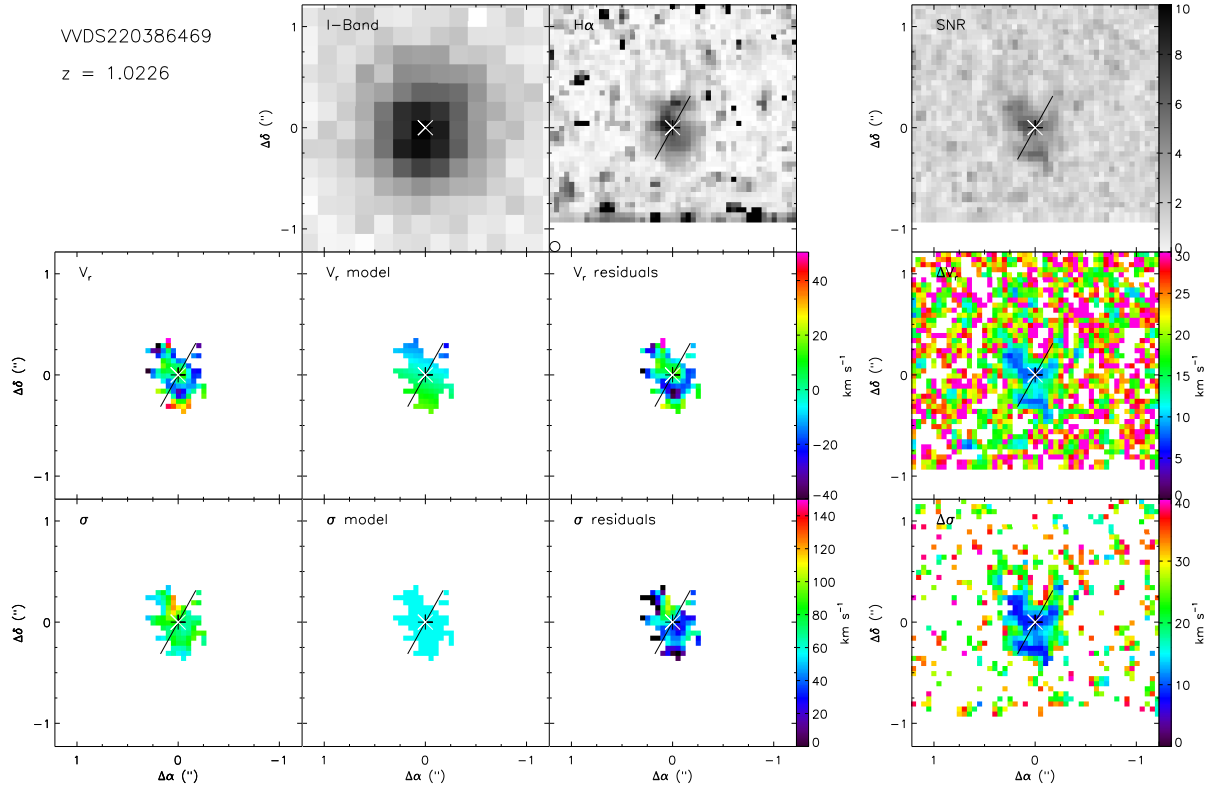


**Fig. B.44.** Maps for VVDS220386469. Same caption as Figure B.1.

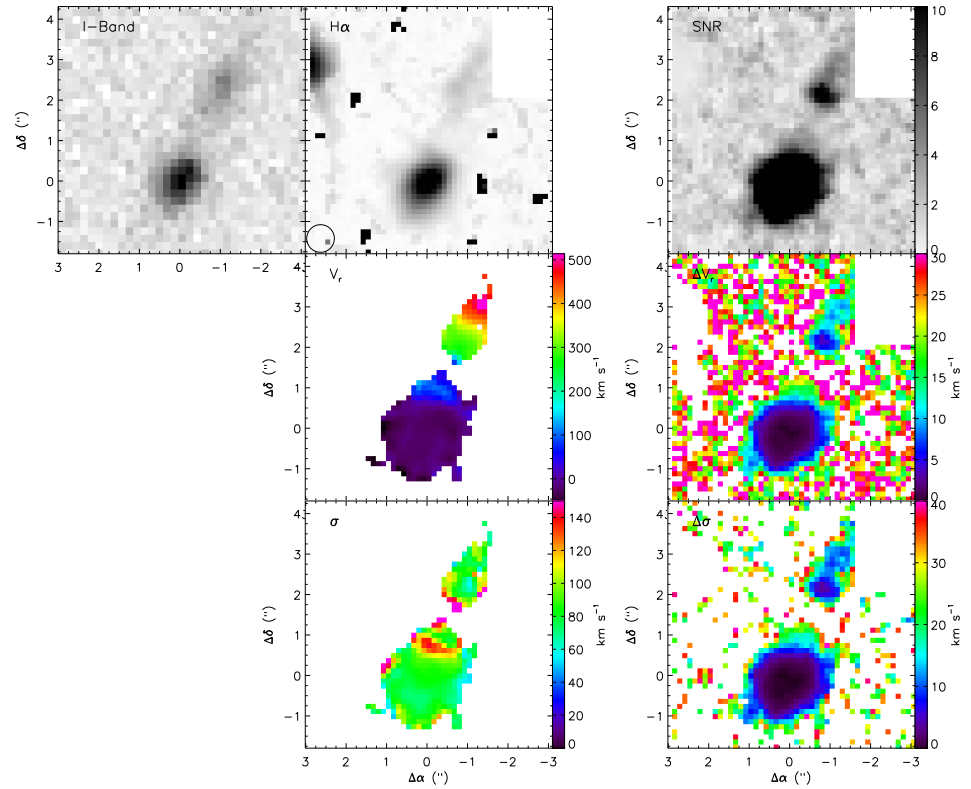


**Fig. B.45.** Maps for VVDS220397579 system. Same caption as Figure B.2.

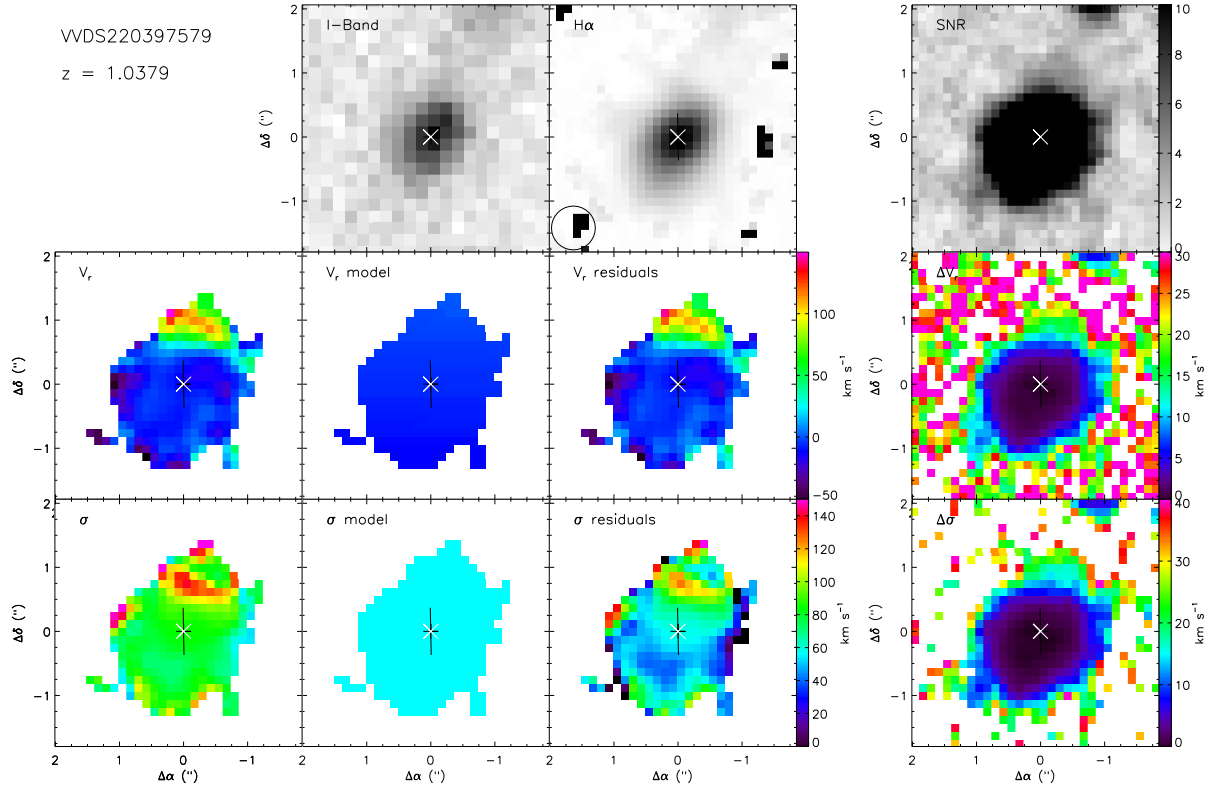


Fig. B.46. Maps for VVDS220397579. Same caption as Figure B.1.

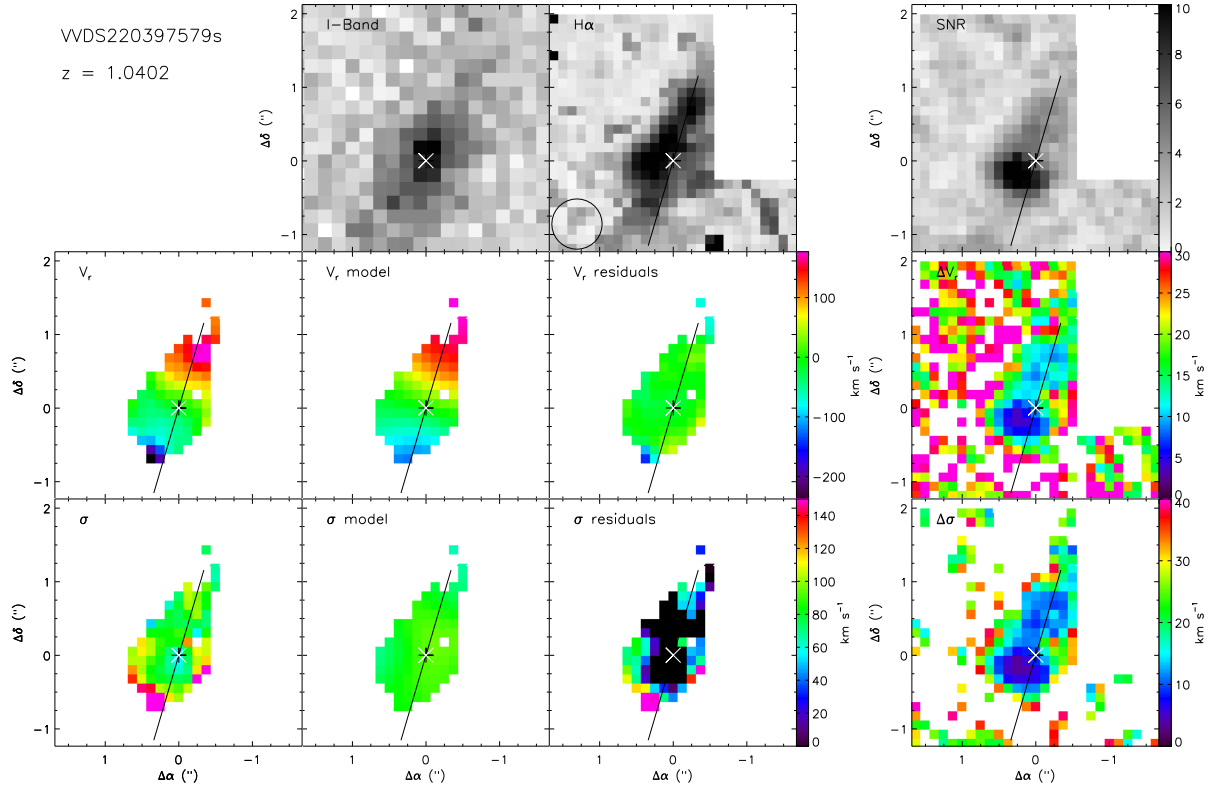
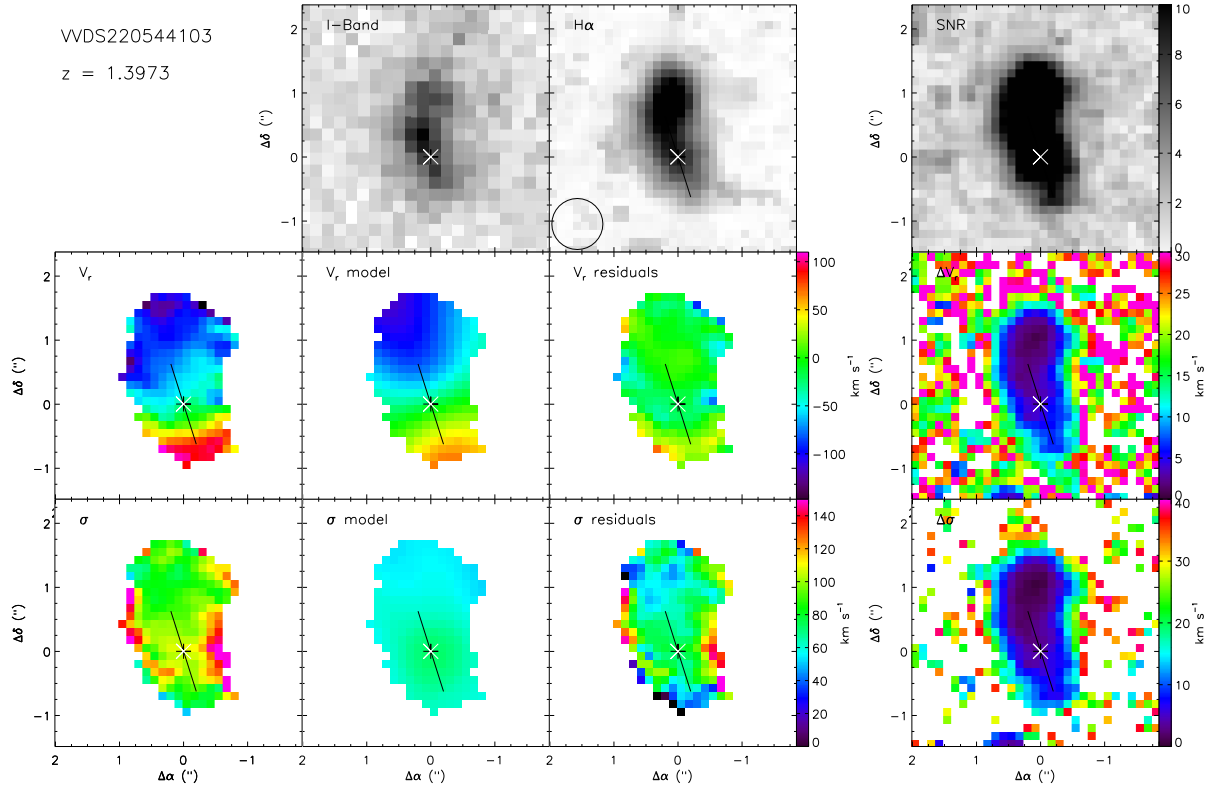
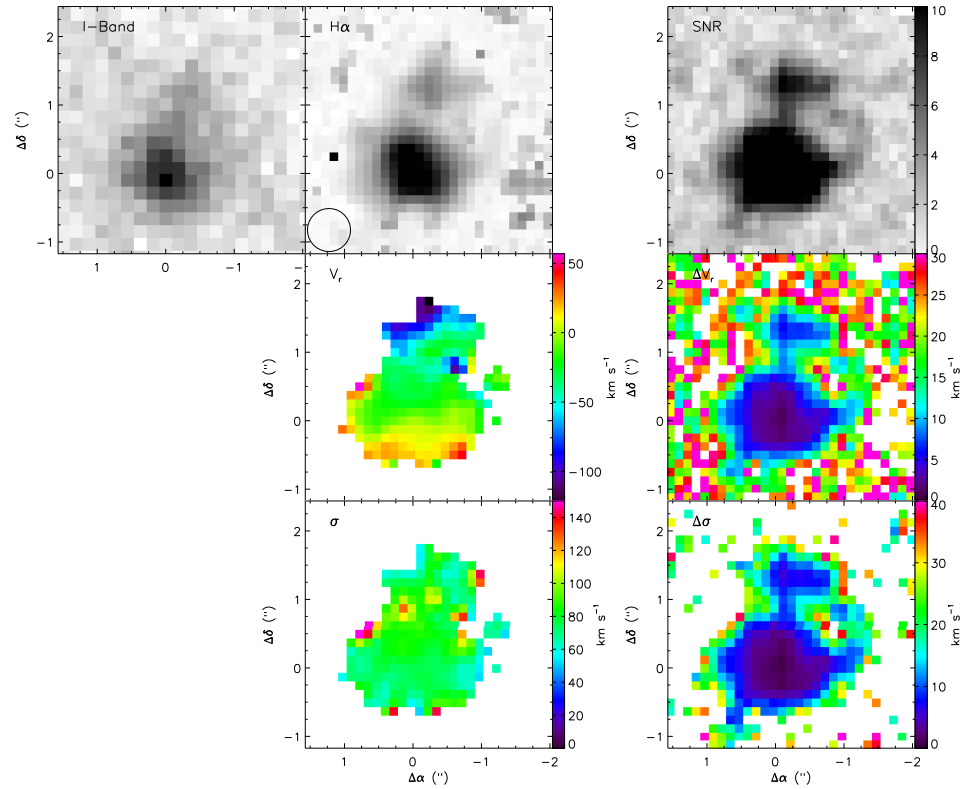


Fig. B.47. Maps for VVDS220397579 companion. Same caption as Figure B.1.



**Fig. B.48.** Maps for VVDS220544103. Same caption as Figure B.1.



**Fig. B.49.** Maps for VVDS220544394 system. Same caption as Figure B.2.

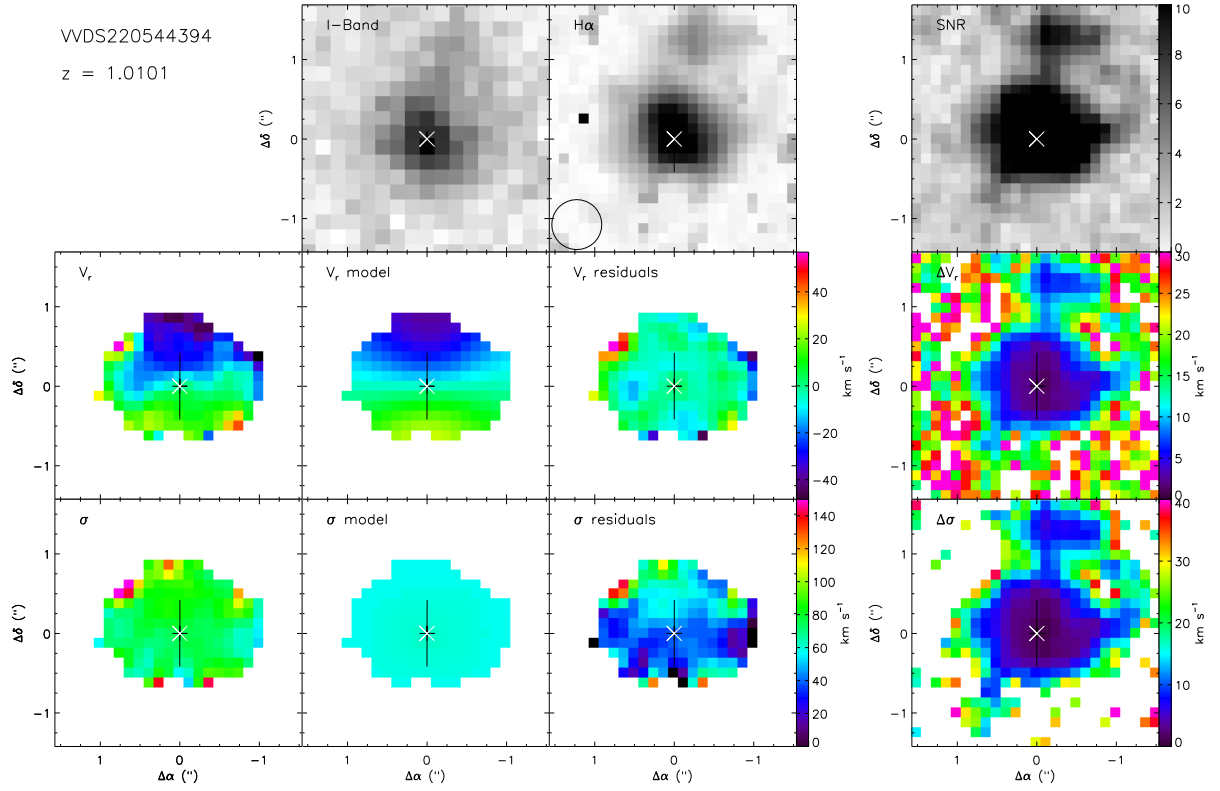


Fig. B.50. Maps for VVDS220544394. Same caption as Figure B.1.

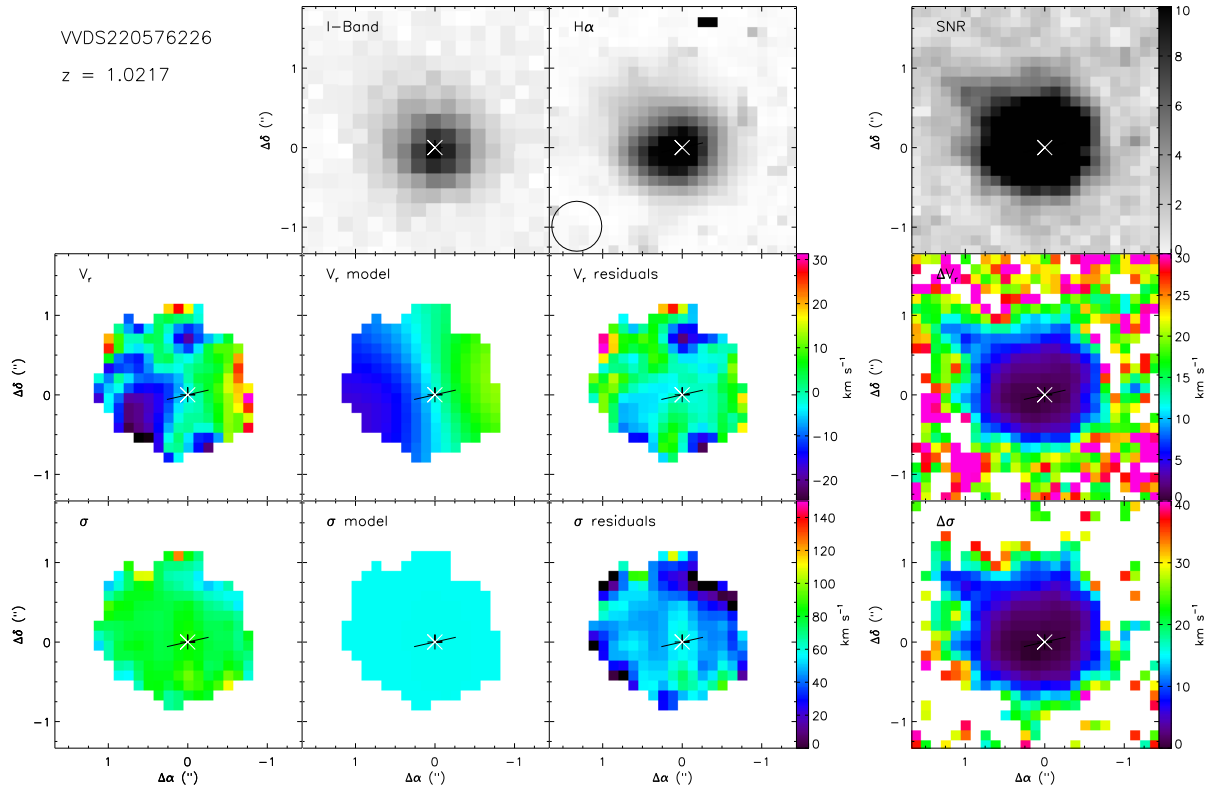
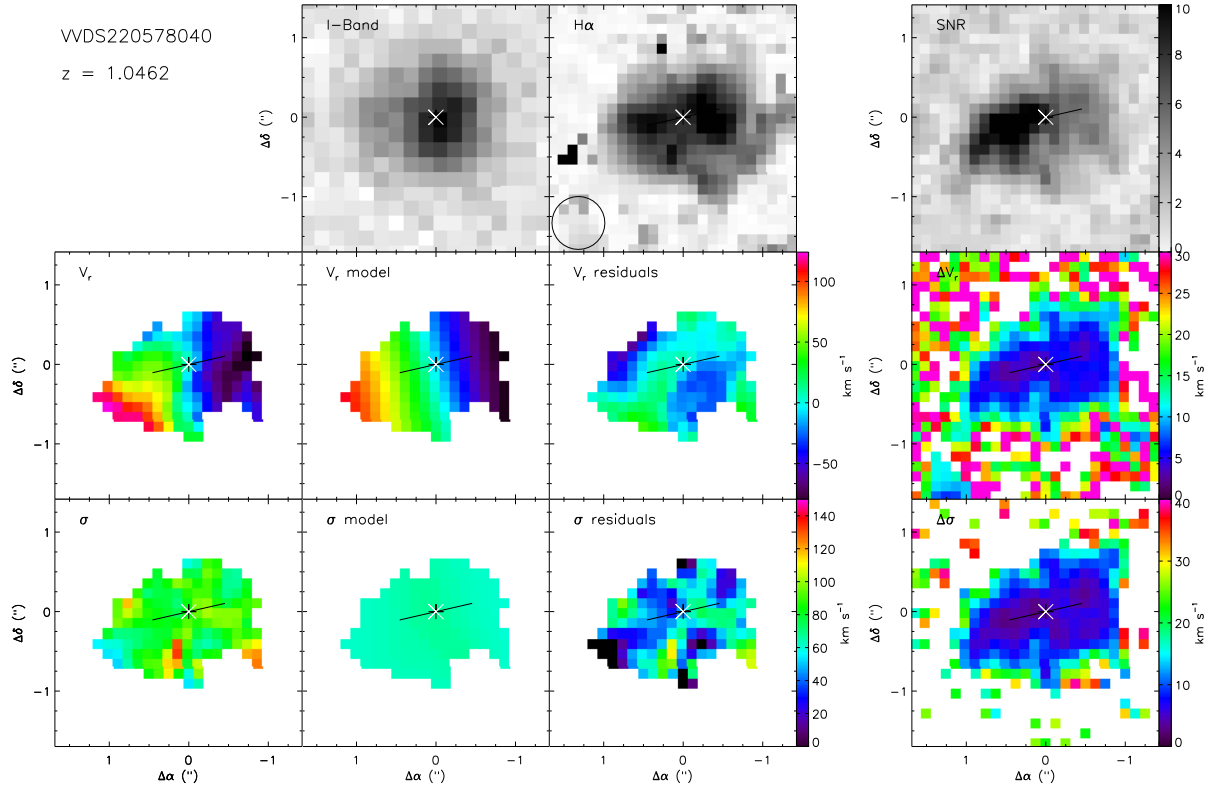
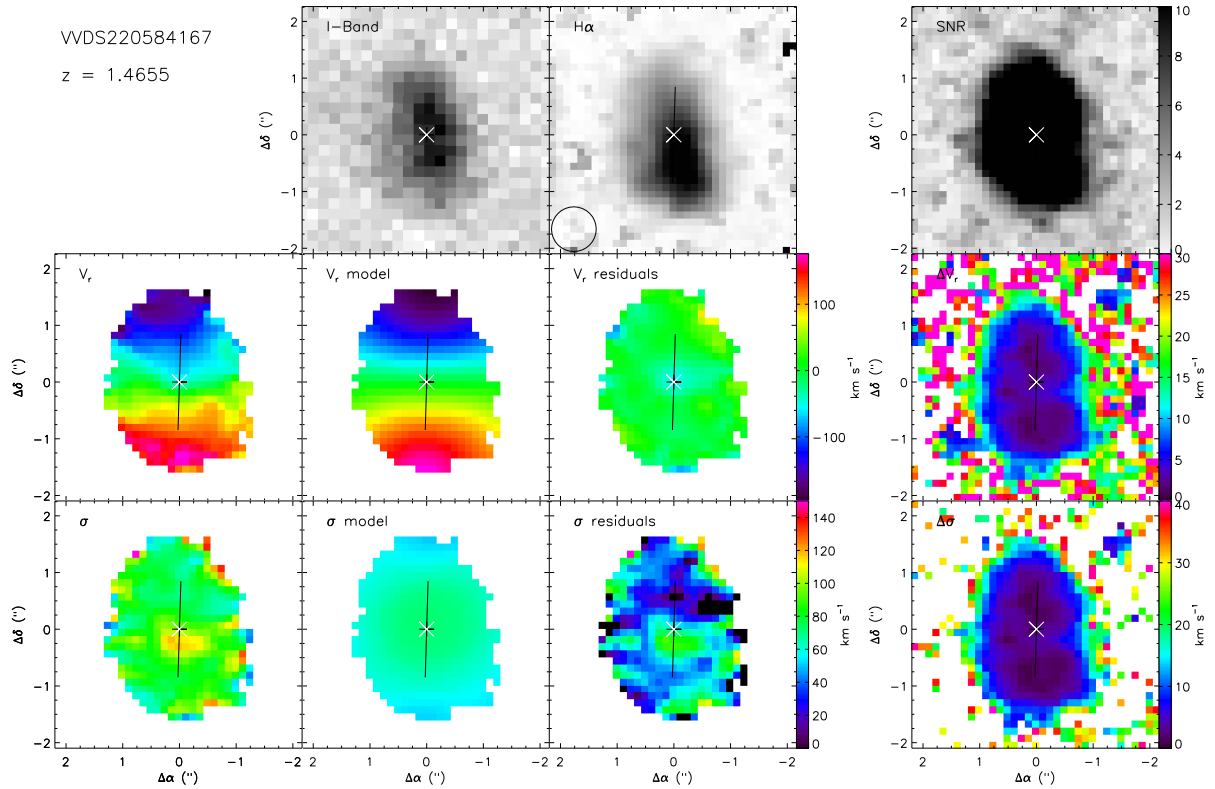


Fig. B.51. Maps for VVDS220576226. Same caption as Figure B.1.



**Fig. B.52.** Maps for VVDS220578040. Same caption as Figure B.1.



**Fig. B.53.** Maps for VVDS220584167. Same caption as Figure B.1.

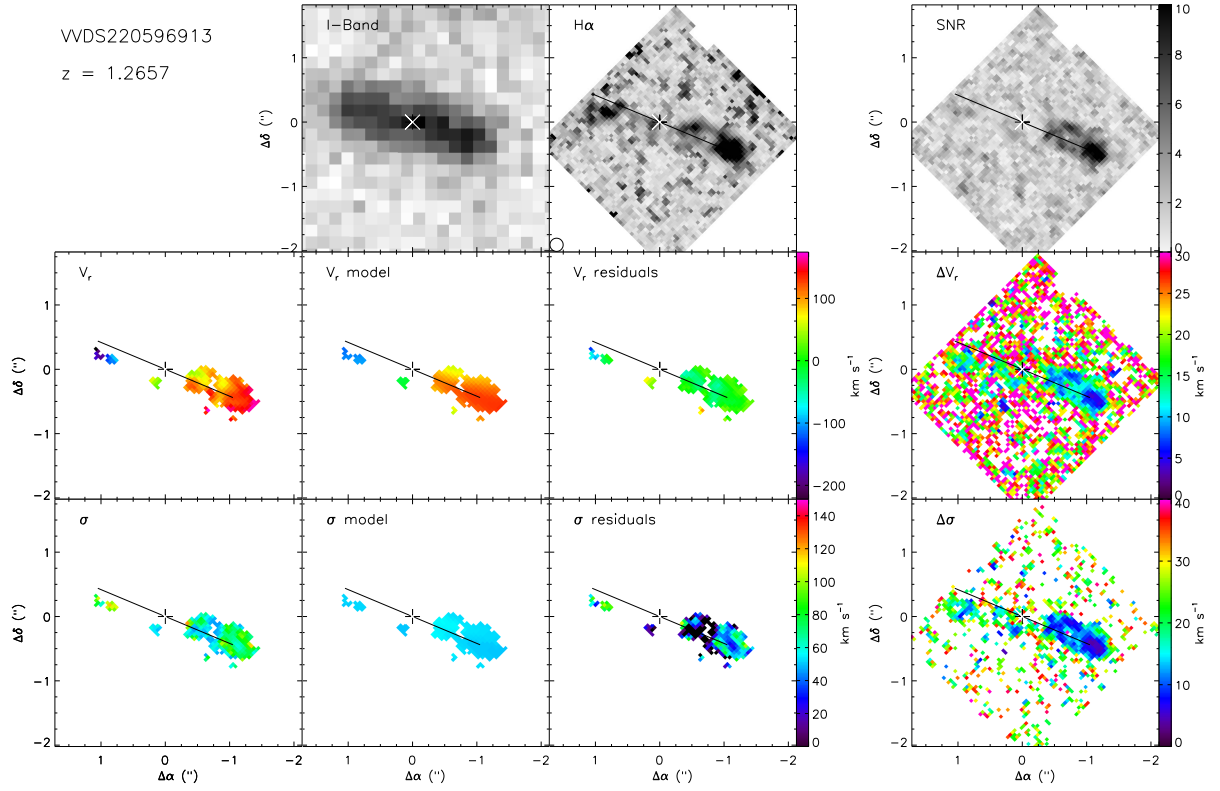


**Fig. B.54.** Maps for VVDS220596913. Same caption as Figure B.1.

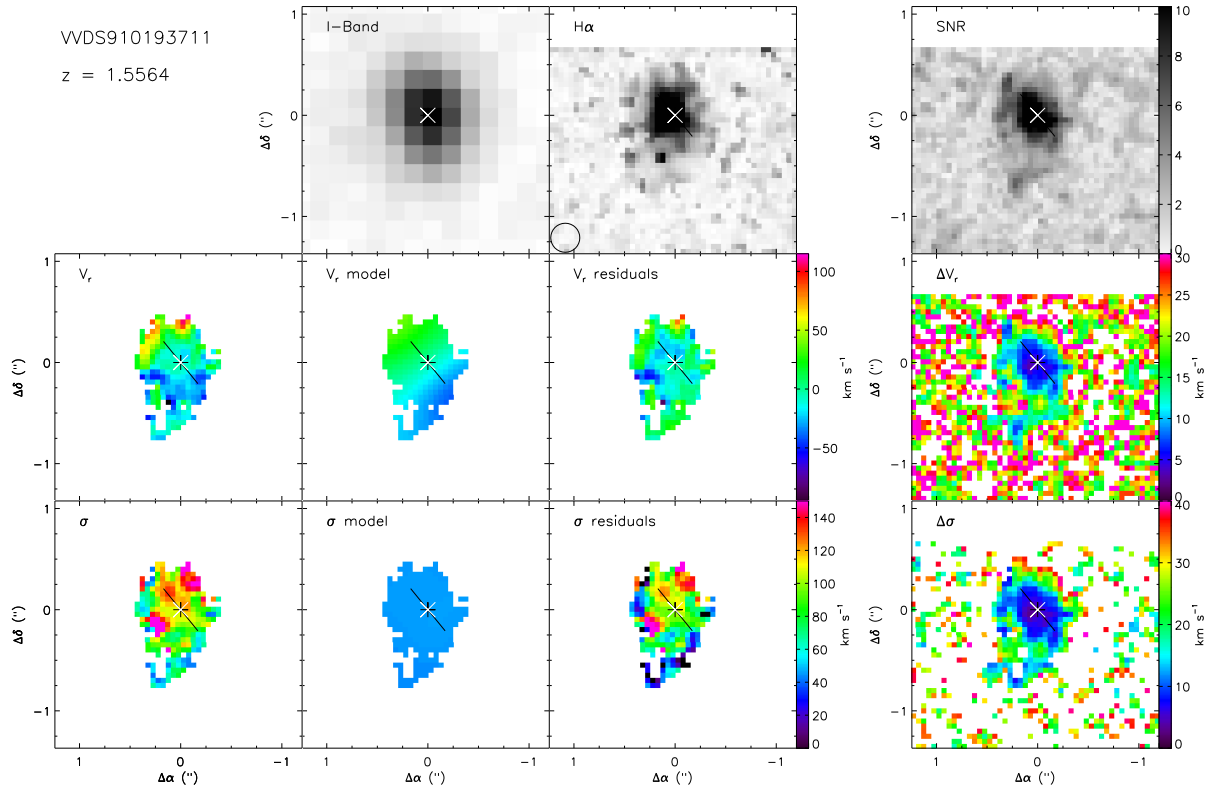


**Fig. B.55.** Maps for VVDS910193711. Same caption as Figure B.1.

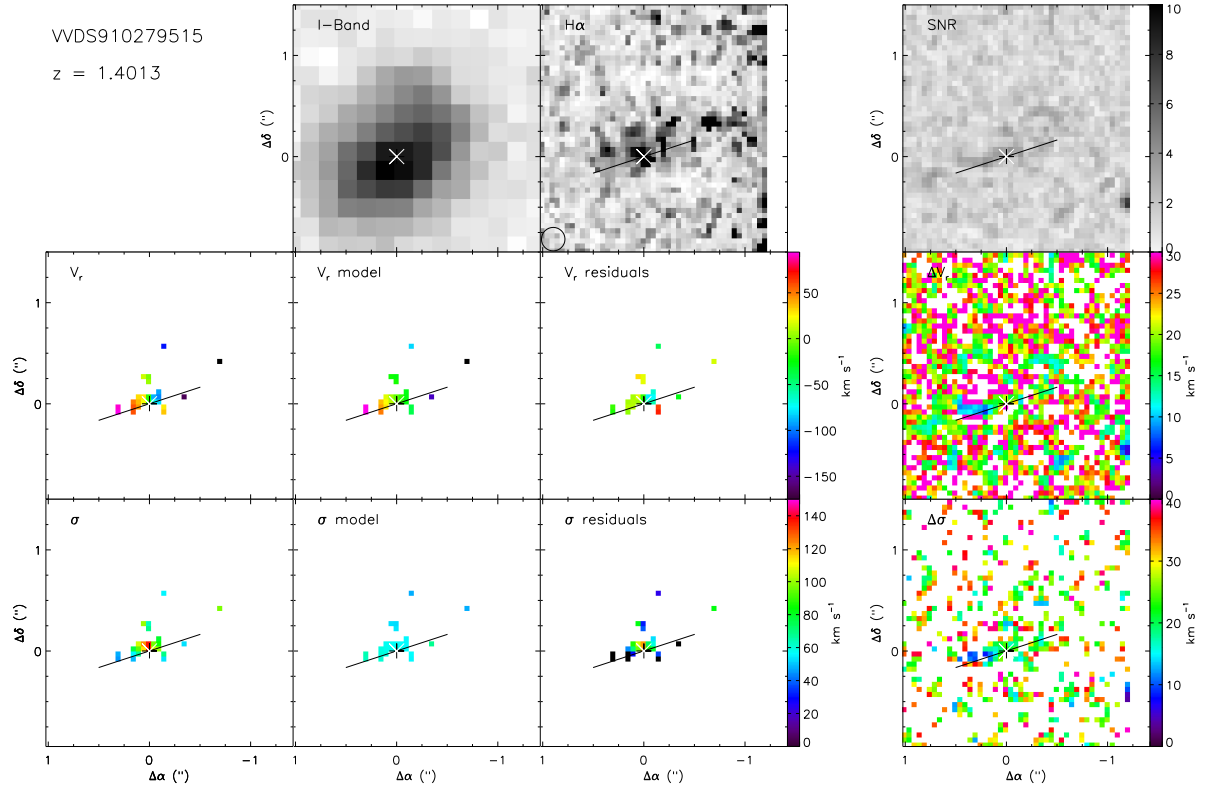


**Fig. B.56.** Maps for VVDS910279515. Same caption as Figure B.1.